Retinal disease progression

Imaging biomarkers of the functional and structural integrity of the retina

Michel Teussink

Cover: Imaging of the retina by different imaging modalities: color fundus image, fluorescein angiograph, OCT-angiography of retinal vessels, stimulus-evoked IOS from photoreceptor IS/OS-junctions, IOS from photoreceptor OS tips, and fundus autofluorescence.

Lay-out: Ruben Stoel (binnenwerk), Stefanie van den Herik and Remco Wetzels (cover), Proefschriftmaken.nl, Utrecht.

Printed by Proefschriftmaken.nl

Retinal disease progression

Imaging biomarkers of the functional and structural integrity of the retina

Proefschrift

ter verkrijging van de graad van doctor
aan de Radboud Universiteit NIjmegen
op gezag van de rector magnificus prof. dr. J.H.J.M. van Krieken,
volgens besluit van het college van decanen
in het openbaar te verdedigen op
woensdag 31 mei 2017 om 10.30 uur precies

door

Michel Marco Teussink

geboren op 21 november 1984
te Enschede

Promotoren: **Prof. dr. C.B. Hoyng**
                                          Prof. dr. B.J. Klevering

Copromotor: **Dr. T. Theelen**

Manuscriptcommissie: **Prof. dr. B. van Ginneken**
                                          Prof. dr. J.F. de Boer
                                          Vrije Universiteit Amsterdam
                                          Dr. P.E.J. van Erp

Table of contents

List of abbreviations

A2E	*N*-retinylidene-*N*-retinylethanolamine
ABCR/ ABCA4	ATP-binding cassette transporter, sub-family A, member 4
AF	autofluorescence
ANSI	American National Standards Institute
AO	adaptive optics
atRAL	all-*trans*-retinal
atROL	all-*trans*-retinol
BCR	birdshot chorioretinopathy
BCVA	best-corrected visual acuity
CC	choriocapillaris
cGMP	cyclic guanosine monophosphate
CME	cystoid macular edema
CNG channel	cyclic nucleotide gated channel
CNV	choroidal neovascularization
CSC	central serous chorioretinopathy
cSLO	confocal scanning-laser ophthalmoscopy
ERG	electroretinography
FA	fluorescein angiography
FOV	field of view
GA	geographic atrophy
GCL	ganglion cell layer
ICGA	indocyanine-green angiography
ICNIRP	International commission of non-ionizing radiation protection
INL	inner nuclear layer
IOS	intrinsic optical signals
IPL	inner plexiform layer
IS/OS	photoreceptor inner/ outer segment
JI	Jaccard index
MC simulation	Monte-Carlo simulation
OCT	optical coherence tomography
OD/ OS	oculus dexter (right eye)/ oculus sinister (left eye)
ODx	optical density
ONL	outer nuclear layer
OPL	outer plexiform layer
OSCE	optical Stiles-Crawford effect
PDE	phosphodiesterase

PDT	photodynamic therapy
qAF	quantitative fundus autofluorescence
ROI	region of interest
RP	retinitis pigmentosa
RPE	retinal pigment epithelium
SD-OCT	spectral-domain OCT
SNR	signal-to-noise ratio
SRF	subretinal fluid
SSADA	split-spectrum amplitude decorrelation angiography
STGD1	recessive Stargardt disease (associated with *ABCA4*-mutations)

Chapter 1.

General introduction

Most diseases of the retina are accompanied with typical tissue alterations, which can be identified when viewed under sufficient magnification. The earlier in the disease process, the more subtle are these abnormalities. The progression of these diseases is, in many cases, also fairly gradual with subtle changes at the leading disease front which become more profound with advancement of the disease. Accurate measurements of these changes, based on imaging techniques sensitive enough to detect them, can be of great clinical interest to make a more accurate prognosis, to better understand the disease process, and to evaluate any effects of treatment. In this thesis, an effort is made to identify disease-associated changes in retinal images (imaging biomarkers), and to better understand their relationship with the disease process. In the following, we describe the structure and biology of the retina and choroid and aspects that are relevant from a biophysical perspective. This provides insight into what is being visualized with the imaging techniques used in this thesis.

1.1 Optical and functional aspects of retinal anatomy

The eye is a highly specialized structure dedicated to the detection of a fraction of the cosmic electromagnetic spectrum, the visible light. However, because our atmosphere reflects, absorbs and scatters much of the incident sunlight, this fraction constitutes most of the radiation that strikes earth's surface. The anterior part of the eye has three main functions: 1) preventing excessive light from entering the eye due to constriction of the pupil, which acts like an aperture, 2) focusing of light to form a sharp image, primarily by the cornea and also by accommodation of the lens, and 3) filtering of hazardous optical radiation.

The eye is equipped with several natural filters, including the cornea, lens and vitreous. These only allow photons in the wavelength range of 0.380 – 1.4 μm to penetrate and reach the ocular fundus (Figure 1).[1] The ocular media transmission increases from about 50% for blue light (λ = 450 nm) to 60% for blue-green light (λ = 500 nm), up to about 74% for red light (λ = 600-1400 nm).[2] Part of the infrared radiation is absorbed by the cornea and the lens – mainly the water bands at 980, 1200, and 1430 nm. The vitreous absorbs light above 1400 nm, up to 10 μm.[1]

The posterior part of the human eye consists of three main structures (Figure 1). The first is the retina: a thin and nearly transparent sheet of nervous tissue that serves as the sensory part of the visual system. The second structure is the choroid, which is important for blood supply and nutrition of the eye. The third, the sclera, maintains the shape of the eye and protects the inner ocular structures. In the outer—most posterior—part of retina, photons may be absorbed by light-sensitive molecules in the membranes of stacked disks in the outer segments of photoreceptor cells. This triggers a process called phototransduction, which involves a set of signaling molecules that lead to the generation of an electrical pulse ('action potential'), and transduction of the pulse along retinal neurons (situated in the inner retina), towards the optic nerve.[3]
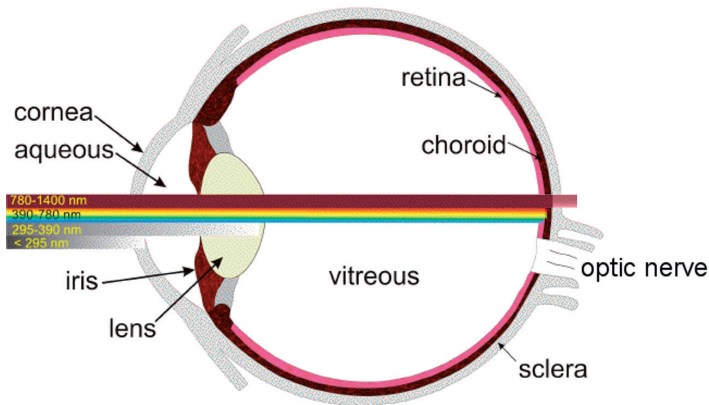
Figure 1. Anatomy of the human eye and transmission of optical radiation. Numbers indicate the wavelength range of transmitted light. Note the partial sclera penetration by infrared light.

(Figure adapted from http://www.photobiology.info/Rozanowska.html)

The retina houses three major types of light-sensitive cells; photoreceptive ganglion cells, rod-, and cone photoreceptors. Photoreceptive ganglion cells are specialized neurons that contain the light-sensitive protein melanopsin (wavelength of maximal absorption λ_{max} ~480 nm),[4] which connect to neurons of the suprachiasmatic nucleus for setting and maintaining circadian rhythms, or to neurons of the Edinger-Westphal nucleus for control of the pupilary light reflex. Rod photoreceptors ('rods'), by far the most numerous of these three types, are found throughout the retina with the notable exception of the foveola. Rods are responsible for peripheral vision during daytime, and are the exclusive cell-type providing vision during low light conditions (scotopic vision). Cone photoreceptors ('cones') are the main type of light-sensitive cell in the central region of the retina, the macula lutea. Under sufficient illumination (2.9 photopic cd·m^{-2}), rods responses are in saturation and photopic vision is initiated by the outputs of three different cones classes (L-, M-, and S-cones) with partially overlapping spectral sensitivities to provide trichromatic color perception. The most-centered region of the macula is called the fovea (1 mm^2), within which the foveola (0.1 mm^2) that only contains cones (Figure 2). This cell-type is responsible for vision at high spatiotemporal resolution and for the discrimination of colors.

The retinal pigment epithelium (RPE) is the outer-most part of the retina (Figure 2). The RPE is a strongly pigmented monolayer which—together with endothelial cells of non-fenestrated retinal blood vessels—acts like a blood-retina barrier. This barrier allows exchange of nutrients, growth factors and waste products between the subretinal space and the choriocapillaris. The pigmentation of the RPE provides absorption of light that has passed through the photoreceptors, which protects against reflected light from the sclera that would otherwise degrade the visual image. Many RPE cell functions are critical to the health and maintenance

13

of photoreceptors. These include but are not limited to the regulation of photoreceptor excitability and metabolism, and the active removal of water from the subretinal space in order to hold the neural retina in proximity to the RPE (reviewed by Sparrow *et al.*, 2010).[5] The RPE also regulates the secretion of immunosuppressive factors and it thereby coordinates the immune response potential.
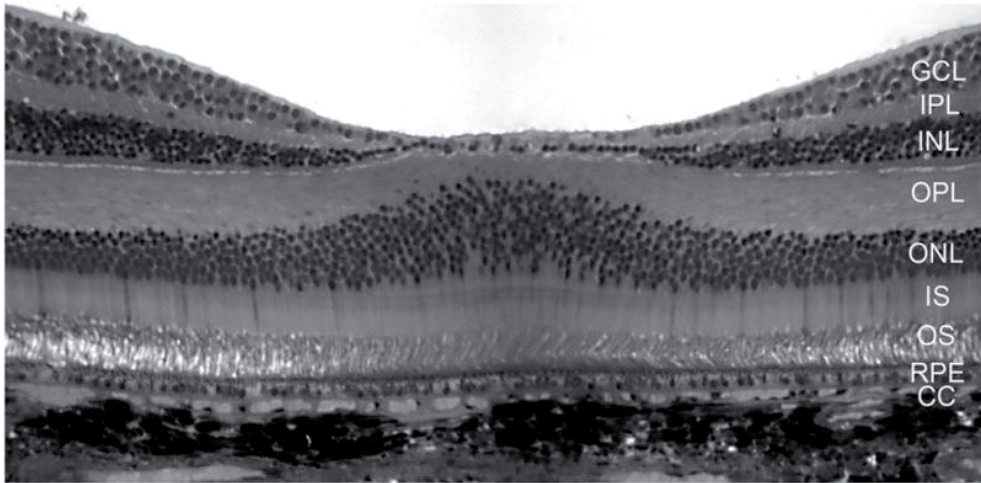
Figure 2. Histological cross-section of the fovea from a macaque monkey, demonstrating the layers of the retina. GCL: ganglion cell layer, IPL: inner plexiform layer, INL: inner nuclear layer, OPL: outer plexiform layer, ONL: outer nuclear layer, IS/ OS: photoreceptor inner/ outer segments, RPE: retinal pigment epithelium, CC = choriorocapillaris. The foveola can be discerned by the near-absence of the INL, IPL, and GCL layers. The Bruch's membrane that separates the RPE and CC is not discernible at this magnification.

The retina is maintained by blood from two main sources: the central retinal artery and the choroidal blood vessels. The choroid receives most of the blood flow (65-85%),[7] and is vital for maintaining the outer retina and the photoreceptors in particular. The remaining 15-35% flows via the central retinal artery from the optic nerve head to supply the inner retina. The intraretinal arteries 'feed' three capillary networks: the radial peripapillary capillaries, the inner-, and outer layers of capillaries. The choroidal arteries branch from posterior ciliary arteries and from vessels of Zinn's circle, around the optic disk. Each of the posterior ciliary arteries fan out into lobules of capillaries that supply local regions of the choroid.[8] These ciliary arteries feed into three vascular layers in the choroid: the outer (Haller's layer, most scleral), medial (Sattler's layer), and the inner layer of blood vessels, called the choriocapillaris (Figure 3). There is an extremely metabolic tissue on one side of the choriocapillaris (RPE and retina) and an essentially inactive connective tissue on the other, scleral, side. Consistent with this polarization is the relatively high concentration of capillary fenestrations on the retinal

side.[9] Exchange of fluid and nutrients takes place through these fenestrations, although the involved molecules are limited in size to less than 330.000 Dalton,[10] and 440.000 Dalton with molecule diameter 110 Ångström (11 nm).[11] In contrast to the foveal avascular zone of the retinal circulation, the choriocapillaris exhibits a greater blood flow, capillary density,[12-14] and frequency of fenestrations [9] in the submacular region. Blood is drained into pre-capillary venules and then veins, which run towards the equator into vortex veins, which merge into the ophthalmic vein.
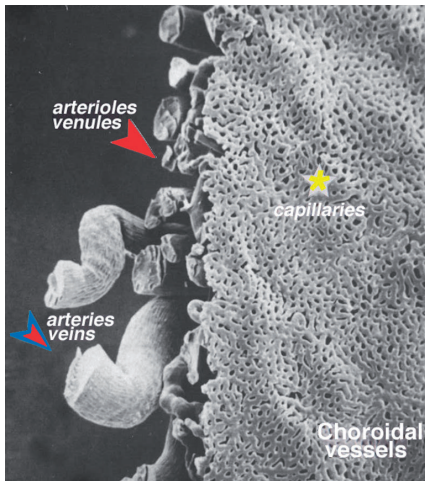
Figure 3. Corrosion cast of the human choroid, showing its three vascular layers: outer arteries and veins (red/blue arrowhead), medial arterioles and venules (red arrowhead), and choriocapillaris (star).
Reprinted from *Prog Retin Eye Res,* vol. 13, Zhang HR, Scanning electron-microscopic study of corrosion casts on retinal and choroidal angioarchitecture in man and animals, pp. 243-270,[15] Copyright (1994), with permission from Elsevier.

1.2 Physiology of vision

Vision is mediated by phototransduction and processing of the visual input by the suprachiasmatic nucleus. The visual (retinoid) cycle is the process that provides the 11-*cis*-retinal that is utilized for photon capture during phototransduction, and that removes potentially toxic byproducts of phototransduction. Both phototransduction and the visual cycle are essential for vision, and defects in these systems are often the cause of inherited blindness. Such defects often manifest as phenotypes with a specific constellation of pathological features on high-resolution retinal imaging.

1.2.1 The phototransduction cascade

Rhodopsin is a G-protein coupled receptor that consists of an opsin molecule and the chromophore 11-*cis*-retinal, situated in the membrane of the rod outer segment disk. Upon capture of a photon, 11-*cis*-retinal converts to its isomer all-*trans*-retinal (atRAL). Rhodopsin subsequently undergoes a series of extremely quick photoisomerization reactions until its first relatively stable isomer, metarhodopsin II, is formed. Metarhodopsin II catalyzes activation of the G-protein transduction, which couples very rapidly with phosphodiesterase (PDE). This enzyme, in turn, catalyzes the hydrolysis of cyclic guanosine monophosphate

(cGMP). The cytoplasmic concentration of cGMP diminishes quickly, which causes cyclic nucleotide gated (CNG) channel-bound cGMP to dissociate. In the dark, cGMP is responsible for holding open CNG channels to allow an influx of sodium ions, which maintains the outer segment membrane in a depolarized state, such that a 'dark current' flows through the cell. This dark current causes voltage-gated calcium influx channels to remain open. The resulting high intracellular calcium concentration causes constant release of the neurotransmitter glutamate in the dark. In the light then, cGMP hydrolysis causes closure of CNG channels leading to hyperpolarization of the OS membrane, which causes closure of voltage-sensitive calcium channels along the OS, resulting in cessation of the dark current and inhibition of glutamate release.

Phototransduction is followed by a cessation and recovery phase. First of all, rhodopsin kinase phosphorylates metarhodopsin II leading to binding of arrestin, which stops the activation of transducin.[16] Second, transducin is inactivated by GTPase accelating protein, thereby silencing the PDE. The rate-limiting step of PDE inactivation, which is determined by the slowest biochemical reaction,[17] differs between rods and cones: in rods it is the inactivation of transducin,[18] while in cones it is the rate of cone opsin phosphorylation.[19] PDE inactivation allows calcium ions to flow into the cell. Intracellular cGMP levels are restored by guanylate cyclase, which is likely the key event in restoring the dark current [20] and terminating the light response. In the recovery phase, all-*trans*-retinal dissociates from rhodopsin and is recycled to 11-*cis*-retinal via the visual cycle (explained below). Arrestin dissociates when all-*trans*-retinal has dissociated from rhopdopsin, following by rhodopsin dephosphorylation. Regeneration of rhodopsin occurs upon binding of regenerated 11-*cis*-retinal.

1.2.2 The visual cycle

11-*cis*-retinal, the primary 'fuel' of the phototransduction cascade, is generated both out of dietary vitamin A after absorption in the blood (all-*trans*-retinol), and from regeneration of atRAL in the RPE. The visual cycle (Figure 4) and phototransduction take place simultaneously. At least some of the aldehyde atRAL, upon release from the transmembranous rhodopsin molecule into the outer segment disk lumen, reacts with phosphatidylethanolamine (PE) (1:1 ratio) in the disk membrane to form *N*-retinylidene-phosphatidylethanolamine (NRPE).[21-25] This sequestration may be an important mechanism to limit the toxicity of atRAL.[26] It is well known that NRPE is the ligand of the retina-specific lipid transporter protein ABCA4 (ATP-Binding Cassette, sub-family A, member 4), which is thought to serve in the delivery of atRAL to cytosolic retinol dehydrogenases (RDH); a group of enzymes that reduce vitamin A aldehyde to the non-reactive alcohol form (*i.e.*, atRAL is reduced to all-*trans*-retinol, atROL).[24, 27-33] atROL is subsequently transported into the interphotoreceptor matrix retinal binding protein (IRBP) that transports it into the RPE cytoplasm.[34] Here, atROL binds to cellular retinol binding protein (CBRP), after which atROL is re-isomerized by a cascade involving lecithin:retinol acetyltransferase (LRAT), RPE specific protein 65 kDa (RPE65) and

finally 11-*cis*-retinol dehydrogenase (RDH5).[35-39] The 11-*cis*-retinal is transported into the interphotoreceptor matrix by cellular retinaldehyde binding protein (CRALBP) and into the outer segment cytoplasm by IRBP. 11-*cis*-retinal then binds opsin: rhodopsin regeneration. This visual cycle is the only means by which rods can regenerate rhodopsin.[40, 41] Cones, however, have a secondary visual cycle taking place in cone outer segments and Müller cells which allows for 11-*cis*-retinal regeneration at a 20-fold faster rate, which is necessary to allow for sustained daylight vision.[42]
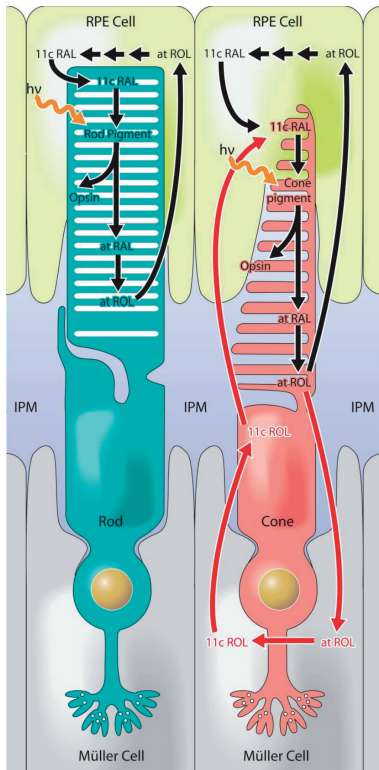
Figure 4. Schematics of two visual cycles in vertebrate rods and cones. The RPE visual cycle (*left*) recycles all-trans-retinol (at ROL) released from rods and cones following a bleach of 11-*cis*-retinal (11c ROL), which can be used by both rods and cones for visual pigment regeneration. The retina visual cycle (*right*) relies on the Müller cells to recycle all-*trans*-retinol released from cones to 11-cis-retinol, which only cones can move to their outer segments and oxidize to 11-*cis*-retinal for regeneration of the pigment. *IPM*: interphotoreceptor matrix, *hv*: photon of light.

This work was originally published in the Journal of Biological Chemistry. V. Kefalov. *J Biol Chem* 2012; 287:1635-1641.[43] © the American Society for Biochemistry and Molecular Biology.

1.3 A brief history of retinal imaging

The retina is a unique structure from an optical perspective, because of its high optical accessibility and the tiny space it occupies despite its physiological importance. The invention of the Augenspiegel ('eye mirror') by Herrmann von Helmholtz (1851) led via rapid subsequent developments to the invention of the first electric field light ophthalmoscope by William Dennet in 1885, after which ophthalmoscopy became a widely used examination technique in ophthalmology. The combination with photography, which gradually developed into a practical technique during the 1820's to 50's, proved possible as early as 1853, although it took until 1907 to obtain useful fundus photographs.[44]

As one of the main causes of visual loss in several major eye diseases, the leakage of blood from the retinal vasculature is an important clinical sign of pathology. The invention of fluorescein angiography, which visualizes blood leakage by fluorescent imaging of pre-injected contrast dye (fluorescein), greatly improved the capability to observe this sign. However, light reflected by the anterior segment of the eye and fluorescence of the lens proved to be important obstacles to obtaining sharp and useful images. Marvin Minsky was the first to patent the principle of confocal microscopy (1957), which is a technique to limit the depth-of-focus of the observation light, which cannot be done with conventional microscopy. In other words, a confocal microscope only 'sees' one depth at a time ("optical sectioning"), in contrast to a conventional microscopy which 'sees' as far as the light can penetrate. The laser scanning process was designed by Thomas and Christoph Cremer (1978), which scans the three-dimensional surface of an object point-by-point by means of a focused laser beam, after which an over-all picture is created. These two combined techniques led to the development of confocal laser-scanning microscopy and, in ophthalmology, to confocal scanning-laser ophthalmoscopy (cSLO) by Webb and coworkers in 1981,[45] which allowed for the exclusive detection of contrast dye fluorescence emanating from the fundus.

Subsequent technological innovations led to the development of highly sensitive, low-noise, high-speed camera's for a variety of optical wavelengths. With this, it became possible to observe the very weak light emitted by the retina's endogenous fluorophores (autofluorescence).[46] Advances in different disciplines in optical imaging led to the development of optical coherence tomography (OCT),[47] which dramatically improved upon the optical sectioning capability afforded by cSLO (optical depth resolution of ~7 μm with OCT versus ~200 μm with cSLO).

1.4 Fundus autofluorescence

Fluorescence is the emission of photons by a substance that was excited by absorbance of electromagnetic radiation or by a different process (*e.g.,* the product of a reaction). It occurs when an orbital electron of a molecule or atom relaxes to its ground state by emission of a photon from an excited singlet state. In most cases, the emitted light has a longer wavelength, and thus lower energy, than the absorbed radiation. The retinal fundus exhibits an intrinsic fluorescence: autofluorescence (AF). AF recorded with a cSLO has a typical intensity distribution in the healthy fundus (Figure 5). AF appears to be absent in blood vessels due to absorption by hemoglobin, while the retinal center appears darker due to absorption by macular pigments. AF is commonly regarded as a means to monitor the health of RPE-cells, with areas of high AF indicating increased lipofuscin levels, areas of lower AF as RPE-damage, and areas or near-absent AF indicating RPE loss. The correct interpretation of AF is more complex than this because there are more factors that can cause signal variability,[48, 49] *e.g.* stacked RPE-cells can cause hyper-AF,[50] hyper-AF in flecks in STGD1 appears to be derived

from bisretinoids in photoreceptor outer segments,[51] photooxidized bisretinoids have increased fluorescence intensity,[52] etc. It is anticipated that a more thorough understanding of fundus AF patterns may impact its use as a therapeutic outcome measure.[48] Fundus AF therefore can serve as an imaging biomarker, *i.e.* an optical signal indicative of specific biological processes that varies with a given disease state.

AF originates from fluorescent metabolites of vitamin A (called bisretinoids) in lipofuscin, located in the RPE.[53] In the photoreceptor outer segments, NRPE can undergo hydrolysis to release atRAL; however, when it reacts non-enzymatically with a second molecule of atRAL, the irreversible formation of toxic vitamin A dimers (also known as bisretinoids) occurs.[26] One of the most important functions of RPE-cells is the phagocytosis of outer segment disks when they are shed, at a diurnal rhythm, by photoreceptors.[54] Due to this function, the bisretinoids generated in the outer segments are transferred to the RPE and accumulate in lysosomal bodies in which RPE lipofuscin is stored.
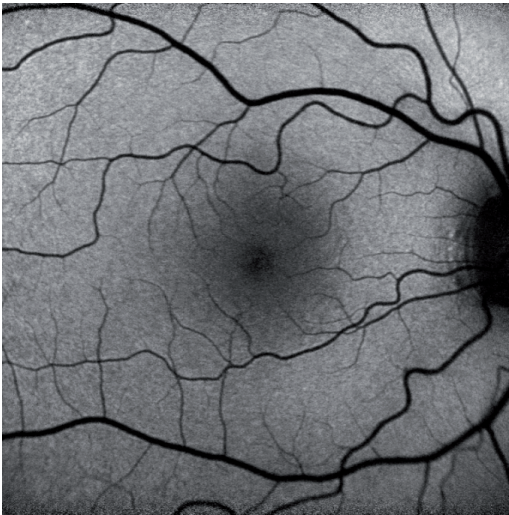
Figure 5. Fundus autofluorescence image of a healthy 25-year old female, recorded with a cSLO. Blood vessels and the optic disk (center right) appear dark due to absorption by hemoglobin, while higher intensities indicate lipofuscin fluorophores accumulated in the RPE. The fovea (center) appears dark due to absorption by macular pigments.

1.4.1 Fundus autofluorescence as an imaging biomarker

Recently there has been a growing clinical appreciation of the sensitivity of AF imaging to detect outer retinal pathology that can be difficult to discern by conventional ophthalmoscopy. It is particularly helpful to visualize atrophy of the retinal pigment epithelium (geographic atrophy, GA).[55-58] The typical patterns of altered fundus AF in inherited retinal diseases can be exceedingly helpful in diagnosing disorders like pattern dystrophies such as Stargardt disease. However, AF can indicate more than the presence of a retinal disease; it can also serve as a biomarker of disease progression. In age-related macular degeneration (AMD), the enlargement of areas of near-absent AF (GA) was correlated with patterns of irregular AF in the surrounding border zone,[59] which was identified as an important risk factor for disease

progression.[59, 60] In Stargardt disease, the gene encoding for ABCA4 is mutated,[61] in most patients giving rise to fish-tail flecks with high fundus AF that are highly typical of the disease. In most cases, these flecks spread out in a centrifugal pattern, leaving behind a trail of decreased AF, thus contributing to decreased AF across the fundus.[62] In retinitis pigmentosa (RP), a hyper-AF ring surrounding the macula is considered a hallmark pathological feature and is present in 50-94% of RP patients.[63-65] This ring, which displays a highly symmetrical progression,[66] is a structural indicator for RP progression and has been reported to correlate well with changes of the outer retinal integrity.[67-71]

1.5 Optical coherence tomography

OCT is an imaging technique based on interferometry to capture images of the retina at a three-dimensional resolution approaching that of histology. Since the inception of the second generation of OCTs—Spectral-domain OCT—in 2005, it became possible to reconstruct a 3D structure with axial resolution in micrometer-scale from in-vivo measurements.[72, 73] Soon after, it saw widespread clinical application in ophthalmology because it allows the easy identification of important pathological features such as subretinal fluid, distortions and thinning of retinal layers, and retinal lesions or complications such as CNV. At present, OCT is the most commonly used clinical technique to acquire images of the retina. A generic OCT system schematic is shown in Fig 6. In a simple Michelson interferometer implementation, a beam of broadband, *i.e.* low-coherence, near-infrared light is directed into a 2x2 fiber optic coupler to achromatically (wavelength-independently) split the incident light, usually in a 80:20 or 90:10 ratio (reference:sample). Light coming from the reference fiber is directed to a mirror and redirected back into the same fiber. Light coming from the sample fiber is directed at a scanning mechanism designed to focus the beam on the sample and to scan the focused spot in one or two dimensions. The light reflected back from the retina is directed through the scanning system into the same sample fiber where it is mixed with reference light returning from the mirror, where it is made to interfere on the surface on the detector.[74] In spectral-domain OCT (SD-OCT), a diffractive grating spectrally separates the returning light into narrow bandwidths, which are focused on 1024 or 2048 separate photoreceptive elements of a high-speed line-scan camera. The received signals, representing electric field $r_s(k)$ versus wavenumber *(k)*, are processed by inverse Fourier transformation into power magnitude reflectivity $R_s(z_s)$ versus sample depth (z_s). These depth profiles are called A-scans, and variations exist depending on the scanning protocol: laterally adjacent A-scans form B-scans laterally adjacent A-scans at one depth form C-scans *(xy)*, A-scans monitored over time are called M-scans *(zt)* B-scans monitored over time are called M-B-scans *(xzt)* etc.
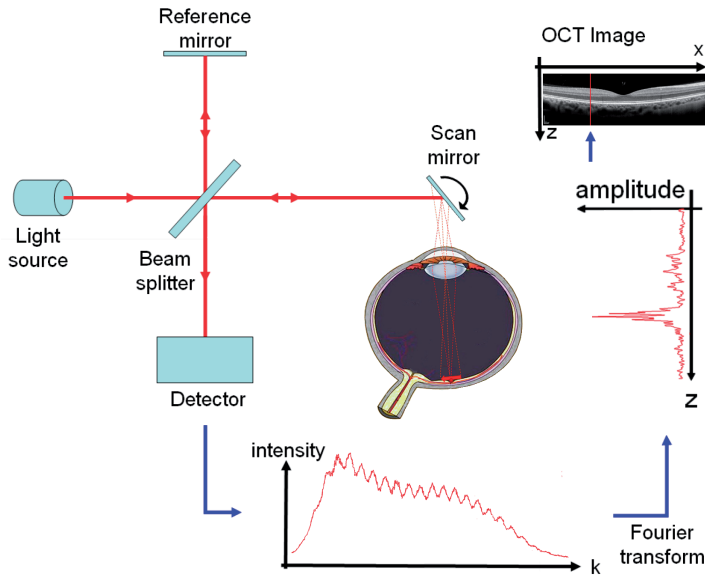
Figure 6. Basic spectral domain OCT system schematic and processing workflow.

SD-OCT has properties that are of interest to numerous medical disciplines, in particular ophthalmology. Its axial (depth) resolution depends only on the center wavelength (λ_0) and spectral bandwidth $(\Delta\lambda)$ of the source, *i.e.* completely decoupled from lateral resolution which also depends on the system optics.[75] OCT uses primarily infrared light in the range of 780 – 1300 nm. Although there is strong forward scattering and therefore high retinal tissue penetration in this range,[76] the drawback is the minimal amount of backscattered light necessary for signal generation. Infrared light is not only comfortable for viewing; infrared light sources with bandwidths $\Delta\lambda$ in the order of 10-100 nm allow a typical depth resolution of 10 µm or less at an arbitrary working distance.[77] SD-OCT can achieve a very high sensitivity (>100 dB dynamic range) and signal-to-noise ratio (50 dB) using low ocular exposure levels.[78] This signal-to-noise ratio is sufficient to detect subtle differences in light reflectivity from the various layers of the weakly backscattering retina.[77] Another interesting aspect of SD-OCT is confocality: the single-mode fiber serves as a pinhole aperture for both illumination and collection of light from the sample. The mathematical expressions for both the lateral- and depth-detected intensity reduce to that of an ideal confocal microscope with a diminishingly small pinhole aperture,[74] maximizing rejection of out-of-focus light at any sample location.

A tomogram (B-scan) of a healthy human retina is displayed in Fig 7, obtained with a commercial SD-OCT system. These images are typically displayed in log-scale intensity, where the original values $(R_s(z_s))$ are a measure of the number of photons scattered back towards the sample fiber (reflected). Four aspects cause variability in the number of photons backscattered to the OCT sample fiber, leading to variable signal intensity in the retinal OCT

scans. 1) Reflectance at the interface between two materials increases as their refractive index difference increases. 2) Most materials in the retina have diffuse reflective properties, 3) not all interfaces are orthogonal to the incident light beam, and 4) certain tissues can show birefringence, *i.e.* reflectivity depends on the light polarization state. An example of birefringent tissue is the Henle fiber layer,[79] which shows increased reflectivity as the OCT beam's angle of incidence approaches normal to the obliquely oriented axon fibers in this layer.[80]
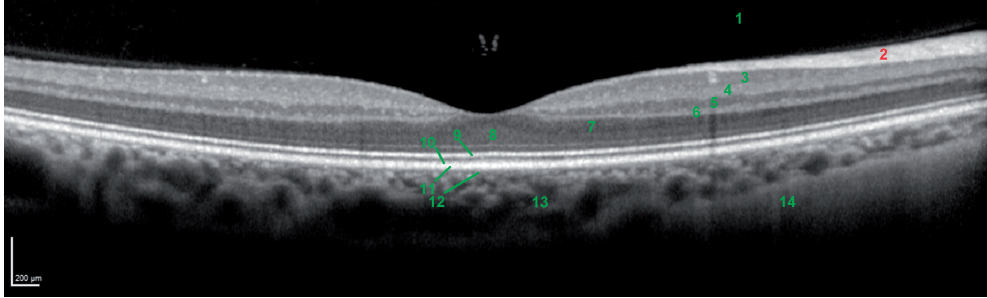
Figure 7. Fovea-centered SD-OCT scan from a healthy eye, showing various layers of the retina. Vitreous fluid (1), retinal nerve fiber layer (2), ganglion cell layer (3), inner plexiform layer (4), inner nuclear layer (5), outer plexiform layer (6), Henle fiber layer (7), outer nuclear layer (8), photoreceptor inner/outer segment junction (9), photoreceptor outer segment – RPE interdigitation zone (10), RPE/Bruch's membrane complex (11), choriocapillaris (12), choroid (13), sclera (14). The retina is displayed anatomically incorrect for better visualization of the layers; the current isotropic pixel aspect ratio (width:depth) should be reduced by factor 1.83; *i.e.* in reality the retina is flatter. Scale bar to the bottom left. Nomenclature follows ref. 81, except for layer 8. An imaging artifact is visible above the fovea.

1.5.1 SD–OCT as an imaging biomarker

OCT allows a quantitative diagnosis of various diseases, by not only visualizing pathological signs but also allowing measurements of layer thickness, tissue reflectivity and the volume of pathological fluid accumulations in or under the retina. For example, the identification of thinning of the nerve fiber layer is important for the early diagnosis of glaucoma, allowing the initiation of treatment as early as possible to limit or prevent irreversible loss of vision.[82, 83] Of particular clinical interest is the strong reflectivity in the photoreceptor-RPE complex. Using OCT devices with enhanced depth resolution (ultrahigh-resolution OCT), and equipped with auxiliary systems for enhanced lateral resolution (adaptive optics) and reduced eye movements artifacts (retinal tracking and image registration post-acquisition), four reflective bands can be resolved in this complex. These include reflections from the external limiting membrane, the inner-outer segment junction, photoreceptor outer segment tips (Fig 8),[84] and the zone where outer segment tips interdigitate with RPE cell protrusions (interdigitation zone). Frequently however, the latter two are visualized as a single band. Disruptions, thickness changes, and reflectivity changes of the photoreceptor bands have been linked to loss of visual function in numerous retinal diseases. However, the absence of particular

bands does not necessarily indicate loss of structure. For example, loss of the inner-outer segment junction does not reflect loss of rods and cones.[85]
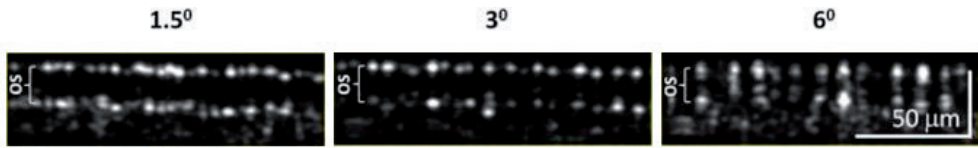
Figure 8. High-resolution SD-OCT B-scans, zoomed in at the cone outer segments (OS). Scans were acquired from a healthy retina at 1.5°, 3°, and 6° temporal to the fovea. Two rows of bright reflections can be observed: the photoreceptor inner-outer segment junction and the photoreceptor outer segment tips. Very weak reflections of the RPE layer directly below can also be seen.
(Kocaoglu *et al.*, *Biomed Opt Express*. 2011;2:748-763)[84]

1.5.2 Functional applications of OCT

As soon as OCT was developed, its potential for numerous functional applications beyond structural imaging was recognized.[75, 86] Presently, some of the most advanced applications include OCT's sensitive to birefringence (polarization-sensitive OCT), oxygenated hemoglobin (spectroscopic OCT), enhanced contrast of targeted molecules (contrast enhanced OCT),[87, 88] tissue elasticity (shear wave imaging OCT),[89] blood flow (OCT angiography), and stimulus-evoked intrinsic optical signals (IOS) indicative of hemodynamic activation and/or phototransduction (IOS-fOCT). This research focused on OCT angiography and IOS-fOCT.

1.5.3 OCT angiography

In OCT angiography blood flow is discriminated from static tissue by analyzing phase changes [90-93] or intensity changes [94, 95] in the OCT signal that are caused by moving light-scattering particles. Phase-based methods are insensitive to motion normal to the incident beam (*i.e.,* axial motion) and require phase-sensitive detection. Intensity-based methods make use of rapid fluctuations in the scattering pattern of blood flow, caused by a stream of randomly distributed blood cells through the imaging volume (voxel), leading to decorrelation of reflections in proportion to particle velocity. However, random speckle is an inherent property in OCT—like all interferometric techniques—which produces a grainy pattern through OCT images. In OCT angiography, speckle noise produces high decorrelation values throughout the flow image regardless of the actual sample reflectivity. Because of the randomness of these speckles, generated by the interference of waves with random phases,[75] simply averaging of multiple images of the same location suffices to suppress speckle. In OCT angiography, the assigning of zero decorrelation to locations with low reflectivity allows for the discrimination of motion from speckle noise.[96] Another aspect of intensity-based methods is that sensitivity to motion depends on the optical resolution along the axis of that motion. Therefore, OCT's high axial but lesser lateral resolution makes these methods highly susceptible to bulk axial motion of the sample,[97] caused by *e.g.* heartbeat and breathing.[98]

One intensity-based method, split-spectrum amplitude decorrelation angiography (SSADA), demonstrated high gains in the signal-to-noise ratio of flow detection due to an equalized sensitivity to flow in all three dimensions by equalizing axial and lateral resolution.[96] It has been incorporated in various commercialized SD-OCTs (Fig 9). It has already been shown that SSADA has great potential in advancing ophthalmic angiography. Indocyanine-green angiography (ICGA) makes use of a high-molecular weight fluorescent dye, excited at 780 nm, which binds to plasma proteins. Imaging by ICGA, like OCT, used infrared light that readily penetrates tissue and blood to clearly visualize the choroidal vasculature. However, neovascularization of choroidal vessels (CNV) is sometimes accompanied by leakage from the immature vessels, leading the abnormal vessels to be obscured by staining of fluid or blood ('occult' CNV). The selective sensitivity of SSADA to flow has even led some researchers to propose that a reliable diagnosis of CNV can only be made by SSADA without the need for dye-based angiography methods such as fluorescein angiography or ICGA.[99]
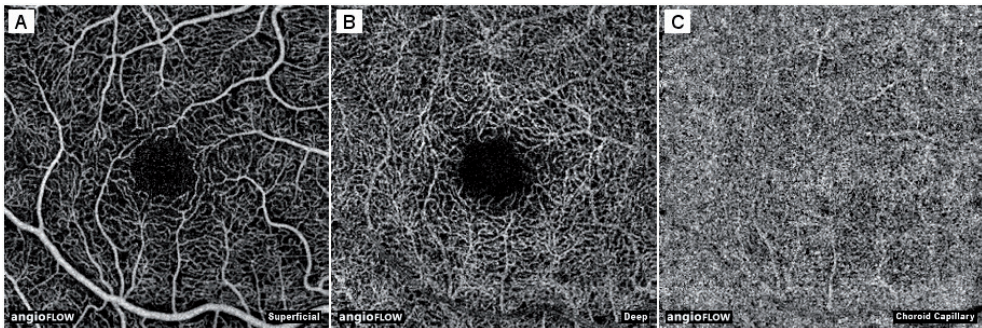
Figure 9. Example OCT angiography images of a healthy retina obtained with the SSADA technique, displaying axially average flow in three vascular compartments. Superficial retina showing the retinal vessels and capillary beds, including the inner limiting membrane, retinal nerve fiber layer, and ganglion cell layers (A). Deep retina, showing the deeper inner retinal capillary beds, including the inner plexiform layer, inner nuclear layer, and outer plexiform layer (B). Choriocapillaris, showing the chroroidal capillary bed, defined as 10 μm below Bruch's membrane directly below the RPE (C).

1.5.4 Intrinsic optical signal imaging

IOS reflect transient changes in the intrinsic optical properties of tissue detectable with optical microscopy. Their detection does not require extrinsic probes such as voltage sensitive dyes or fluorescent labels. In short, the method involves the continuous monitoring of a tissue volume for seconds to minutes, while an appropriate stimulus is delivered to evoke the signal. IOS were first reported as an approach to measure neural activity in optically accessible regions of the brain, such as the surface of the—surgically exposed—visual cortex. [100, 101] Red or infrared light is frequently useful to probe for these changes, because neurons show little if any response to these wavelengths. SD-OCT is useful to probe for IOS in the

retina due to its high optical accessibility, neuronal composition, and because SD-OCT provides the distinct advantages of imaging at high spatiotemporal resolution in 3D and sensitivity to small changes in reflectivity. At present, the only truly objective functional retinal assessments at the disposal of ophthalmologists are electroretinography (ERG) and fundus densitometry. Both these techniques have their limitations. ERG and its variants measure electrical responses from discrete populations of retinal neurons to standardized visual stimuli in either the whole retina (full-field ERG) or in subfields, such as the 200 μm diameter fields of multifocal ERG. Fundus densitometry quantifies light absorption in photoreceptors as a measure of the concentration of light-absorptive visual pigments, although it does not detect if phototransduction indeed occurs in photoreceptors with adequate pigment. In this context, IOS-fOCT could provide useful additional information by displaying retinal function (phototransduction) together with high-resolution structural information in one examination. It could be particularly attractive for fine-mapping of functionality in locations that appear to have a (partially) atrophic structure, but that may not be objectively detected with either multifocal ERG's limited resolution or with the limited reliability of subjective microperimetry tests.

1.6 Aim and Outline of this thesis

This research is focused on 1) the discovery of novel imaging biomarkers and 2) the deepening of our understanding of existing imaging biomarkers of the retina and choroid, and 3) their use in assessing the progression of ocular diseases. First, single- and multimodal imaging, including – but not limited to – fundus autofluorescence (AF) and structural OCT, were used to study longitudinal changes in Stargardt disease and birdshot chorioretinopathy. Second, the risks of using AF imaging in patients with potential susceptibility to short-wavelength light were examined. Third, a novel OCT-based functional imaging biomarker for the detection of functional, *i.e.* light-responsive, photoreceptors has been investigated. Fourth, a novel OCT-based assessment of chorioretinal blood flow was used to investigate blood flow abnormalities in central serous chorioretinopathy.

Chapter 2.

Fundus autofluorescence imaging

Chapter 2.1

The effect of light deprivation in patients with Stargardt disease

Michel M. Teussink
Michele D. Lee
R. Theodore Smith
Ramon A.C. van Huet
Caroline C.K. Klaver
B. Jeroen Klevering
Thomas Theelen
Carel B. Hoyng

Abstract

Purpose. To investigate whether long-term protection from light exposure affects the rate of disease progression in patients with autosomal recessive Stargardt disease (STGD1), measured using fundus autofluorescence imaging.

Design. Longitudinal, retrospective, interventional case series.

Methods. Five patients with Stargardt disease protected one eye from light exposure by applying a black contact lens during waking hours for ≥12 months. Disease progression was followed by performing autofluorescence imaging at semi-regular intervals. Longitudinal changes in autofluorescence were studied by evaluating areas of decreased autofluorescence and areas of increased autofluorescence as a measure of retinal pigment epithelium damage and lipofuscin accumulation, respectively.

Results. We observed less progression of decreased autofluorescence in 4 (80%) out of 5 light-protected eyes relative to their respective non-protected eyes. The progression of increased autofluorescence was highly variable and did not respond consistently to treatment.

Conclusions. Areas of decreased autofluorescence may serve as a useful biomarker for measuring the progression of Stargardt disease. The reduced progression of decreased autofluorescence in the light-protected eyes suggests that light deprivation might be beneficial in patients with Stargardt disease.

Introduction

Autosomal recessive Stargardt disease (STGD1) is the most common inherited juvenile macular degeneration.[102] Most patients develop bilateral loss of vision in childhood or early adulthood. This subtype of Stargardt disease is caused by mutations in the *ABCA4* gene, which encodes a retina-specific transporter protein (ABCR) in the rims of rod and cone photoreceptor outer segment discs.[61, 103, 104] Retinal degeneration in *ABCA4*-linked Stargardt disease is believed to result from the toxic effects of lipofuscin that accumulates in the retinal pigment epithelium (RPE) and the subsequent degeneration of photoreceptors.[25]

Light can induce photochemical injury at the ocular fundus. Depending on the level and duration of the irradiance, the primary site of damage can be either the photoreceptors or the RPE.[105] In *ABCA4*-linked retinopathies, products generated by the visual cycle accumulate and contribute to retinal damage via both direct toxic effects and increased photosensitivity. A major fluorophore of lipofuscin, bisretinoid *N*-retinylidene-*N*-retinyl-ethanolamine (A2E), accumulates with other, currently unidentified lipofuscin constituents within the RPE.[106-108] Thus, an excessive accumulation of A2E has been observed in both *Abca4*$^{-/-}$ mice and patients with Stargardt disease.[25, 109] Lipofuscins (and A2E in particular) are potent photosensitizers[11-14] that can induce oxidative damage, thereby accelerating light-induced retinal damage and RPE atrophy.[110-112] This oxidative damage may affect the rate of disease progression in patients with Stargardt disease.

The total quantity of A2E oxiranes in *Abca4*$^{-/-}$ mice increases in response to light exposure.[113] In addition, a recent review of light-induced and inherited retinal degenerations suggested that light exposure might modify the disease course of genetically well-defined retinal dystrophies, including Stargardt disease.[114] An early study used functional and ophthalmoscopic examinations to test the effect of five years of unilateral light deprivation in a patient with autosomal recessive retinitis pigmentosa and in a patient with autosomal dominant retinitis pigmentosa; the author observed symmetrical disease progression.[115] However, in the absence of a genetic diagnosis, and without clear insight into the pathogenesis of these two RP patients, no conclusions can be drawn with respect to patients with Stargardt disease.

Because the aforementioned results suggest that patients with Stargardt disease might be more sensitive to light, we considered using light protection as a means to slow disease progression in patients with Stargardt disease. Therefore, we retrospectively examined the effects of using a single black contact lens in an attempt to spare disease progression in one eye in patients with Stargardt disease. We followed disease progression in five patients using the fundus autofluorescence imaging data, as this test provides a sensitive, non-invasive measure of RPE abnormalities and lipofuscin accumulation in patients with Stargardt disease.[116-118]

Methods

This study was a longitudinal, retrospective, interventional case series of patients diagnosed with Stargardt disease. The intervention was applied in the context of clinical care at the request of the patients (or legal guardian) and not in the context of a prospective clinical trial. Therefore, nonstandard analyses (*e.g.*, routine imaging) were performed to ensure internal quality control and to detect any adverse events in a timely manner. All patients had been diagnosed previously as having Stargardt disease with at least one *ABCA4* mutation, and all patients presented with the typical clinical symptoms associated with this retinal dystrophy.

All genetic analyses were performed by the Department of Human Genetics at Radboud University Medical Center (Nijmegen, the Netherlands). Patients were screened for known *ABCA4* mutations using the arrayed primer extension microarray (Asper Biotech, Tartu, Estonia), and exon duplications and/or deletions were detected using multiplex ligation-dependent probe amplification (P151 and P152, MRC-Holland, Amsterdam, the Netherlands). If no mutations—or only a single heterozygous mutation—were identified, the exons and intron-exon boundaries were sequenced using the Sanger method to screen for mutations in the other allele. All identified mutations were confirmed using Sanger sequencing.

The study was performed in accordance with the tenets established by the Declaration of Helsinki, and informed consent was obtained from all patients (or from the legal guardians of underage patients) for a retrospective analysis of therapy-related data. Patients were previously advised regarding the potential benefits of wearing sunglasses, avoiding direct light exposure, and limiting their dietary intake of vitamin A.[119] Complete protection from light exposure was suggested as a treatment option to patients who had a pressing request for any potentially effective treatment, given the current absence of suitable treatments for Stargardt disease. The institutional review board (*Commissie Mensgebonden Onderzoek*, Region Arnhem-Nijmegen) retrospectively approved this study (2013/062) after the last patient's final visit and during the study.

Patients were enrolled in the study and followed from January 2006 through December 2009 at the clinical practice of Radboud University Medical Center, Nijmegen. After eliminating any medical concerns regarding the use of contact lenses, we suggested that the patients protect their intuitively best eye (determined at the time of enrolment) during waking hours for at least one year using a black contact lens. The age of disease onset was defined as the age at which visual loss was first recorded. Best-corrected visual acuity (BCVA) was measured using a Snellen chart or the finger-counting method. To provide the most complete light protection, a customized, black, soft contact lens designed to cover the entire cornea (Ercon, Assen, the Netherlands) was applied; this lens blocked >90% of light in the visible spectrum.

Patients underwent a routine ophthalmological examination, including BCVA, slit-lamp examination, binocular funduscopy, and confocal fundus autofluorescence imaging of both eyes with a Spectralis device (Heidelberg Engineering, Heidelberg, Germany). After pharmacological pupil dilation to ≥6 mm with phenylephrine 2.5% and tropicamide 0.5% eye drops, we recorded fundus autofluorescence images centered on the fovea and including part of the optic disc; images were obtained using an excitation wavelength of 488 nm and a barrier filter (≥500 nm) in high-resolution mode (30° field of view, 1536 pixels x 1536 pixels). Baseline and follow-up images of both eyes were captured with equal system sensitivity settings. Clinical phenotyping was performed in accordance with Fishman *et al.* (1999)[120] by an experienced clinician (author R.H.) who was blinded with respect to the study results. Fundus autofluorescence was used to phenotype the disease stages as described by Cideciyan *et al.*[121]

Fundus autofluorescence images were acquired using a standard procedure as follows. First, focusing was performed using the near-infrared reflection mode of the Spectralis. To account for chromatic aberrations, slight re-focusing in the autofluorescence mode was performed, and nine separate images were acquired after sensitivity adjustment, thereby covering the entire macular area and including part of the optic disc. To increase the signal-to-noise ratio, all images were aligned and a mean image was calculated using the internal software (without normalization by histogram stretch). All other image processing and analysis were performed using scripts written in MatLab (R2006; MathWorks, Natick, Massachusetts). Initial and final fundus autofluorescence images were automatically registered as reported previously.[116] The alignment of each image pair was manually confirmed; if necessary, registration was adjusted iteratively until a satisfactory result was obtained. Pixel size was normalized to the fovea-disc margin distance.[122]

Increased autofluorescence and/or decreased autofluorescence relative to the image background was quantified by an observer (author M.L.; this author was blinded with respect to the treated eye) based on non-normalized mean images as published previously.[116, 123, 124] In brief, each fundus autofluorescence image was leveled by subtracting a 12-zone quadratic polynomial mathematical model of the image's background autofluorescence, which was calculated for each image. The threshold for increased or decreased autofluorescence was set at 1.5 x σ above or below, respectively, the mean pixel intensity of the resulting image. Consistent with previous reports,[116] we found that this threshold provided the best detection of visually evident autofluorescence abnormalities. In some cases, the precise location of the fovea could not be determined due to pathologic changes; in such cases, determining where to place the center of the quadratic polynomial model was questionable. Therefore, we adjusted the model's position slightly until the selection of any visually evident autofluorescence abnormalities was optimized. For some images, multiple re-positioning of the model was required in order to capture all autofluorescence abnormalities; in these cases, we combined

the resulting pixels showing increased and/or decreased autofluorescence, respectively. Pixels that were identified incorrectly in vessels and/or bifurcations were removed manually. The total number of pixels showing increased and/or decreased autofluorescence were measured in each image, and the annual rate of change in decreased autofluorescence (change in decreased AF) in serial image pairs of the right eye (OD) was calculated as follows:

$$\% \text{ Change in decreased AF (OD)/ yr} =$$

$$\left(\frac{\text{Decreased AF}_{post} \text{ (OD)} - \text{Decreased AF}_{pre} \text{ (OD)}}{\text{Decreased AF}_{pre} \text{ (OD)} + \text{Decreased AF}_{pre} \text{ (OS)}} \right) \cdot 100\% \cdot \left[\text{Time between images (yr)} \right]^{-1}.$$

The annual rate of change in the left eye (OS) was calculated as follows:

$$\% \text{ Change in decreased AF (OS)/ yr} =$$

$$\left(\frac{\text{Decreased AF}_{post} \text{ (OS)} - \text{Decreased AF}_{pre} \text{ (OS)}}{\text{Decreased AF}_{pre} \text{ (OD)} + \text{Decreased AF}_{pre} \text{ (OS)}} \right) \cdot 100\% \cdot \left[\text{Time between images (yr)} \right]^{-1}.$$

Dividing by the total initial number of pixels showing decreased autofluorescence in both eyes minimized potential artificial increases in progression that might have arisen when the initial quantity in one eye was low. To evaluate the progression of decreased autofluorescence in the light-protected eye, we normalized its progression to the control (non-protected) eye as follows:

$$\text{Progression of decreased AF (normalized)} =$$

$$\left(1 - \left(\frac{\% \text{ Change in decreased AF}_{untreated} / \text{ yr} - \% \text{ Change in decreased AF}_{treated} / \text{ yr}}{\left| \% \text{ Change in decreased AF}_{untreated} / \text{ yr} \right|} \right) \right) \cdot 100\%.$$

All calculations were performed for annual changes in increased autofluorescence. Statistical analyses were not performed due to the relatively small sample size and the absence of empirical data regarding the progression of altered autofluorescence under conditions of light deprivation.

Results

The patients' demographics and clinical data are summarized in Table 1. Five Caucasian patients (3 male, 2 female) with Stargardt disease (mean age at inclusion was 22.6 years; range: 10-46 years) enrolled and completed the treatment with a mean follow-up period of 17.8 months (range: 11-26 months). We identified disease-related mutations in both *ABCA4* alleles of four patients; only one *ABCA4* mutation was identified in patient #5.

Table 1. Demographics, genetics and clinical appearance of five patients with Stargardt disease

Patient	Gender	Age at inclusion (years)	Age at onset (years)	Disease duration (months)	Follow-up period (months)	Eye	Initial BCVA	Final BCVA	Mutation allele 1	Mutation allele 2	Ophthalmoscopy	Fluorescence angiography	Electroretinography	Stargardt phenotype[a]
1	F	20	19	41	28	OD	20/40	20/100	c.768G>T	c.872C>T	Yellowish white flecks in parafoveal area, central parafoveal pigment alterations, bull's eye-like appearance.	No dark choroid.	Within normal limits.	PF
						OS*	20/40	20/100						
2	F	46	46	32	27	OD	20/16	20/16	c.2588G>C c.656G>C[b]	c.2828G>A	Yellowish flecks throughout the posterior pole extending anterior to the vascular arcades and peripapillary region.	No dark choroid, but cSLO recording, which may mask the dark choroid sign.	Within normal limits.	FF
						OS*	20/12.5	20/20						
3	M	10	10	22	13	OD*	20/400	20/400	c.3335C>A	c.5461 - 10T>C	Yellowish white flecks in para- and perifoveal area, central RPE alterations.	No dark choroid.	OD Photopic: moderately reduced, OS pathologically reduced (lowered amplitude).	PF
						OS	20/400	20/400						
4	M	13	11	53	29	OD	20/125	20/160	c.2588G>C	c.4539 +1G>T	Central RPE alterations and widespread atrophic lesions throughout the posterior pole extending anterior to the vascular arcades.	Diffuse hyperfluorescent lesions.	Photopic moderately reduced.	DA
						OS*	20/125	20/125						
5	M	24	12.3	284	12	OD	20/400	CF	c.IVS39> - 10T>C	NF	Central RPE alterations with intraretinal pigmentations. Small atrophic lesions (presumably resorbed yellow flecks) scattered throughout the posterior pole extending anterior to the vascular arcades.	Not performed.	OD and OS photopic moderately reduced, OD scotopic moderately reduced, OS scotopic pathologically reduced.	DA
						OS*	CF	CF						
Mean		23	18	86	22									
SD		14	17	111	9									

F = female; M = male; Disease duration = time between age at onset of the disease and the final image; OD = right eye; OS = left eye; * = the treated (light-protected) eye; BCVA = best-corrected Snellen visual acuity; CF = Finger counting; Mutation allele 1 or 2 = mutations in the *ABCA4* gene; NF = not found; RPE = retinal pigment epithelium; cSLO = confocal scanning laser ophthalmoscopy; PF = perifoveal type; FF = fundus flavimaculatus type; DA = diffuse atrophic type.

[a] As defined by Fishman *et al.* (1999). [120]

[b] Allele unknown

Chapter 2

Treatment compliance was assumed based on information provided by the patients or their legal guardians, and they reported that they complied. The course of BCVA was similar in both eyes of each patient and was stable in all but one patient (patient #1) throughout the study period. In patient #2, whose BCVA was stable throughout the study, bilateral nuclear cataract was identified at the final follow-up visit. No geographic atrophy was observed in any patient throughout the study period. None of the study participants developed any contact lens–related adverse events or signs of deprivation amblyopia.

Figure 10 shows the characteristic fundus autofluorescence appearance in one patient during the study period. All five patients presented with a complex textural fundus autofluorescence appearance (*i.e.,* lesions of increased or decreased fundus autofluorescence). Central diffuse hypofluorescent areas were present in the initial images of four patients; however, these areas were not sharply demarcated and had stronger signals than would be expected in areas of geographic atrophy in Stargardt disease.[116]

During the study period, pixels showing increased and/or decreased autofluorescence emerged, disappeared, and/or changed (*i.e.,* from an increase to a decrease or vice versa). We observed that the temporal sequence of autofluorescence changes was heterogeneous both between patients and between a given patient's eyes *(e.g.,* some hypoautofluorescent areas expanded, but also regressed partially into the background autofluorescence). This heterogeneity was observed in visually evident lesions as well as in lesion-free areas. Progression analysis was performed in accordance with Cideciyan *et al.*[121] and revealed that all five patients progressed during the study period; one, two, and two patients progressed to stage 3, stage 4, and stage 5, respectively.

The total number of pixels showing decreased autofluorescence generally increased in all but one eye. However, in four of the five patients, the normalized annual progression rate in the light-protected eye was less severe compared to the respective untreated eye (Figure 11). In one patient, we observed the opposite pattern; in patient #3, the progression of decreased autofluorescence was slightly higher in the light-protected eye than in the control eye. On the other hand, the progression of increased autofluorescence was more variable than the progression of decreased autofluorescence; increased autofluorescence developed symmetrically (*i.e.,* with similar progression in both the light-protected and untreated eye) in all patients. The results of our autofluorescence analysis are summarized in Table 2.
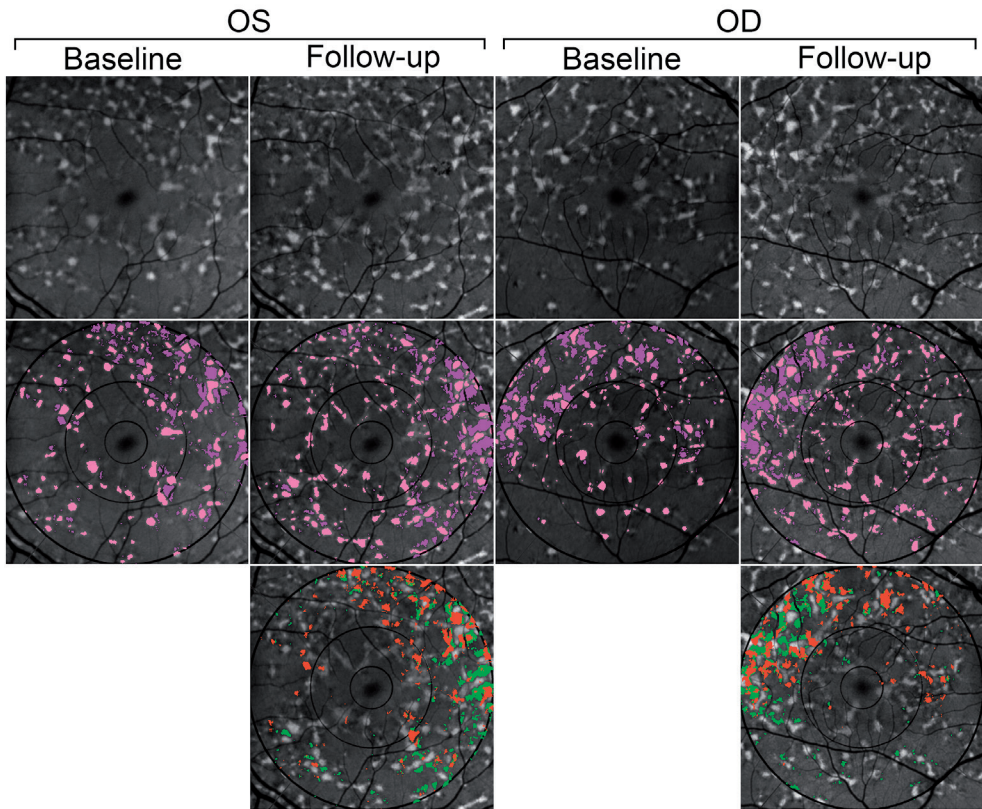
Figure 10. Example of autofluorescence in a patient with Stargardt disease. Fundus autofluorescence was measured and analyzed in a patient with Stargardt disease (patient #2). The left eye (OS) was protected from light exposure using a black contact lens for 24.4 months (see Methods); the right eye (OD) was not light-protected. The top row shows original, non-segmented autofluorescence images; the middle row shows increased autofluorescence (pink) and decreased autofluorescence (purple) segmentation. The bottom row shows the longitudinal change analysis of pixels showing decreased autofluorescence; baseline autofluorescence is shown in orange, and autofluorescence at follow-up is shown in green. The grids demarcate the retinal areas analyzed; the outer radius is 500 pixels adjusted to the fovea-disc margin distance.[122]
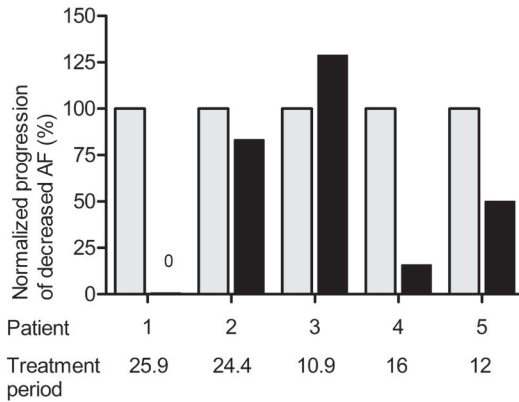
Figure 11. Summary of the effect of light exposure on the progression of decreased autofluorescence in five patients with Stargardt disease. Normalized progression of decreased autofluorescence measured in the light-protected eyes (black bars) and the untreated eyes (gray bars) of five patients. The progression of decreased autofluorescence was reduced in patients #1, 2, 4, and 5; in contrast, patient #3 had more progression in the light-protected eye compared to the untreated eye. The value below each patient indicates the treatment duration in months.

Table 2. Course of fundus autofluorescence in five patients with Stargardt disease

Patient	Eye	Treatment period (months)	Initial FIAF (pixels)	Final FIAF (pixels)	FIAF change %/yr	Initial FDAF (pixels)	Final FDAF (pixels)	FDAF change %/yr
1	OD		1664	326	-16.6	88	199	22.6
	OS*	25.9	1897	431	-18.2	129	129	0.0
2	OD		3894	6160	11.6	4231	4342	0.6
	OS*	24.4	4650	5745	5.6	4117	4214	0.5
3	OD*	10.9	1464	750	-15.4	12172	14395	6.7
	OS		2720	1859	-18.6	17665	19394	5.2
4	OD		2946	1302	-16.9	4583	4987	1.9
	OS*	16.0	1127	329	-8.2	4098	4153	0.3
5	OD		1613	2663	27.0	29546	35152	10.4
	OS*	12.0	2284	3636	34.7	24363	27187	5.2
Mean		17.8	2426	2320	-1.5	10099	11415	5.4
StDev		7.0	1136	2200	20.1	10432	12174	7.0

OD = right eye; OS = left eye; * = the study eye; FIAF = focal areas of increased autofluorescence; FDAF = focal areas of decreased autofluorescence; yr = year

Images were registered and adjusted for pixel size (*i.e.*, the fovea-disc distance had identical pixel numbers in follow-up series). Total numbers of pixels showing increased and/or decreased autofluorescence in initial and final images were measured, and yearly changes in the numbers of pixels showing increased and/or decreased autofluorescence were calculated as a percentage of the total number in the initial images of both eyes (as % FIAF/yr and % FDAF/yr, respectively).

Discussion

Here, we report the effect of using a black contact lens to protect the eye from light exposure in patients with Stargardt disease. We observed less progression of decreased autofluorescence in four out of five light-protected eyes compared to the patients' unprotected eyes. In contrast, we found no effect of light protection on the progression of increased autofluorescence. Despite an extensive literature search (for details, see Appendix), we were unable to find any published reports regarding the effect of light protection in patients with Stargardt disease.

A recent study using the *Abca4*^{-/-} mouse model found that the accumulation of lipofuscin in the retina makes the retina more vulnerable to the effects of light with respect to disease progression.[125] How increased levels of lipofuscin lead to photoreceptor degeneration and visual loss in patients with Stargardt disease is poorly understood. Photo-oxidative processes appear to accelerate cell damage in retinas that have increased lipofuscin levels following light exposure.[125, 126] The primary site of this light-induced damage in patients with Stargardt disease could be photoreceptor outer segments, the RPE, or both. For instance, prolonged light exposure may cause primary photoreceptor cell damage by allowing photopigment regeneration and subsequent repeated bleaching, which may promote the formation of bisretinoids in photoreceptor cells. Due to outer segment shedding, however, bisretinoids in photoreceptor cells are kept to a minimum and instead accumulate in the RPE. Although some studies of light damage have reported the greatest damage in the RPE,[127-132] others have reported damage in both the RPE and photoreceptors.[125]

Patients with Stargardt disease can develop increased or decreased autofluorescence compared to background autofluorescence. In Stargardt disease, pixels showing increased and/or decreased autofluorescence tend to be unstable and can vary with respect to the temporal sequence of autofluorescence changes.[116] Whether a given fundus area with background, increased, or decreased autofluorescence will develop a focal increase and/or decrease in autofluorescence cannot be predicted at baseline; such a change depends on the stage of the disease in that specific area.[133] In our study, we quantified the increased and/or decreased autofluorescence relative to background autofluorescence. Because we did not measure autofluorescence quantitatively,[134] we cannot conclude whether background autofluorescence—and by extension, lipofuscin—is equal to, higher than, or lower than normal in a given patient. Therefore, in contrast to well-defined areas of geographic atrophy, pixels showing decreased autofluorescence may not necessarily reflect total RPE atrophy in that region. Pixels showing decreased autofluorescence may therefore represent decreased, normal, or even increased autofluorescence compared to age-matched healthy subjects. Nevertheless, pixels showing decreased autofluorescence (which was referred to in 2009 by Smith *et al.*[116] as "focally decreased autofluorescence") suggest RPE cell damage.[116] Because recent quantitative measurements showed that background autofluorescence is nearly

always increased in Stargardt disease (compared to age-matched controls),[135] pixels showing increased autofluorescence should indicate increased autofluorescence values in general. Pixels showing increased autofluorescence may therefore be interpreted as an increase in lipofuscin, even when precise quantification is not available.

We observed that a pixel showing increased autofluorescence could change to decreased autofluorescence; however, it could also remain increased or even return to background autofluorescence levels. On the other hand, pixels showing decreased autofluorescence could emerge from background autofluorescence or increased autofluorescence. As discussed above, a pixel showing increased autofluorescence suggests a focal area of increased levels of fluorophores such as lipofuscin and lipofuscin bisretinoids. Thus, our data suggest that light protection does not affect the progression of focal lipofuscin accumulation.

Interestingly, the three youngest patients in our cohort (patients #1, 3, and 4) had a decrease in the number of pixels showing increased autofluorescence even in the light-protected eye. It should be noted that patients #1, 3, 4, and 5 were classified as having early-onset Stargardt disease and were included in a recent study conducted by our department.[136] This decrease—in combination with an increase in the number of pixels showing decreased autofluorescence in patients #1, 3, and 4—is likely associated with a trend of decreasing overall autofluorescence.[116] This trend may be more pronounced when the disease progresses rapidly, as occurs in early-onset Stargardt disease.[136] Patients #3 and 5, however, had an extremely large central diffuse hypoautofluorescent lesion and a large number of pixels showing decreased autofluorescence. This finding suggests more destructive disease, as suggested by Lambertus *et al.*[136]

On the other hand, decreased autofluorescence appeared to be associated with light exposure in our cohort; in other words, light deprivation reduced the progression of decreased autofluorescence in four of five patients. Irradiance with visible light of sufficient intensity photobleaches lipofuscin autofluorescence in RPE cells, and primary RPE damage with no anatomical changes in the retinal photoreceptors can occur following exposure to visible light.[126, 137] In *Abca4* [-/-] mice, light damage in the RPE can also be caused by toxicity due to increased bisretinoids and their oxidation products.[125] Therefore, it is likely that excessive light exposure is harmful to patients with Stargardt disease. Other lines of evidence suggest that blue light may be primarily responsible for this damage.[138-141] Therefore, eyeglasses or contact lenses that filter out short-wavelength light might be a viable alternative to total light deprivation.

The advantage of our study is that we compared each light-protected eye to the untreated eye in the same patient, providing each treated eye with its own internal control. By comparing the light-protected eye to the untreated eye in the same patient, both genetic and environmental effects (aside from the use of the contact lens) were minimized.

On the other hand, this study also has several potential limitations. First, we studied a relatively small number of patients with a range of ages and in various stages of Stargardt disease. Therefore, our cohort included eyes in different disease stages and eyes with different degrees of lipofuscin accumulation. However, we included only patients with recent subjective and objective progression, strong motivation to participate in this durable treatment, and no contraindication to contact lens use. Moreover, our approach to light-deprive the subjectively better eye may have influenced our results. However, we believe that any selection bias was unlikely, as the disease was symmetrical at the start of treatment with respect to both functional and anatomical examination (shown using BCVA, funduscopy, and the number of pixels showing increased autofluorescence and decreased autofluorescence). In addition, randomization was not possible, as this was not a prospective clinical trial. The treating physician (author C.H.) felt that any treatment—if effective— should be applied to the subjectively better eye in an attempt to preserve function in that eye.

Furthermore, because this study was not performed prospectively, it relied on retrospective data analysis. Therefore, autofluorescence imaging was not performed using a standardized protocol, nor were the images obtained at predetermined time points. Moreover, media opacity and pupil dilation—two potential confounders of autofluorescence—were not routinely measured before imaging. Taken together, our study was subject to two specific form of selection bias: *i*) the strong motivation of the patients to participate in this study, and *ii*) our retrospective quality selection of the imaging data.

Consistent with previous studies, our study was designed to observe the progression of increased autofluorescence and/or decreased autofluorescence during a specific period of time and to identify any difference in progression between the untreated and treated eyes in the same patient.[116] However, our study did not follow the continuous development of changes in autofluorescence over a prolonged interval (*i.e.*, until geographic atrophy and vision loss occurred). A long-term prospective study including more frequent and regular measurements using standardized autofluorescence imaging over several years might help address the important question of whether light protection can delay vision loss—rather than merely delaying focal RPE damage—in patients with Stargardt disease. Moreover, adding quantitative autofluorescence imaging to future study protocols would be highly informative. Unfortunately, appropriate research tools for normalizing autofluorescence grayscale values to an internal reference[134] were not available at the time of our study.

In conclusion, our results suggest that decreased autofluorescence may serve as a biomarker for disease progression in patients with Stargardt disease. Under light-deprivation conditions, we found reduced overall progression of decreased autofluorescence compared with the untreated eye, suggesting a reduction in the rate of RPE damage in the treated eye. Our data suggest that light deprivation may confer a protective effect in patients with Stargardt disease and therefore merits further investigation.

Appendix

An extensive literature search was performed using the following search string in the PubMed database (available at http://www.ncbi.nlm.nih.gov/). The search was performed at 2nd of November, 2014.

```
(irradiation[tiab] OR irradiations[tiab] OR photoradiation[tiab] OR
photoradiations[tiab] OR radiations[tiab] OR illumination[tiab]  OR light[tiab]
OR photo[tiab]  OR (intraocular[tiab]  AND light[tiab])) AND

((treat[tiab]  OR treatment[tiab]  OR treated[tiab]) OR (protect[tiab]  OR
protection[tiab]  OR protected[tiab]) OR (filter[tiab]  OR filtering[tiab]  OR
filtered[tiab]) OR (shield[tiab]  OR shielding[tiab]  OR shielded[tiab]  OR
block[tiab]  OR blocking[tiab]  OR blocked[tiab]) OR (avoid[tiab]   OR
avoidance[tiab]   OR avoided[tiab]) OR (deprived[tiab] OR deprivation[tiab] OR
deprive[tiab])) AND

(fundi[tiab] OR fundus[tiab] OR  "retina"[MeSH Terms] OR "retina"[tiab] OR
retinal[tiab] OR retinas[tiab] OR "macula"[tiab] OR maculas[tiab] OR
"macular"[tiab] OR "fovea"[tiab] OR "foveal"[tiab] OR "foveas"[tiab] OR
photoreceptor[tiab] OR photoreceptors[tiab] OR "cone"[tiab] OR cones[tiab] OR
rod[tiab] OR rods[tiab]OR amacrine[tiab] OR (horizontal[tiab] AND (cell[tiab] OR
cells[tiab])) OR (optic[tiab] AND (disk[tiab] OR disc[tiab])) OR choroid[tiab] OR
choroid[mesh]) AND

("Stargardt Macular Degeneration" [Supplementary Concept] OR "Stargardt disease 1"
[Supplementary Concept] OR "Stargardt disease 3" [Supplementary Concept] OR
Stargardt[tiab] OR Fundus Flavimaculatus [tiab] OR STGD[tiab] OR STGD1[tiab] OR
STGD3 [tiab] OR STGD4 [tiab]) OR (abca4[tiab] OR ((ABC1[tiab] OR ABC[tiab]) AND
(transporter[tiab] OR transporters[tiab]) AND (photoreceptor[tiab] OR
photoreceptor[tiab])) OR ((ATP-Binding Cassette Transporters [Mesh]) AND
(photoreceptor cells [Mesh] OR photoreceptor [tiab] OR retina [Mesh] OR retina
[tiab]) OR (rim[tiab] AND (protein[tiab] OR proteins [tiab]) OR Abcr[tiab]))) AND

(patient[tiab] OR patients[tiab] OR trial[tiab] OR (clinical[tiab] AND
trial[tiab]))

NOT (tuberculosis[tiab]  OR tuberculous[tiab] OR tubercular[tiab] OR
bacterial[tiab]  OR bacterium[tiab]  OR bacillary[tiab] OR tumor[tiab]  OR
tumors[tiab] OR rifampicin[tiab] or (regional[tiab] AND myocardial[tiab] AND
perfusion[tiab]))
```
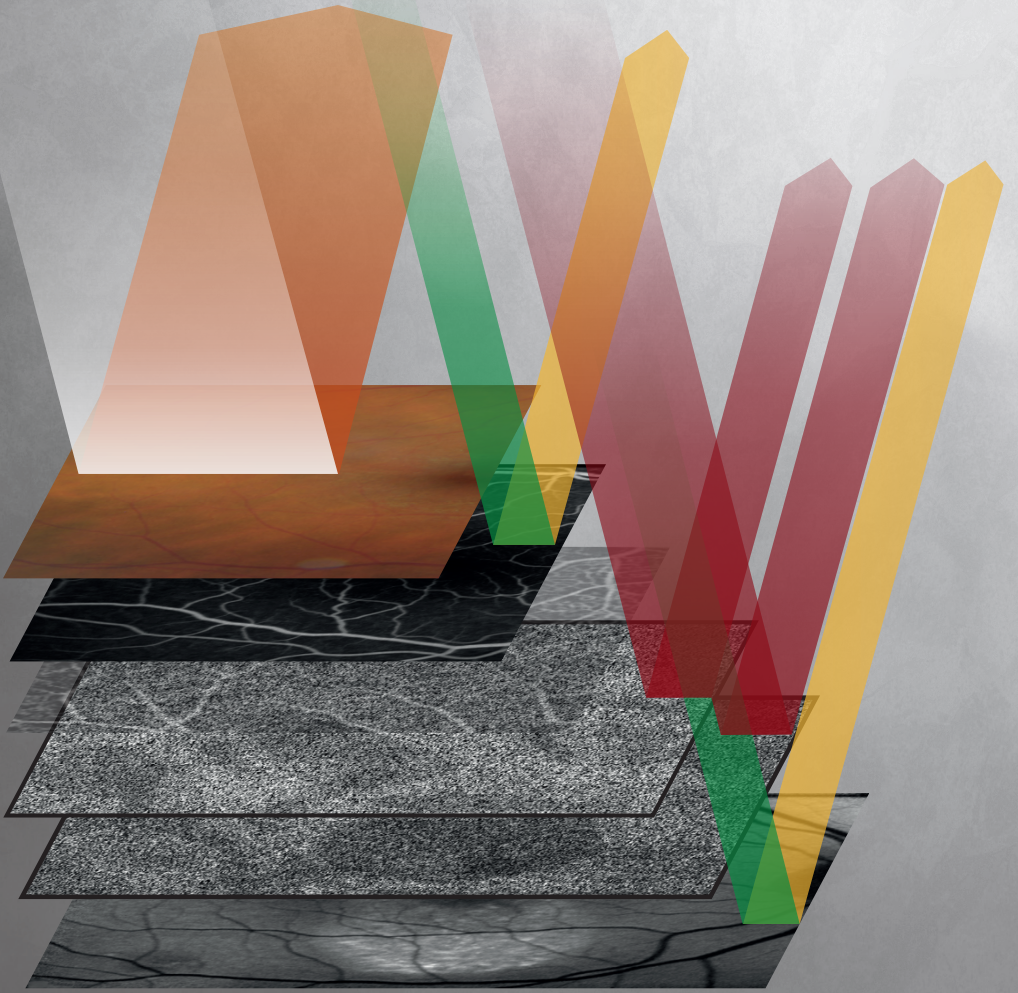
Chapter 2.2

Multimodal imaging of the disease progression of birdshot chorioretinopathy

Michel M. Teussink
Paulien I. Huis in het Veld
Lieuwe A.M. de Vries
Carel B. Hoyng
B. Jeroen Klevering
Thomas Theelen

Abstract

Purpose. To study outer retinal deterioration in relation to clinical disease activity in patients with birdshot chorioretinopathy using fundus autofluorescence and spectral-domain optical coherence tomography (OCT).

Methods. A single-centre retrospective cohort study was carried out on 42 eyes of 21 patients with birdshot disease, using a multimodal imaging approach including fundus autofluorescence, OCT, fluorescein angiography and indocyanine green angiography in combination with a patient chart review. The patients' overall clinical activity of retinal vasculitis during the follow-up period was determined by periods of clinical activity as indicated by fluorescein angiography and associated treatment decisions. Image analysis was performed to examine the spatial correspondence between autofluorescence changes and disruption of the photoreceptor inner segment ellipsoid zone on OCT.

Results. Three common types of outer retinal lesions were observed in fovea-centred images of 43% of patients: circular patches of chorioretinal atrophy, ellipsoid zone disruption on OCT, and outer retinal atrophy on autofluorescence and OCT. There was good spatial correspondence between ellipsoid zone disruption and areas of diffuse hyper-autofluorescence outside the fovea. Interestingly, the ellipsoid zone disruption recovered in 4 out of 7 patients upon intensified therapeutic immunosuppression.

Conclusions. Most patients only developed peripapillary atrophy and occasional perivascular hypo-autofluorescence. A multimodal imaging approach with autofluorescence imaging and OCT may help to detect ellipsoid zone disruption in the central retina of patients with birdshot disease. Our results suggest that ellipsoid zone disruption may be related to both the activity and duration of retinal vasculitis, and could help to determine therapeutic success in birdshot disease.

Chapter 2

Introduction

Birdshot chorioretinopathy is a chronic bilateral posterior uveitis responsible for 1- 2% of all uveitis cases.[142-145] Patients are typically middle-aged and complain of blurred vision, floaters, photopsias, and nyctalopia. The ophthalmic examination shows no or low-grade anterior segment inflammation, low-grade vitritis, and at least 3 hypopigmented choroidal "birdshot" –lesions. The Human Leukocyte Antigen A*29:02 (HLA-A29:02) is present in 98% of patients and only 7% of the general population and is therefore strongly supportive of the diagnosis.[146-148] T-cell mediated inflammation may play a role in the pathogenesis of birdshot disease, but the exact mechanism of disease remains elusive.[149]

Many imaging modalities, such as color fundus photography, fluorescein angiography (FA), indocyanine green angiography (ICGA), spectral-domain optical coherence tomography (OCT), and fundus autofluorescence imaging have been used for the diagnosis and follow-up of birdshot disease.[150, 151] While FA is an accepted method to evaluate the presence of active retinal vasculitis, it remains an invasive procedure with small but inherent risks. On the other hand, the potential of other imaging techniques to determine activity and progression of birdshot disease has not yet been sufficiently explored.

OCT is an established imaging technique to document changes of retinal structure, thickness and subretinal fluid accumulation in most retinal diseases. OCT has been able to determine accelerated choroidal thinning in birdshot disease even in the absence of clinical activity.[152] Extramacular OCT scans showed extensive disruptions of the photoreceptor inner-outer segment junction/ inner segment ellipsoid zone in birdshot disease.[153] Autofluorescence imaging, on the other hand, can be of great value by mapping the vitality of the retinal pigment epithelium.[49] In addition, it may be used to measure visual pigment as an indicator of photoreceptor integrity.[154] A recent study in patients with birdshot disease showed that hypo-autofluorescence at the macula correlates with loss of visual acuity.[155] In addition, the authors frequently observed areas of hyper-autofluorescence in the periphery and posterior pole.[155] In other forms of posterior uveitis like multifocal choroiditis and punctate inner choroiditis, hyper-autofluorescence was correlated with reduced integrity of the outer retina and with irregularity in the retinal pigment epithelium on OCT.[156]

There is lack of longitudinal imaging data that could serve as biomarkers for activity and progression of birdshot disease. In this study, we use autofluorescence imaging and OCT to study the longitudinal course of outer retinal deterioration relation to the activity of birdshot disease.

Methods

Population

We retrospective studied the eyes of consecutive patients under treatment for birdshot disease at the clinical practice of the Radboud University Medical Center, Nijmegen, the Netherlands, between January 2007 and July 2015. This cohort study adhered to the tenets of the Declaration of Helsinki and was prospectively approved by the local institutional review board (*Commissie Mensgebonden Onderzoek Radboudumc*). All patients gave informed consent prior to inclusion of their data into our study. We limited inclusion to patients who were HLA-A29 positive and with a bilateral presence of ≥3 peripapillary typical birdshot lesions, low-grade anterior segment inflammation (<1+ cells) and low-grade vitreous inflammation (≤2+ vitreous haze) based on Standardization of Uveitis Nomenclature (SUN) criteria. In order to assess the presence and progression of outer retinal alterations, follow-up imaging data on OCT and/ or fundus autofluorescence had to be available. However, we did not require follow-up of both OCT and autofluorescence imaging to avoid introducing bias by excluding patients with less severe birdshot disease, for whom the acquisition of these images was rarely warranted. Naturally, the presence of adequate information on visual acuity, disease activity and therapeutic interventions during the follow-up period was mandatory.

Data collection

We identified patients suitable for study inclusion by chart review. We collected patient demographics, including age, gender, age at onset, disease duration, and visual acuity. We defined the age at onset as the age at onset of symptoms, including vibrating vision, shimmering vision, photopsias, or newly appeared floaters interfering with vision. The duration of the illness was defined as the time between and the age at onset and the final autofluorescence and OCT image, and the follow-up period was defined as the time between the first and last autofluorescence or OCT imaging session. We collected data on the (best-corrected Snellen) visual acuity and on therapeutic interventions as well as the treatment outcome by the clinical disease activity and the course of visual acuity. We analyzed the inflammatory course of birdshot disease during the follow-up period separately for the retina and choroid. We defined retinal inflammatory activity as retinal vasculitis on FA and a subsequent decision to intensify treatment. We assessed the activity of retinal vasculitis during follow-up based on periods of active vasculitis. We define a period starting from one FA showing renewed activity to the first next FA showing inactivity. We evaluated ICGA for inflammatory involvement of the choroid, by the presence of choroiditis or choroidal ischemia. Indicators for treatment success were reductions in vasculitis, diffuse leakage in the posterior pole and along the vascular arches, and cystoid macular edema (CME) on FA and/or OCT. FA/ICGA, autofluorescence and OCT imaging were performed with a Heidelberg

Spectralis HRA+OCT (Heidelberg Engineering, Heidelberg, Germany). Only fovea-centred images were used for further analysis due to lack of peripheral OCT imaging.

Image Analysis

We analyzed the disruption of the ellipsoid zone on OCT in relation to autofluorescence abnormalities (Fig 12). OCT B-scans and corresponding *en face* infrared reflectance images were displayed in the Spectralis Eye Explorer software at their original digital resolution. An intact-appearing ellipsoid zone was demarcated on each B-scan, leading to the two-dimensional mapping of those locations in the corresponding infrared image by the Spectralis software. Screenshots of the infrared/ OCT images were saved as tagged image file format (TIFF) and were imported in ImageJ (version 1.47v; http://imagej.nih.gov/ij/; provided in the public domain by the National Institutes of Health, Bethesda, MD, USA). Using the region-of-interest function of ImageJ, a two-dimensional outline of an intact-appearing ellipsoid zone was created based on the demarcation points on the infrared images of 768 x 768 pixels. This region-of-interest was used as an overlay on the autofluorescence image registered to the infrared image. We aligned the infrared and autofluorescence images using a semi-automatic registration tool, developed in MeVisLab (version 2,5a, MeVis Medical Solutions AG, Bremen, Germany), to translate, rotate and rescale the target image to accurately match three user-specified landmark locations on both the source (infrared) and target (autofluorescence) images.[157] The region-of-interest was then co-registered with the infrared image and was overlaid on the autofluorescence image.

Chapter 2

Results

Patient demographics are depicted in Table 3. We examined 42 eyes of 21 patients with birdshot disease. 15 other patients were excluded due to lack of longitudinal OCT and/or autofluorescence imaging data. All included patients were Caucasian and HLA-A29 positive. 43% of the patients were female, and the mean age at presentation was 51 (range, 25-76) years. The mean, median and mode of the disease duration were 97, 73 and 38 (range, 6-366) months, respectively, and the mean follow-up period of OCT and autofluorescence imaging was 43 (range, 3-85) months

Five lesion types were commonly observed in these patients.

Lesion type 1 - peripapillary atrophy, was present in 90% of the patients (Table 4). It generally expanded slowly if any over time (Fig 13B). This lesion's correspondence to papillitis and papillary edema is evident, considering that these inflammatory signs were present in nearly all of a given patient's FAs, except for a few patients in whom these signs were only seen at clinical presentation.

Lesion type 2 - perivascular streaks of hypo-autofluorescence corresponding to profound perivascular sheathing on FA, were an occasional observation in patients with a relatively short disease duration of 33 to 38 months (14% of study patients, Table 4). OCT did not reveal thinning or irregularity of the subjacent retinal pigment epithelium and photo- receptors; these streaks are therefore most likely the result of light absorption by blood components such as hemoglobin.
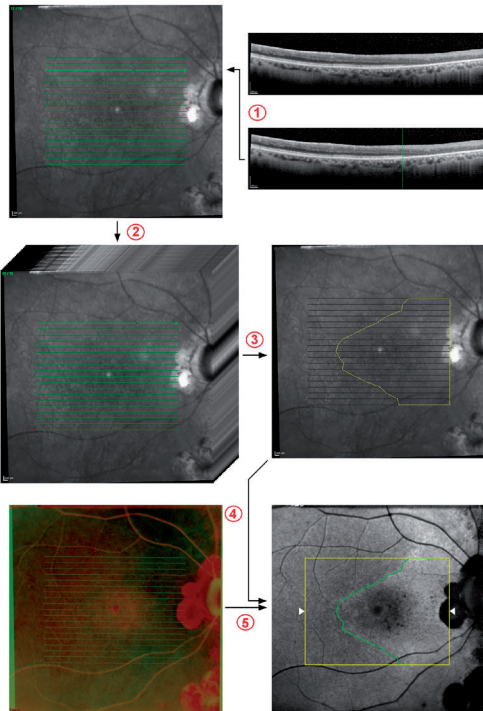

Fig 12. Analysis of the correspondence of fundus autofluorescence and disruption of the ellipsoid zone on optical coherence tomography. The boundary between an intact and disrupted ellipsoid zone was demarcated on each OCT B-scan. The OCT software mapped that location in the corresponding infrared reflectance image, of which a screenshot was made (Step 1). Step 1 was repeated for all B-scans to generate an image stack to serve as input for ImageJ (Step 2). All indicated locations were sequentially added to create a 2-dimensional outline as a region of interest (yellow line) (Step 3). The infrared image (inverted grayscale image with green look-up table) was transformed to match the autofluorescence image (inverted grayscale image with red look-up table) until the vessels aligned as indicated in yellow (Step 4). The transformation of the infrared image was applied to the region-of-interest (green line), which was overlaid on the autofluorescence image (Step 5).

Lesion type 3 - well-demarcated circular patches of chorioretinal atrophy with profound hypo-autofluorescence and hypofluorescence on late-phase ICGA were observed in 5 patients (24%, Table 4), all 5 of long disease duration. In one patient—without signs of such lesions on autofluorescence at baseline—these lesions appeared to develop out of areas of diffuse and subtle hypo-autofluorescence (Fig 14). In this patient, we found that 2 creamy-white 'birdshot' spots in color fundus images corresponded to diffuse hypo-autofluorescence spots that progressed to circular chorioretinal atrophy. Of note, we observed more diffuse hypo-autofluorescence spots than creamy-white birdshot spots. Type 3 lesions were located primarily along large retinal blood vessels and occasionally at the posterior pole (Fig 13A). Two other patients with circular atrophic lesions in the initial images did show similar diffuse hypo-autofluorescence areas, although none of these areas progressed to chorioretinal atrophy. Over time, chorioretinal atrophic lesions expanded slowly but consistently in all 5 patients (Fig 13B).

Table 3. Patient demographics

Patient	Gender	Age of onset* (years)	Follow-up† (months)	Initial BCVA‡ (OD : OS)	Final BCVA‡ (OD : OS)	Signs of choroiditis§
1	M	48	26	20/20 : 20/20	20/32 : 20/20	-
2	M	38	26	20/80 : 20/20	20/63 : 20/20	-
3	F	53	80	20/25 : 20/25	20/20 : 20/63	mild
4	F	54	64	20/32 : 20/25	20/32 : 20/32	-
5	M	57	22	20/20 : 20/32	20/20 : 20/25	-
6	F	58	58	20/32 : 20/20	20/50 : 20/32	yes
7	M	64	44	20/20 : 20/20	20/20 : 20/25	yes
8	M	72	20	20/20 : 20/25	20/20 : 20/32	-
9	F	72	44	20/40 : 20/63	20/40 : 20/80	-
10	F	25	5	20/20 : 20/20	20/20 : 20/20	-
11	M	48	36	20/40 : 20/20	20/20 : 20/20	yes
12	M	57	22	20/40 : 20/63	20/20 : 20/63	yes
13	F	54	57	20/63 : 20/50	20/50 : 20/63	yes
14	M	33	3	20/25 : 20/20	20/20 : 20/20	yes
15	F	51	81	20/20 : 20/20	20/20 : 20/20	no
16	M	54	45	20/40 : 20/32	20/25 : 20/20	yes
17	M	45	13	20/20 : 20/20	20/20 : 20/20	yes
18	M	41	43	20/40 : 20/20	20/50 : 20/20	yes
19	F	34	85	20/100 : 20/400	20/40 : 20/400	mild
20	M	48	80	20/40 : 20/20	20/50 : 20/20	-
21	F	40	77	20/100 : 20/40	0.25/200 : 20/40	-

BCVA = best-corrected visual acuity, F = female, M = male, OD = right eye, OS = left eye. Dash = no data available.
* Defined as the age at onset of symptoms.
† Defined as the time between the initial and final images.
‡ Visual acuity at the time of the initial and final images, respectively.
§ Signs of choroiditis observed in indocyanine green angiograms, at any point during the follow-up.
  See text for details.

Lesion type 4 - disruptions in the ellipsoid zone on OCT were observed in 33% of study patients (Table 4). In 6 of these 7 patients, we found a good spatial correspondence between this lesion on OCT and areas of evident, slightly speckled, hyper-autofluorescence along the optic disk, vascular arcades, and posterior pole (Fig 15). In general, we found that these patterns of hyperautofluorescence did not change significantly with the activity of the disease, except for 1 patient (patient #14, Fig 17). One patient (patient #16) had a disrupted ellipsoid zone at the location of CME without corresponding hyper-autofluorescence. Focal disruptions of the ellipsoid zone were already observed in the baseline OCT images of 7 patients and expanded slowly over time, similar to the corresponding hyper-autofluorescence. An interesting observation regarding type 4 lesions

concerned four patients (#14, 15, 16, and 19) where the disrupted ellipsoid zone on OCT reformed after successful therapeutic immunosuppression (*e.g.* Fig 16 and Fig 17) with normal appearance of reflectivity and texture on OCT. These changes were accompanied by evident reductions in the activity of vasculitis, diffuse leakage, and cystoid macular edema on FA. However, in three other patients (patients #18, 20 and 21) with a disrupted ellipsoid zone, no restoration was observed after treatment. In these patients, we observed a persistent, low-grade activity of vasculitis defined by fluorescein leakage in the area with ellipsoid zone disruption. In the initial autofluorescence and OCT images of these three patients, we found no features that were clearly distinct from those of the four patients that showed a better anatomic response to treatment. However, patients with successful treatment had a substantially shorter disease duration than these three patients.

Table 4. Frequency of outer retinal lesions and vasculitis activity in birdshot chorioretinopathy

Patient	Age[a] (years)	Disease duration[b] (months)	Lesions in final image[c] 1	2	3	4	5	Retinal vasculitis[d]	Periods of retinal vasculitis[e]
1	51	36							0
2	41	38	X						1
3	63	115	X					•16	5
4	60	73	X						2
5	60	28	X						1
6	65	82	X						1
7	69	55	X						4
8	78	78	X						0
9	79	94	X						1
10	28	38		X					1
11	51	37	X	X					2
12	59	33	X	X					2
13	68	171	X		X			•72	1
14	34	6	X			X			1
15	60	99	X			X			5
16	58	47	X			X			2
17	47	19	X				X		1
18	61	241	X		X	X		•142	2
19	47	157	X		X	X	X	•64	2
20	66	218	X		X	X	X	•119	3
21	70	366	X		X	X	X	•267	-

Dash = no data available; patient was allergic to fluorescein.

[a] Age at time of final image.

[b] Defined as the time between the last image and the age of onset.

[c] Lesions present in macular images of 55° retinal eccentricity. 1 = peripapillary atrophy; 2 = perivascular hypofluorescence; 3 = circular chorioretinal lesions; 4 = disruption of the ellipsoid zone; 5 = outer retinal atrophy.

[d] Time scheme depicting periods of active retinal vasculitis during the follow-up period of 8 years (grey bars, left to right). The exact times of fluorescein angiography are shown (stripes), with either active retinal vasculitis (red) or inactive vasculitis (blue). Brackets indicate periods of active disease. The periods during which type 4 lesions were observed are also indicated (pink bars instead of grey). Sawtooth symbols to the left indicate that the full disease duration is not shown due to lack of corresponding autofluorescence and OCT imaging data, with the omitted time indicated (months). See text for details.

[e] Periods of active retinal vasculitis. See text for details.
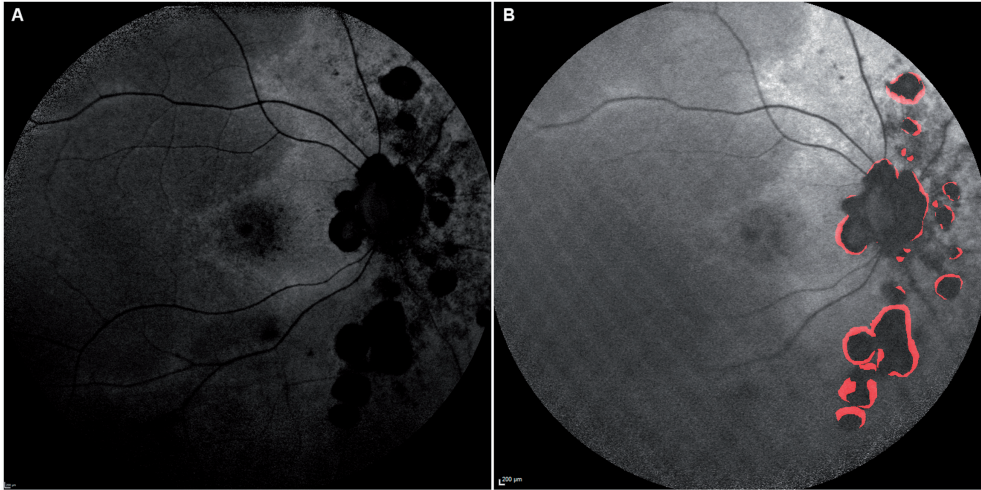
Fig 13. Location and progression of circular chorioretinal atrophy in birdshot disease (patient #20, right eye). Autofluorescence image at follow-up showing lesions along blood vessels inferior, superior, and nasal to the optic disk, as well as in the circumpapillary region (A). Baseline autofluorescence image with outline of atrophy progression area (time between images is 34 months). The outline was created by manually delineating areas of profound hypo-autofluorescence in the baseline and follow-up images, and by indicating the difference in red (B).
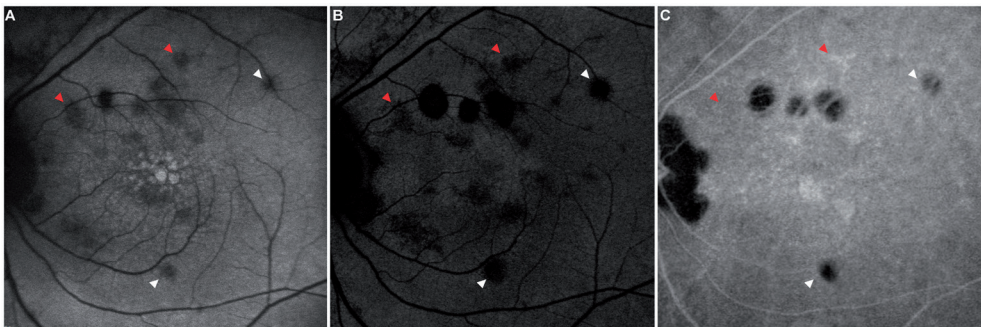
Fig 14. Development of chorioretinal lesions out of diffuse hypo–autofluorescent areas in birdshot disease (patient #19, left eye).

Some areas of diffuse hypo-autofluorescence developed into circular, well-demarcated areas of hypo-autofluorescence (A, B, white arrowheads) with corresponding hypofluorescence on late-phase ICGA (C). Some other diffuse hypo-autofluorescent areas remained stable (A, B, red arrowheads). Note that most of these stable areas appear to correspond with hyperfluorescence on late-phase ICGA Time between the initial (A) and final (B, C) images was 66 months. The bright white macular foci in (A) correspond with cystoid macular edema on fluorescein angiography.

Lesion type 5 - outer retinal atrophy, indicated by atrophic photoreceptors and retinal pigment epithelium on OCT and/or the typical profound fundus hypo- autofluorescence, was observed in 19% of study patients (Table 4). In a patient with advanced birdshot disease (patient #21), the hyper-autofluorescence with correspondence to ellipsoid zone disruption on OCT mentioned earlier, was observed lining these atrophic patches and diffuse hypo- autofluorescence areas (Fig 15a).

Fovea-centred images of 57% of study patients showed a lack of outer retinal damage on OCT or autofluorescence abnormalities during the follow-up period, except for lesion types 1 or 2. These patients had a mean disease duration of 59 (range, 28-115) months. Lesion types 3, 4 and 5 were observed in the other 43% of study patients, who had a mean disease duration of 147 months (range, 6-366 months). The activity of retinal vasculitis in the former 12 patients appeared highly comparable to that in the other 43% of study patients (Table 4). The ICGA generally showed signs of choroidal inflammatory involvement like scattered hypofluorescent spots, small hyperfluorescent plaques and diffuse choroidal leakage in both groups of patients (Table 3). Autofluorescence imaging showed bright spots in the fovea (Fig 14a) in 7 patients. These spots corresponded well with CME visible on FA and SD-OCT. On SD-OCT, the corresponding ellipsoid zone appeared slightly darker in most cases, probably due to shadow artifacts. It was not evidently disrupted. These hyperautofluorescent spots subsided when the CME resolved.

Discussion

We have studied the longitudinal changes in the outer retina of patients with birdshot disease using OCT and fundus autofluorescence imaging. Outer retinal atrophy, if present, progressed slowly over time. Changes in the photoreceptor layer appeared to be common and widespread. A disrupted ellipsoid zone on OCT corresponded well with areas of geographic, diffuse hyper-autofluorescence compared to the surrounding area. In 4 of 7 patients with a disrupted ellipsoid zone, we observed its recovery concurrent with successful immunosuppressive treatment represented by substantial reductions in vasculitis, cystoid macular edema and diffuse leakage.

As birdshot disease progresses, focal lesions of retinochoroidal atrophy become apparent in the peripheral retina; in addition, the patient's overall vision may deteriorate.[158] An earlier study showed that patients with birdshot disease often have extensive disruptions of the photoreceptor layer in the periphery by extramacular OCT scans.[153] Since a multimodal imaging approach may be more sensitive to detect subtle retinal alterations,[157] we examined the central retina for the development and progression of retinal deterioration over the course of several years by combining imaging modalities like autofluorescence imaging and OCT. We found that photoreceptor abnormalities were a common observation, as compared to the rarely observed *de novo* development of chorioretinal atrophy (Fig 14) and the slow
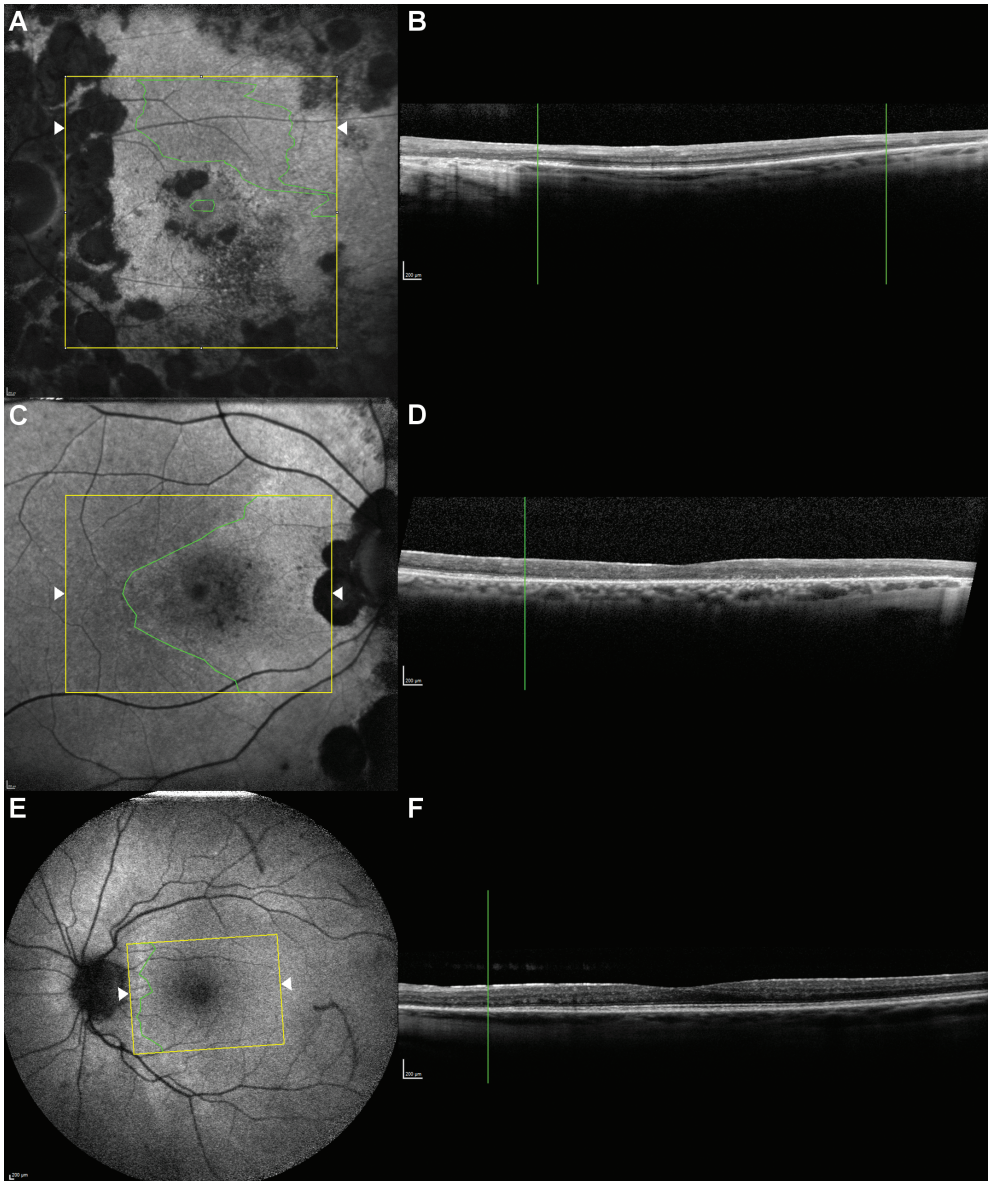
Fig 15. Correspondence between disruption of the ellipsoid zone on SD–OCT and hyperfluorescence in three patients with birdshot disease. Patient #21 (A, B), patient #20 (C, D), and patient #15 (E, F). An intact-appearing ellipsoid zone is demarcated in each SD-OCT B-scan (B, D, F), and the result is overlaid on the autofluorescence image to determine the region with an intact ellipsoid zone. The latter is demarcated by the green line (A, C, E). The SD-OCT scan area is indicated in yellow. White arrowheads indicate the locations of the shown B-scans. Hyper-autofluorescence can be observed lining the atrophic patches and hypo-autofluorescent areas surrounding, and central in, the posterior pole (A). Note the foveal sparing in patient #21 (A).

expansion, if any, of existing atrophy (Fig 13 and Table 4, lesion type 4). Relative to other types of outer retinal lesions in birdshot disease, photoreceptor damage—as represented by disruption of the ellipsoid zone—therefore appears to be a frequent manifestation of outer retinal damage in response to inflammation. This damage is probably not strictly related to disease activity, because it was absent in the central retina of several other patients with high vasculitis activity (Table 4). The duration of inflammation may be a factor as well, considering that most of our patients with ellipsoid zone disruptions had a relatively long disease duration (Table 4).

Fundus autofluorescence imaging can also be helpful in the evaluation of patients with birdshot disease. First, the distribution of pigment epithelial atrophy that can be difficult to discern on funduscopy, can be mapped.[159] Second, areas of discrete hyper-autofluorescence may help to detect and follow regions of outer retinal damage that may be restorable by effective treatment. Although hyper-autofluorescence areas were previously described in patients with birdshot disease, its clinical relevance was unclear due to a lack of correlation with intraocular inflammation, macular edema and visual acuity,[155] which is similar to our findings. In our study, we found a remarkable correspondence between subtle hyper-autofluorescence and the potentially reversible photoreceptor damage as shown by disruption of the ellipsoid zone on OCT (Fig 15). As to the explanation for the subtle hyper-autofluorescence: reduced visual pigment optical density in photoreceptor outer segments can result in an increased autofluorescence intensity.[154] A disrupted ellipsoid zone is not synonymous with loss of the photoreceptors. A recent study employing adaptive optics showed the presence of substantial populations of photoreceptors in areas of disrupted ellipsoid zone on OCT.[85] Therefore, areas of subtle autofluorescence increase and ellipsoid zone disruption probably reflect shortening of photoreceptor outer segments and not photoreceptor loss. This is indirectly corroborated by the striking restoration of the ellipsoid zone architecture in several patients with birdshot disease following successful anti-inflammatory treatment. Although ellipsoid zone disruptions were observed only in 7 patients and improved in only 4, evidence suggests that they are more common in extramacular OCT scans,[153] As was found earlier in a case,[160] anatomic improvements in this band could be detected in several patients with reduced, albeit still present, inflammatory signs (Figs. 16 and 17). In retinitis pigmentosa, the loss of this band has been shown to coincide with loss of visual field, and its assessment has been suggested as an end point for clinical trials for cone dystrophies, achromatopsia and retinitis pigmentosa.[161] Therefore, we are of the opinion that monitoring this disruption could provide indications of clinically relevant anatomical outcomes of immunosuppressive treatments, in addition to angiographic evidence of immunosuppression. Although both ellipsoid zone disruptions and geographic hyperautofluorescence were most commonly observed adjacent to the optic disk and the vascular arcades, one may consider imaging the whole posterior pole by OCT and autofluorescence in order to obtain a complete picture of areas of mild to moderate photoreceptor damage in patients with birdshot disease.
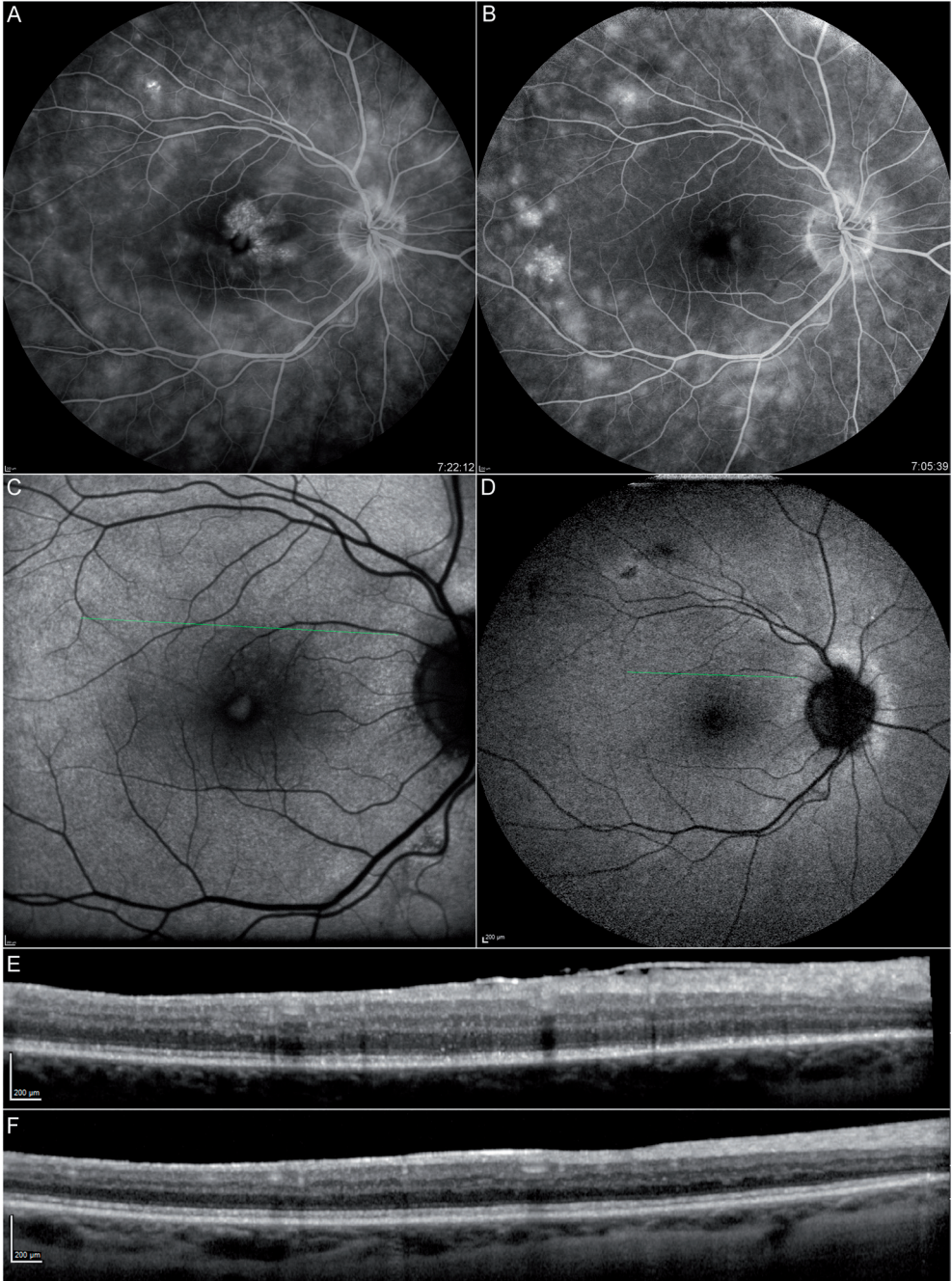
← 16. Restoration of the ellipsoid zone in a patient with birdshot disease (patient #15, right eye).
Late-phase fluorescein angiography showed CME and diffuse leakage along the large retinal vessels in the initial image (A). After immunosuppressive treatment, CME is absent and diffuse leakage in the posterior pole is less (B). Autofluorescence images show slight circumpapillary hyper-autofluorescence that persists (C, D). However, corresponding SD-OCT scans show that the disrupted ellipsoid zone in the circumpapillary region (E) has mostly recovered (F). The locations of the SD-OCT scans are indicated by the green lines in (C) and (D). Time between the initial (A, C, E) and final (B, D, F) images was approximately 7 years.

→ Fig 17. Restoration of the ellipsoid zone in a patient with birdshot disease with a short disease duration of 5 months (patient #14, left eye). Late-phase fluorescein angiography showed significant vasculitis (A) that reduced (B) upon immunosuppressive treatment. Fundus autofluorescence shows a macular hyper- autofluorescent plaque (C) that disappeared (D). Corresponding SD-OCT scans show that the disrupted ellipsoid zone in the macula (E) has recovered (F). The locations of the SD-OCT scans are indicated by the green lines in (C) and (D). Time between the initial (A, C, E) and final (B, D, F) images was 35 days.
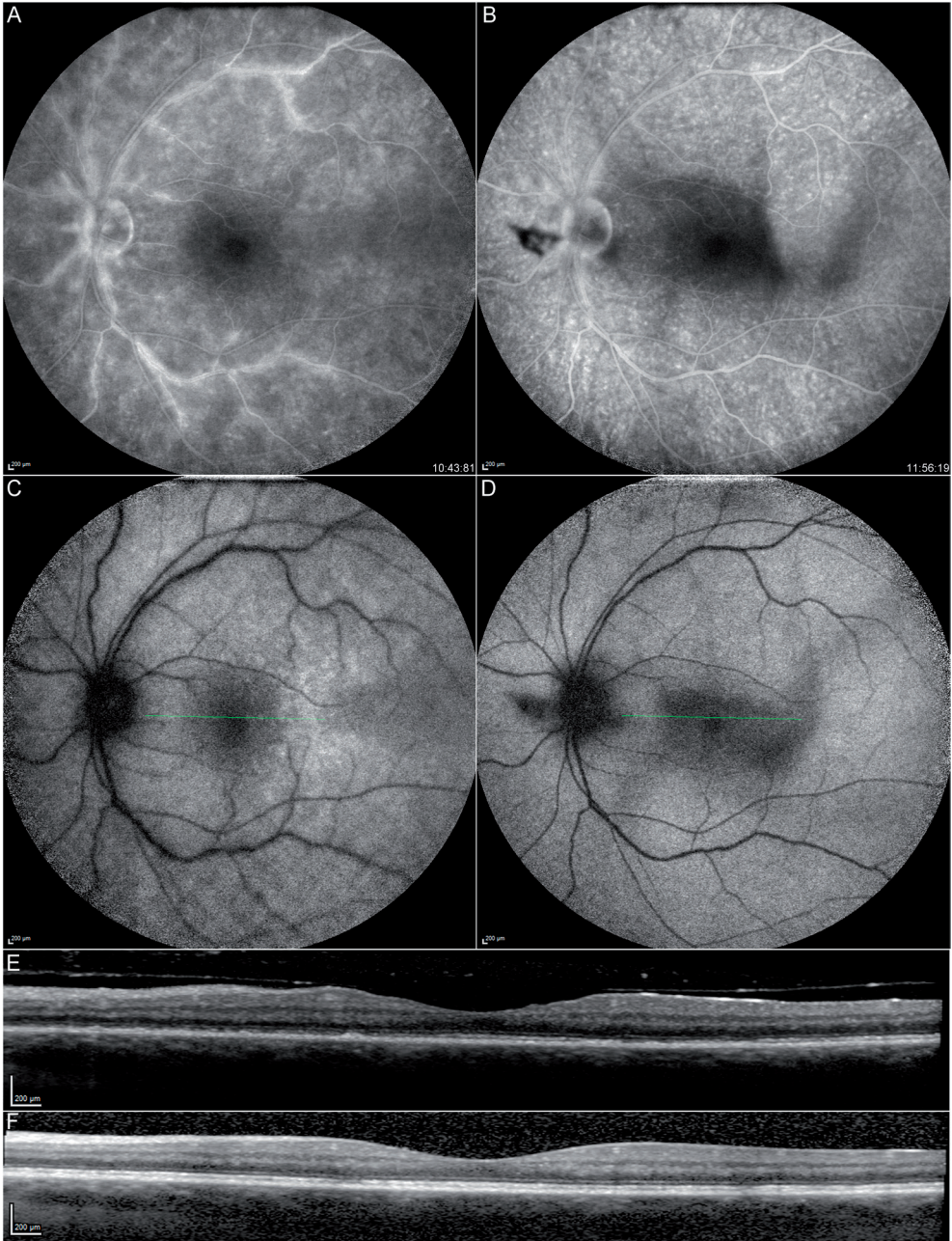
In our study of birdshot disease, it appears that the most profound autofluorescence changes—including RPE-atrophy and ellipsoid zone disruption—can also be detected with OCT, while OCT also provides depth localization of the affected tissues. However, while a snapshot autofluorescence image provides high-resolution information indicating the integrity of the RPE in a relatively large field of view, acquiring this information with OCT requires the time-consuming acquisition of multiple dense volumes. Piffer *et al.* (2014)[155] found diffuse hyper- or hypo-autofluorescence changes in the wider peripheral retina in 46.7% of the patients. They concluded that peripheral lesions detected by autofluorescence indicate how diffusely the periphery is affected, and that this accounts for the visual discomfort that patients describe (loss of peripheral vision, hemeralopia, *etc.*).[155] Considering these facts, we are of the opinion that autofluorescence imaging could provide a time-economic means to provide a more complete picture of a patients' disease status than OCT alone.

Our study has several limitations, including the retrospective design. It would be interesting to study the causes of outer retinal changes more closely with matching ICGA data. Furthermore, we did not correlate the ellipsoid zone disruption with high-resolution imaging techniques like adaptive-optics. This would have been helpful to distinguish between impaired photoreceptors and loss of rods and cones. Due to the qualitative descriptive design of our study, we have not used validated segmentation software to measure the thicknesses of outer retinal bands on OCT. These techniques might give us more information on the actual photoreceptor damage, and the potential for recovery, as well as risk and rate of progression of outer retinal atrophy.

In conclusion, multimodal imaging with autofluorescence imaging and OCT can detect subclinical outer retinal damage in patients with birdshot disease. Our data suggest that ellipsoid zone disruption, indicative of photoreceptor damage, is a relatively frequent aspect of central retinal deterioration in birdshot disease, and that may help to monitor therapeutic success in this enigmatic disease.

Chapter 2.3

Photo–oxidative stress during fundus autofluorescence imaging

Michel M. Teussink
Stanley Lambertus
Frits F. de Mul
Malgorzata B. Rozanowska
Carel B. Hoyng
B. Jeroen Klevering
Thomas Theelen

Abstract

Background. Current standards and guidelines aimed at preventing retinal phototoxicity do not specifically evaluate the contribution of endogenous photosensitizers. However, patients with certain retinal diseases do exhibit abnormal levels of potential photosensitizers such as lipofuscin bisretinoids in the retinal pigment epithelium (RPE). We explored if such contributions can be determined by a numerical assessment of in-vivo photo-oxidative stress subsequent to irradiation of endogenous RPE-lipofuscin.

Methods. We calculated the retinal exposure levels, optical filtering of incident radiation by the ocular lens, media, and RPE-melanin, light absorption by lipofuscin, and photochemical effects at the level of the retinal pigment epithelium (RPE) in two clinically relevant settings: exposure to short-wavelength (λ = 488 nm) fundus autofluorescence (AF) excitation light and exposure to indirect (diffuse) sunlight. We extracted the relevant parameters from the literature or estimated their value if empirical data were not available.

Results. In healthy persons at age 20, 40, and 60, respectively, the rate of oxygen photoconsumption by lipofuscin increases by 1.3, 1.7, and 2.4 fold during AF-imaging as compared to diffuse sunlight. In patients with STGD1 below the age of 30, this rate was 3.3-fold higher as compared to age-matched controls during either sunlight or fundus AF imaging.

Conclusions. Our results suggest that the RPE of patients with STGD1 is generally at increased risk of photo-oxidative stress, while exposure during AF-imaging amplifies this risk. These theoretical results have not yet been verified with in-vivo measurements due to a lack of sufficiently sensitive in-vivo measurement techniques.

1. Introduction

Fundus autofluorescence (AF) imaging visualizes the accumulation of fluorophores that constitute a substantial fraction of RPE lipofuscin in the retinal pigment epithelium (RPE).[53] Lipofuscin forms as a by-product of the visual cycle in photoreceptor outer segment disks, which are subsequently phagocytosed by RPE cells. As a result, lipofuscin accumulates in the lysosomes of RPE cells,[162-165] and continues to accumulate with age.[166] Short-wavelength (488 nm) AF is commonly regarded as a way to monitor the status of RPE cells, with areas of high AF indicating increased lipofuscin levels and areas of absent AF indicating loss of RPE cells. The interpretation of AF abnormalities is probably more complex than this,[49] but we anticipate that a more thorough understanding of AF patterns will give deeper insight into retinal disease progression, which can eventually help to evaluate the efficacy of therapies.[48]

The retinal radiant exposure of the bright AF excitation light is far below ANSI safety thresholds.[167] These thresholds were based on cross-sectional data of the effects of light on a cellular level, designed to protect the eye and skin from accidental light exposure. To reduce ocular exposures, the International Commission of Non-Ionizing Radiation Protection (ICNIRP) has also provided guidelines for ophthalmic instruments.[168] Commercial or experimental ophthalmic instruments adhere to these standards with additional constraints for intentional exposures,[169] and may thus be considered safe with regard to short-term effects.

However, patients with certain retinal diseases may be highly susceptible to photic toxicity.[114, 170] This has led to concerns that patients with recessive Stargardt disease (STGD1) may be at risk for light toxicity during short-wavelength AF imaging.[171] Indeed, the ANSI thresholds and ICNIRP guidelines do not specifically evaluate the contribution of endogenous photosensitizers in enhancing a patient's susceptibility to retinal phototoxicity. In patients with STGD1, photochemical damage may involve changes in molecules within the visual cycle such as all-*trans*-retinal.[114, 126] Additionally, removal of all-*trans*-retinol from the photoreceptor outer segment disks is impaired,[25] which leads to an accelerated accumulation of lipofuscin bisretinoids in the RPE. Some of these bisretinoids have been identified as potent photosensitizers in animal studies. In *Abca4*$^{-/-}$ mice, very high intensities (50 mW/cm^2) of blue light (λ = 430±20 nm) irradiation for 30 min caused severe atrophy of photoreceptors and RPE cells with elevated lipofuscin, which was less pronounced in age-matched wild type controls.[125] Conversely, there was no photoreceptor atrophy in *Rpe65*^{rd12} mice without RPE-lipofuscin.[125] Whether the mechanism of photochemical damage involves changes in either lipofuscin or molecules within the visual cycle such as all-*trans*-retinal, patients with STGD1 will be highly susceptible to photic injury.[114, 126] Consistent with this notion, even chronic exposure to normal daylight appears to increase the progression of RPE damage in STGD1.[172]

There is lack of empirical evidence about the extent to which endogenous photosensitizers make humans more susceptible to photic injury. Extrapolation from results from animal studies to humans is difficult because of their considerable differences in light susceptibility. Therefore, we numerically simulated in-vivo photo-oxidative stress in the human RPE subsequent to irradiation of endogenous RPE-lipofuscin. More precisely, we simulated exposure during either AF imaging or diffuse sunlight in either healthy individuals of different ages or patients with Stargardt disease. Daylight exposure is not known to cause retinal injury to healthy people except for unintentional and excessive exposures,[173] which thus can provide a reference frame of normally harmless effects. Such an approach may yield considerable insight, because it facilitates the identification of gaps in our knowledge of all aspects involved in retinal photo-oxidative stress.

2. Methods

2.1 Retinal exposures

2.1.1 Exposure to daylight

We used the solar spectrum of the American Society of Testing and Materials (ASTM G173-03) as a reference for terrestrial solar irradiation.[174] It was measured under atmospheric conditions considered a reasonable average over a period of one year, and pointing to the sun at an inclination of 37°. This inclination corresponds to the approximate average latitude of the 48 contiguous states of the USA. This spectrum includes light scattered by the atmosphere and light reflected off the earth's surface (Fig 18). In such a scenario of free or Newtonian illumination,[175] a distant light source—the sun—irradiates an area A larger than the pupil of the eye. The retinal radiant exposure H_r (J·cm-2) can then be expressed as a function of corneal radiant exposure H_r (J·cm^{-2}):[169]

$$H_r = H_c \frac{A_{pupil}}{A_{retina}} \approx H_c \tau \frac{d_p^2}{f_e^2 \alpha^2} = L_s \tau \frac{\pi}{4} \left(\frac{d_p}{f_e} \right)^2 , \qquad (1)$$

with the pupil diameter (d_p), the eye's focal length (f_e), the visual angle of the source (α), and the ocular media transmission (τ). For free illumination, the retinal radiant exposure H_r can also be expressed as a function of the irradiance of the source $(L_s$, unit J·sr$^{-1})$, independent of α (Eq. [1], third term).[169] Using normative data of the pupil diameter at different ages measured under various lighting conditions,[176] we calculated an average pupil diameter d_p at age 20, 40, and 60 of 3.8, 3.5, and 3.2 mm, respectively (Appendix, section 1). We assumed that the pupil is adapted to daylight luminance without pharmacological dilation and we used an average focal length f_e of the eye of 17 mm.

Because a person will usually not stare directly into the sun, the referenced solar spectrum is an overestimation of the actual solar irradiation entering the eye. We therefore subtracted the 'direct and circumsolar' spectrum that measures a 2.5° circle around the solar disk from the aforementioned ('global tilt') solar spectrum as an indication of indirect solar irradiation, *i.e.,* diffuse insolation (Fig 18). To determine the irradiance L_s (W·cm^{-2}·sr^{-1}) of this diffuse scattered light, we used the solid angle Ω of radiation specified for the ASTM reference spectrum, which equals that of diffuse light scattered in a full hemisphere ($\Omega = 2\pi$ steradian).[174] Consequently, $L_s \approx H_c / 2\pi$.
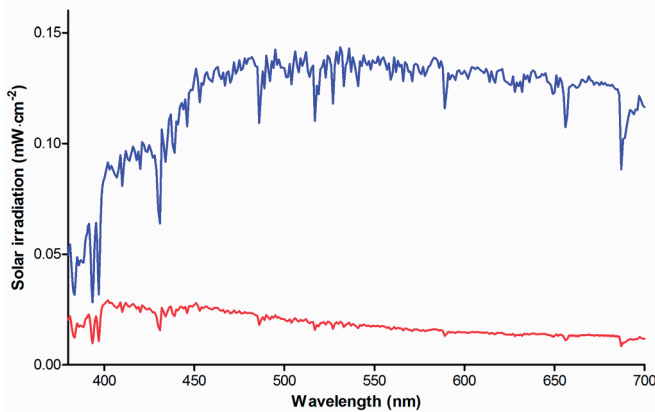
Figure 18. Visible range of the ASTM G173-03 solar irradiance spectrum, measured at a global tilt of 37° pointing to the sun (blue). The solar irradiance spectrum when not staring directly at the sun, including light scattered by the atmosphere and light reflected off the earth's surface, is also shown (red).

To account for absorption in the ocular media, we employed an algorithm that predicts the average media optical density at a given age and wavelength.[2, 177] The algorithm of Van de Kraats and Van Norren is based on six optical density components with the optical density D_λ depending only on wavelength and age.[2] We obtain:

$$H_r = \frac{H_c}{2\pi}\exp(-D_\lambda)\frac{\pi}{4}\left(\frac{d_p}{f_e}\right)^2.$$

(2)

We used Eq. (2) to predict retinal exposures to diffuse insolation at age 20, 40, and 60.

2.1.2 Autofluorescence Imaging

In autofluorescence imaging by confocal scanning-laser ophthalmoscopy (cSLO), the imaging beam enters the eye with a known angle α through an entrance pupil smaller than the pharmacologically dilated pupil. In this scenario of Maxwellian illumination, the retinal radiant exposure is the power entering the pupil φ, divided by the retinal exposed area:[169]

$$H_r = \Phi \tau \frac{4}{\pi \left(f_e \alpha \right)^2}. \tag{3}$$

The blue autofluorescence imaging mode of the widely used Spectralis™ HRA+OCT employs an optically pumped solid-state continuous wave laser with a wavelength of 488 ± 2 nm and a recommended maximum optical power of 260 μW to excite lipofuscin fluorophores in the fundus. Emitted fluorescence in the wavelength range of 500 – 680 nm is detected after passing through a barrier filter. Typical AF imaging sessions scan at the high-speed mode (768 x 768 pixels; 8.9 frames·s^{-1}) in square 30° fields. The average retinal radiant exposure in perfectly transparent media is then 328 μW·cm^{-2}. Taking media absorption in a healthy 20-year old person into account, it is 190.4 μW·cm^{-2}.

2.2 Optical screening by melanin

The flux of photons impinging on lipofuscin is reduced due to optical screening by melanin granules situated apically in RPE cells. RPE melanin consists largely of eumelanin,[178] which is able to dissipate approximately 90% of incident UV energy as heat.[179] We performed a Monte-Carlo (MC) simulation of light scattering and absorption by melanin in the RPE to investigate optical screening by melanin in healthy people of different ages and in patients with Stargardt disease. MC methods are a standard approach in numerical simulation and the basic methodology in simulating scattering of light in human tissues is, by now, strongly established. MC methods have been employed with great success in order to predict the properties of light scattering in human tissues.[180-183] Our calculation of light *scattering* by melanosomes was similar to an earlier publication on using MC methods to investigate iris melanosomes.[184] Our calculation of light *absorption* by melanin, however, was not similar: we based it on empirical data of the absorption spectrum of melanin. See Appendix, section 2 for details of this MC simulation of in-vivo optical attenuation by RPE-melanin in the paramacular RPE-cells. We modeled the paramacular RPE as a single 9 μm 185 thick sheet, and RPE-melanin could occupy the apical ≤33% of the RPE-cell (inward positive, *i.e.*, the optical path length $l_{melanin}$ ranged from 0 to +3 μm). An infinitely thin and non-divergent beam of light ('pencil beam') injected 5·10^5 photons into the system. We varied the thickness of the layer in which the scatterers (melanosomes) are present with age and/or the presence of STGD1, as specified in Appendix, section 2.

MC-simulations of optical screening by RPE-melanin were performed for specified wavelengths (λ = 380, 405, …. , 705) for each of four different scenarios: healthy 20-, 40-, and 60- year old paramacular RPE, and 20-year old non-atrophic RPE of a patient with STGD1. MontCarl counted the number of photons that were either absorbed, backscattered (upon refractive passage at the interface between two layers and directed towards negative depth values), or transmitted (the inverse of backscattering; this could therefore include non-scattered and forward scattered photons). From these fractions and the total number of incident photons, we calculated attenuation coefficients ($\mu_{a,\,melanin}$ and $\mu'_{s,\,melanin}$) and the optical density ($OD_{melanin}$) as:

$$\mu_{a,\,melanin} = -\log\left(1 - \frac{[\text{Absorbed photons}]}{[\text{Total injected photons}]}\right)\Big/ l_{melanin}, \tag{4}$$

$$\mu'_{s,\,melanin} = -\log\left(1 - \frac{[\text{Backscattered photons}]}{[\text{Total injected photons}]}\right)\Big/ l_{melanin}, \text{ and} \tag{5}$$

$$OD_{melanin} = \left(\mu_{a,\,melanin} + \mu'_{s,\,melanin}\right) \cdot l_{melanin}. \tag{6}$$

2.3 Optical absorption by lipofuscin

Studies on photosensitizers have shown a strong relationship between total light absorbed and oxygen uptake.[186, 187] The high optical density of each lipofuscin granule may give rise to significant internal optical screening.[188] Granules in the basal part of the cell may therefore receive little or no light; resulting in a poor correlation between the RPE-lipofuscin concentration and total light absorbed. This may explain why—at present—we have no evidence that lipofuscin bisretinoids photo-oxidation varies with lipofuscin bisretinoid concentration.[189]

Calibrated fundus AF measurements have shown that patients with STGD1 exhibit substantially increased fluorescence from RPE-lipofuscin.[135, 190, 191] This may be ascribed to either increased fluorescence efficiency of lipofuscin bisretinoids, increased absorption of excitation energy, or both. The 'dark' or 'silent' choroid sign on fluorescein angiography, present in 37 - 50% of patients,[192, 193] indicates a considerable reduction in light transmission (λ = 488 nm) through the RPE.[192, 194, 195] Increased backscatter and/or absorption from lipofuscin may underlie this phenomenon; however, increased backscatter is highly unlikely to be the sole cause. Finally, mouse studies have shown that the amount of the lipofuscin bisretinoid A2E decreases in-vivo when retinal light exposure increases, due to lipofuscin oxidation and subsequent degradation.[196]

We incorporated light absorption by lipofuscin into our simulation because of these indications. Although an accurate approximation of the fraction of light absorbed could be obtained with an MC simulation, as far as we know there are no empirical data on certain optical parameters of lipofuscin granules. These parameters include the granule size distribution, wavelength-dependent absorption- and scattering cross-sections, and empirical data on the angular scattering function. We therefore took a different approach, based on the principle that light absorption tends to correlate with the granule concentration n_g and the optical path length (l) through these granules. Hence, we considered their product $(n_g \cdot l)$ indicative of light absorption.

Although electron microscopy of the RPE of patients with STGD1 shows massive accumulations of lipofuscin in the posterior pole,[197] it is difficult to obtain an exact value of $(n_g \cdot l)$ based on these images. In mice, however, the concentration of a major fluorophore of lipofuscin (A2E)[106] was found to correlate with the calibrated fluorescence intensity from RPE-cells.[189] Since similar data[134] are available both in healthy people[191] and patients with STGD1,[135] estimations of $(n_g \cdot l)$ in STGD1 based on fundus AF would be an alternative. We tested the feasibility of such estimations by determining the correlation between $(n_g \cdot l)$ and fundus AF intensity (detailed in the Appendix, section 3).

2.4 Oxygen photoconsumption by lipofuscin granules

The goal of our simulation was to compute oxygen uptake by lipofuscin granules in-vivo under the considered exposure regimes, because oxygen photoconsumption by lipofuscin can serve as an indicator of lipofuscin oxidation.[198] We considered in-vitro oxygen uptake measurements on isolated human RPE lipofuscin granules by Rozanowska *et al.* (2004)[198] to be—at present—the most appropriate basis for this calculation. Firstly, their measurement setup and results were described in sufficient detail to allow for meaningful and quantitative comparisons with in-vivo exposure conditions. Second, isolated—but intact—human RPE lipofuscin granules of different ages were used, and the pH of the medium is comparable to that in-vivo. As such, these two factors are representative of physiological conditions. The results obtained in sections 3.1 to 3.3 serve as variables influencing oxygen uptake by lipofuscin, and are applicable to an in-vivo milieu. We determined the corresponding values of these variables applicable to the in-vitro measurements by Rozanowska *et al.* (2004).[198] By normalizing for differences in these variables in-vivo, we predicted the rates of oxygen uptake, were they measured in-vivo in the RPE. Details on this normalization are described in Appendix, section 4.

3. Results

3.1 Retinal exposures

The retinal exposure (mW·cm^{-2}) during daylight or typical AF imaging sessions was corrected for absorption and scattering in the lens and media (plotted in Fig 19). After integration over wavelength (λ = 380-700 nm), exposures to the AF excitation beam exceed exposures during daylight by 35, 41, and 49-fold at ages 20, 40, and 60, respectively.
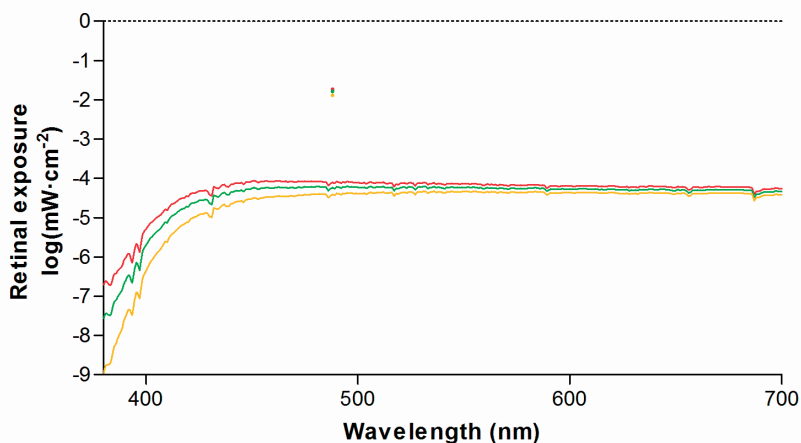
Fig 19. Retinal exposure from diffuse solar irradiation compared to excitation light of short–wavelength retinal auto–fluorescence. At λ = 488 nm the peak height is indicated by single colored dots. Exposures were calculated by Eq. (2) and Eq. (3), respectively. Exposures in ocular media of different ages are plotted; 20 year-old (red), 40 year-old (green), and 60 year-old (orange).

3.2 Optical screening by RPE–melanin in–vivo

The MC results are plotted in Fig 20. It can be seen that absorption dominates over scattering at λ <505 nm. We evaluated whether this phenomenon is caused by wavelength-dependent differences in the absorption and scattering properties of the melanosomes. By taking the product of each granule class' concentration and absorption/ scattering cross-section, and taking the arrhythmic sum of all granule classes in the medium, the theoretical absorption coefficient ($\mu_{a,\ melanin}$) and scattering coefficient ($\mu_{s,\ melanin}$) can be determined. The reduced scattering (backscattering) coefficient can be calculated by including the scattering anisotropy factor (g). It varies from -1 for complete backscattering, through 0 for isotropic scattering, to +1 for complete forward scattering, We calculated the backscattering

coefficient by $\mu'_{s, \text{melanin}} = \mu_{s, \text{melanin}} \cdot (1 - g)$. An estimate of light attenuation due to absorption ($\text{OD}_{a, \text{melanin}} = \mu_{a, \text{melanin}} \cdot l_{\text{melanin}}$) backscattering ($\text{OD}_{s, \text{melanin}} = \mu'_{s, \text{melanin}} \cdot l_{\text{melanin}}$) and the total optical density (Eq. 6) can then be made. As can be seen in Fig 20(a), scattering is expected to dominate over absorption for all wavelengths under investigation, which is in contrast to the MC simulation results. In addition, the MC results show several fold lower attenuation for both scattering and absorption.

We found that both of these phenomena can be explained by two aspects: our simulation was performed for a thin layer (3 μm) in combination with a strong tendency for forward scattering in this layer of melanosomes. In this system, photons will deviate from their path by about 30° on average ($\cos^{-1} <g> = \cos^{-1} (0.865) = 30.3°$) at each scattering event, which indicates that randomization of the direction of scattering occurs only after several scattering events. This would suggest that more backscattering occurs when the melanosome layer is thicker. We tested this suggestion by simulating a melanosome layer of either 3 μm or 52.5 μm with an average transmission of photons of 89.4% and 6.6%, respectively (Fig 20[b]). We found, in the case of the thicker sample, absorption actually dominates over scattering for all tested wavelength and an overall reduction in the backscattering coefficient $\mu'_{s, \text{melanin}}$. This suggests that, although a photon may only backscatter after a given number of scattering events, it becomes increasingly more likely that the photon will be absorbed before it reaches that point. The effect of simulating a thin sample is also illustrated in Fig 21. Thus, in our MC simulation, photons have a greater tendency for absorption as compared to backscattering at shorter wavelengths.
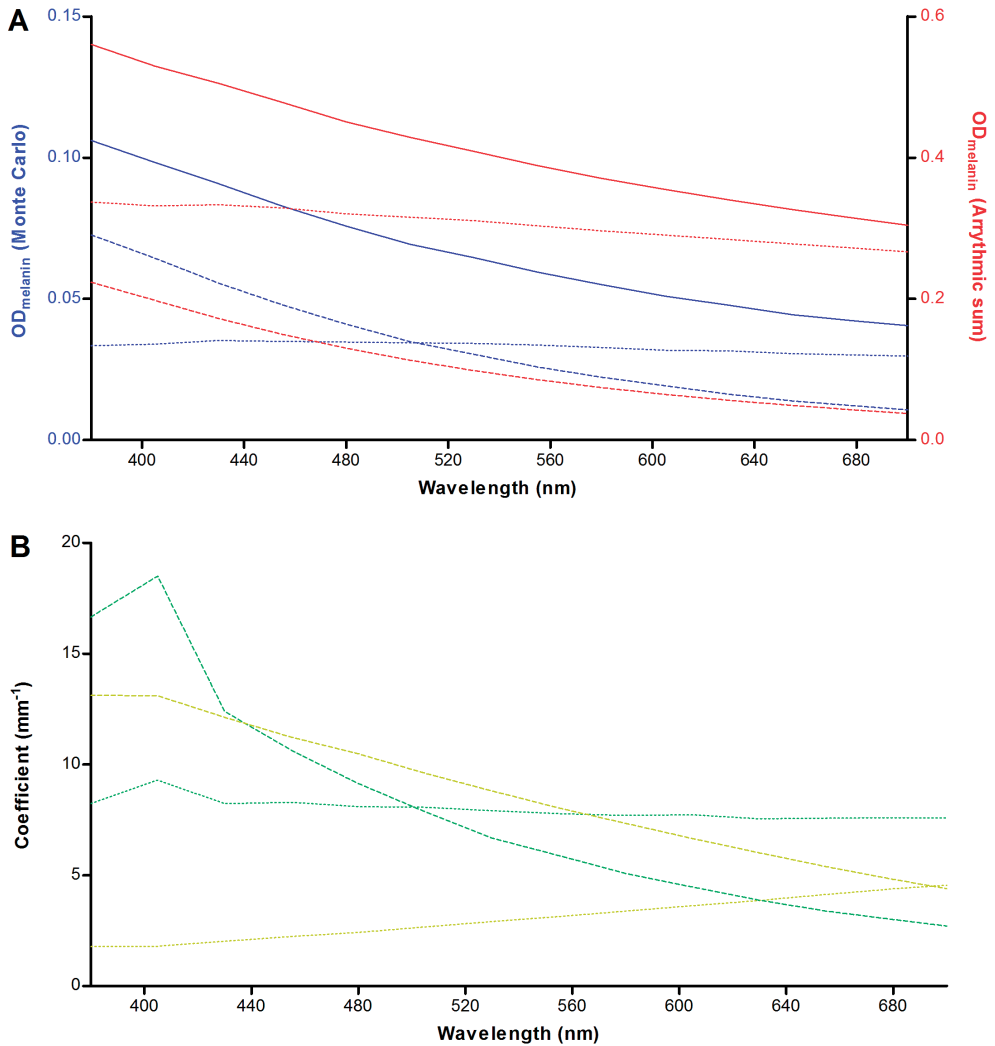
Fig 20. A) Agreement between Monte-Carlo simulation and theory, plotted based on conditions in the paramacular RPE of a healthy 20-year old person. The optical density (OD) was calculated based on the product of the attenuation coefficient and the melanosome layer thickness ($l_{melanin}$). Attenuation by absorption (striped line), scattering (dotted line), and total attenuation (straight line) are plotted separately. The MC results are shown in blue (left Y-axis) and the theoretical result is shown in red (right Y-axis). See text for details. B) Simulations of a thin (3 μm; dark green) and thick (52.5 μm; dark yellow) layer of melanosomes. In case of thicker layers, there is a dominance of the absorption coefficient ($\mu_{a, melanin}$, striped lines) over the backscattering coefficient ($\mu'_{s, melanin}$, dotted lines) for all tested wavelengths.
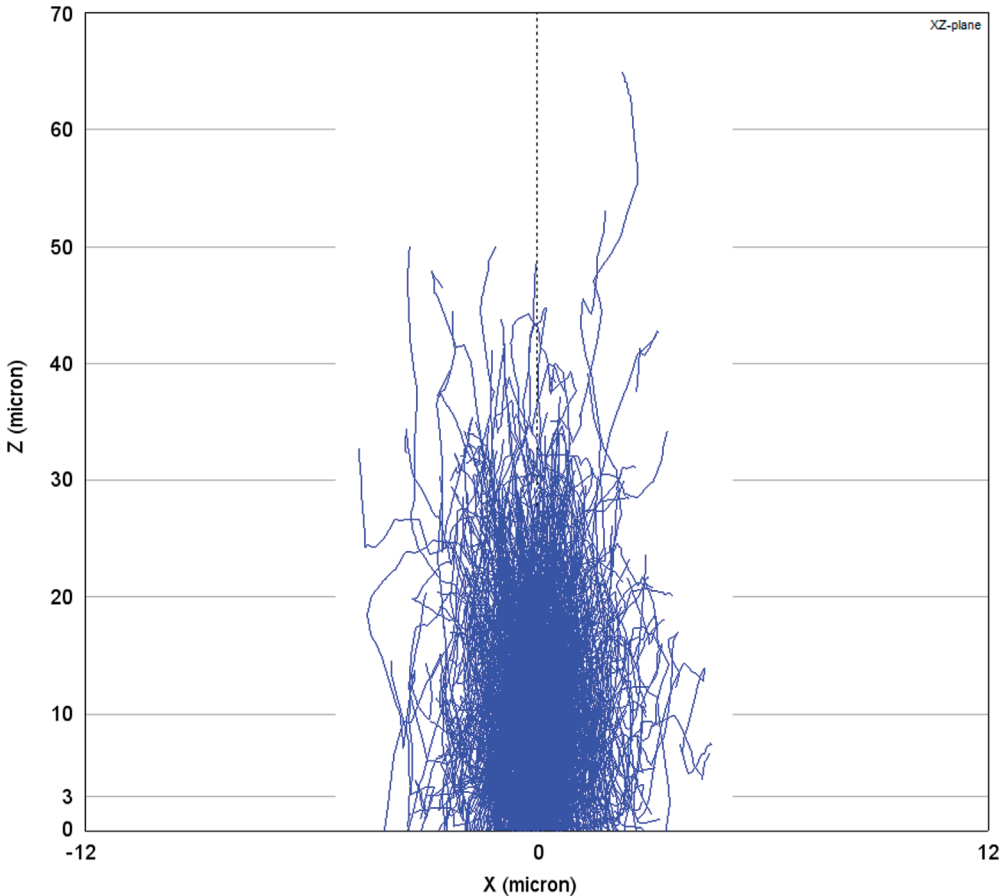
Fig 21. Monte–Carlo simulation of light scattering and absorption in a thick layer of melanosomes.
In this plot generated by MontCarl, the optical paths (blue lines) of 3000 photons are ray-traced through a relatively thick layer of RPE-melanosomes at the concentration in-vivo. Photons are injected by an infinitely thin light beam at X/ Y = 0/ 0. The X- and Z-axes, respectively, indicate the lateral and vertical (depth) location in the sample. Most photons are either absorbed or scattered back at Z = 30 μm. At the assumed maximum in-vivo layer 'thickness' of RPE-melanosomes (3 μm), a small proportion of photons are backscattered or absorbed.

The MC results for the various scenarios tested are shown in Fig 22. We found optical screening by melanin in 20-year old patients with STGD1 to be less than half of that in age-matched controls, with the difference diminishing at longer wavelengths.
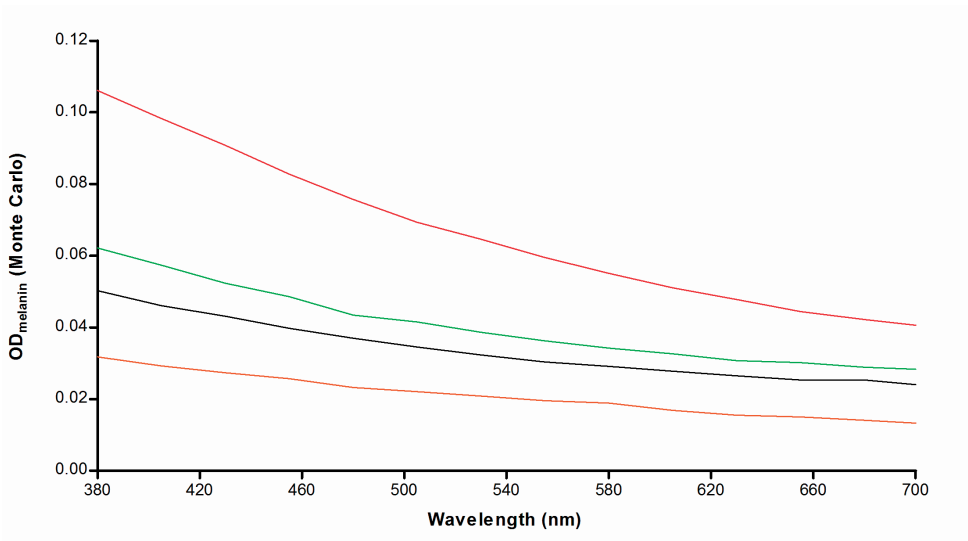
Fig 22. Light attenuation by RPE–melanin in–vivo varies with age and the presence of Stargardt disease. We calculated the total optical density (OD) of paramacular RPE-melanin versus wavelength of incident radiation with Eqs. 4-6 based on results of Monte-Carlo simulations. Colored lines indicate attenuation in healthy people of different ages: 20 (red), 40 (green), and 60 (orange). The same is shown for a 20-year old patient with STGD1 (black).

3.3 Light absorption by lipofuscin

As shown in Fig 23, we found a strong correlation between calibrated fundus AF measurements (qAF_8) and values we consider indicative of light absorption by lipofuscin $(n_g \cdot l)$. Based on a linear regression model and our calculated average qAF_8 value of patients with STGD1, we interpolated the value of $(n_g \cdot l)$ in these patients.
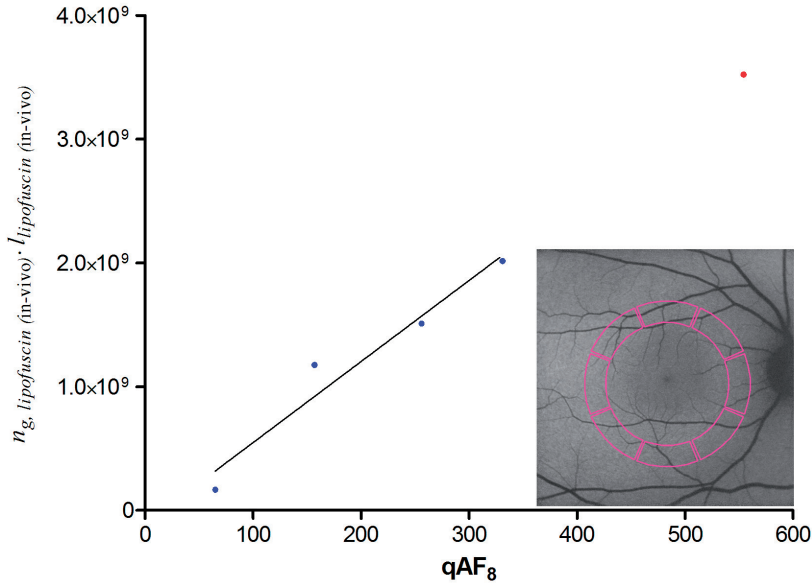
Fig 23. Correlation between calibrated fundus AF measurements and histologic data on lipofuscin granules. We considered the product of optical path length (l) and granule concentration (n_g) to be indicative of light absorption by lipofuscin granules. Here, we tested whether this product correlates with calibrated fundus AF measurements published earlier ('qAF$_8$'),[134, 135, 191] possibly allowing an estimation of this product $(n_g \cdot l)$ in patients with STGD1 based on their qAF$_8$ values. qAF$_8$ values were measured in the posterior pole of the fundus (colored area in the inset). Blue dots represent average values of healthy people of different age-ranges; the red dot represents average values of patients with STGD1 (age < 30 years). Pearson's correlation (r = 0.97) was significant (P = 0.0259); therefore, a linear regression analysis was performed with data from healthy people (solid line). With the average qAF$_8$ value of patients with STGD1, we extrapolated the value of $n_g \cdot l$ in Stargardt disease prior to atrophy of the RPE (red dot).

3.4 Oxygen photoconsumption by lipofuscin

We used the results obtained in sections 3.1 - 3.3 together with data on the oxygen concentration in the RPE in-vivo to normalize for differences with in-vitro studies on isolated lipofuscin granules (Eq. S7).[198] Fig 24 shows age-related differences in the rate of oxygen uptake (pM·cm^{-2}·s^{-1}) during sunlight exposure. This is particularly evident for short-wavelength visible light. However, in patients with Stargardt disease, we found an amplification of the rate of oxygen photoconsumption regardless of wavelength. We integrated the results along λ to better compare results for different ages, and healthy versus Stargardt disease (Fig 25). This also facilitates a comparison of low-intensity, broadband radiation (diffuse sunlight) and high-intensity narrowband laser light (fundus AF excitation light). Interestingly, the total rate of oxygen uptake during diffuse sunlight exposure in-vivo varies little with age according

to our simulation. During fundus AF, however, oxygen uptake increases considerably with advancing age. The results suggest that oxygen uptake by lipofuscin is increased by about 3.3-fold in 20-year old patients with STGD1 as compared to age-matched controls. To be more specific, during diffuse sunlight and fundus AF imaging, this fold-increase is 3.292 and 3.264, respectively. When comparing oxygen uptake during either exposure to diffuse sunlight or fundus AF, we found a 1.33-, 1.70-, and 2.39- fold increase for healthy individuals aged 20, 40, and 60, respectively. For patients with Stargardt disease, we found a 1.32- fold increase, *i.e.* close to that in age-matched controls.
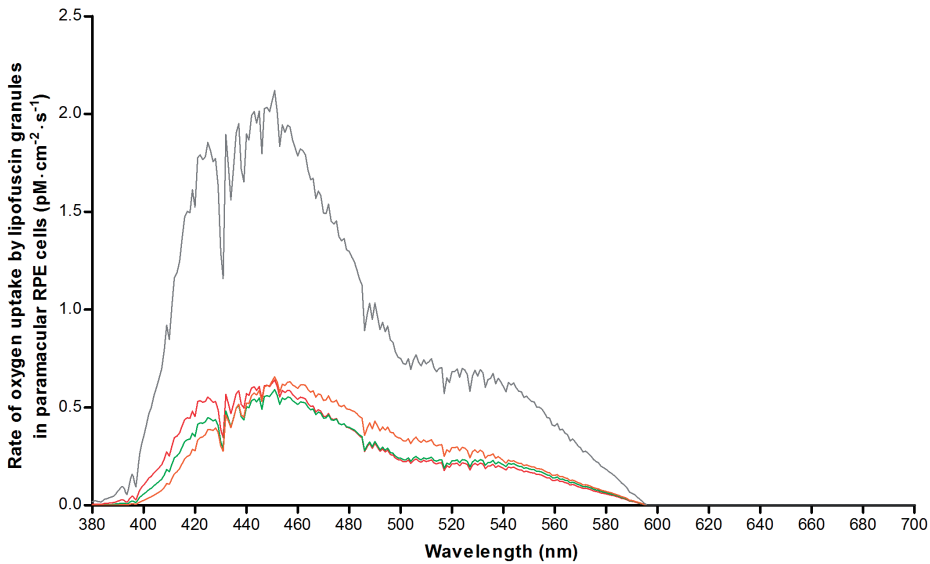
Fig 24. Numerical simulation of oxygen uptake by lipofuscin in paramacular RPE in–vivo during exposure to diffuse sunlight. Oxygen uptake was calculated based on results from a previous investigation of oxygen uptake by isolated human lipofuscin granules,[198] after correction for factors affecting retinal exposure levels in-vivo (see text). Results were plotted for healthy people of different ages: 20-year old (red), 40-year old (green), and 60-year old (orange). Results for 20-year old patients with STGD1 are also shown (grey).
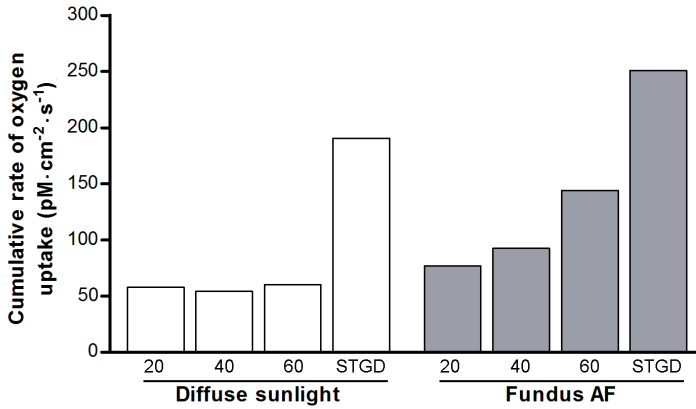
Fig 25. Total rates of oxygen uptake by lipofuscin during light exposure. Rates of oxygen uptake (see Fig 24) were integrated along the wavelength of incident radiation to obtain the total rate of O_2-uptake, as an indication of cellular oxidative stress in-vivo during exposure to diffuse sunlight (white bars) or fundus AF (grey bars). X-axes: Age of healthy individuals, or patients with STGD1 (age, 20).

4. Discussion

Herein, we performed a comprehensive simulation of photo-oxidative stress in the RPE in-vivo, which suggested that lipofuscin granules had a 3-fold higher oxygen uptake and light absorption in patients with STGD1 compared to age-matched controls. To our knowledge, this is the first study to report STGD1 patients' relative sensitivity to light. We incorporated all known factors influencing light-induced oxygen consumption by RPE-lipofuscin, insofar sufficient empirical data was available.

4.1 Optical screening

We identified differences in optical attenuation ($\mu_{melanin}$) by RPE melanosomes between our simulated in-vivo data and earlier ex-vivo studies. Weiter *et al.* (1986)[185] found a total attenuation of 0.022 ± 0.008 OD·μm^{-1} in the apical part of RPE-cells (λ = 500-600 nm). This agrees well with the pooled average result of our MC simulation for healthy people aged 20-60 (0.020 ± 0.002 OD·μm^{-1}). The difference in $\mu_{melanin}$ may lie in two facts. First, we simulated a declining concentration of melanosomes with age, whereas Weiter *et al.* did not take age into account and could not distinguish between melanin and melanolipofuscin.[185] Our MC simulation would probably have shown a higher $\mu_{melanin}$ if we had included melanolipofuscin granules, since the latter granules are known to accumulate with advancing age concomitant with reductions in melanosomes.[199] Second, our simulated 'layer' of melanosomes (1 – 3 μm) was thinner than the histologic sections used by Weiter *et al.* (8 μm).[185] As we showed in Fig 21, there is a lower proportion of backscattered photons in our simulation causing an overall lower $\mu_{melanin}$.

However, optical screening by melanin only marginally protects lipofuscin against irradiation. At an $OD_{melanin}$ of 0.05, only about 11% of incident light is filtered. Assuming that optical parameters of melanosomes are unchanged in STGD1—as indicated by their normal morphological appearance[197]—the MC simulation showed a 50% lesser screening effect as compared to age-matched controls (Fig 22). Therefore, our data indicates that the apical displacement of melanin in RPE cells of patients with STGD1[197] is of little consequence with regard to intracellular optical screening.

The optical absorption by visual pigments (VP) in photoreceptors should be very low under the aforementioned luminance of 4400 cd·m^{-2}, leading to a minimal VP optical screening effect. A luminance of 2.9 photopic cd·m^{-2} is already sufficient to saturate rod electroretinographical responses, and therefore the unbleached fraction of rod VP will be very low. Based on photoreceptor topography data from Curcio *et al.*,[200] rods constitute about 72% of the paramacular surface at 10° foveal eccentricity, taking into account the relative sizes of rods and cones in that area and their population densities. We estimate that the VP OD of the various cones in that area varies between 0.004 and 0.008 depending on wavelength, considering the relative numbers of blue, red and green cones,[201] their outer segment lengths, ex-vivo absorption spectra,[201] and the steady-state bleached fraction of VP [202] at 4400 cd·m^{-2}.

4.2 Light absorption by lipofuscin

Comparison of light-induced oxidative stress in patients with STGD1 versus healthy controls requires correction for differences in light absorption. Earlier studies used lipofuscin AF as an indication of the concentration of fluorophores.[166, 185] Because calibrated fundus AF measurements[134] are the only quantitative in-vivo indication of the fluorophore concentration, we investigated its correlation with histologic data of the concentration of lipofuscin granules. The fraction of light absorbed *(A)* can be calculated by the formula $A = n_g \cdot l \cdot \sigma_a$,[203] and as shown in Fig 23, we found calibrated fundus AF and *(n$_g$·l)* to be linearly proportional. We considered the latter directly related to the amount of light absorption, because of two indications of an age-invariant absorption cross-section (σ_a). First, our image analysis of previously published[188] electron microscopy images shows no age-related difference in granule size (results not shown), ruling out a change in the amount of light scattering. Second, the optical density of lipofuscin granules decreases only slightly (0 - 14%) with age.[188] In the context of unchanged scattering by these granules, absorption will only marginally change with age. One aspect of note is the increased fluorescence efficiency of oxidized bisretinoids,[52] with the oxidized form of A2E being the strongest fluorophore among them.[204] Also, in lipofuscin granules, the ratio of oxidized A2E versus unoxidized A2E increases considerably with age.[204] These results indicate that increased qAF may not correspond with equally increased light absorption. Another aspect to consider is the effect of internal optical screening among lipofuscin granules at high concentrations, due to the high optical density

of each granule.[188] This would also cause a lack of linear proportionality between total light absorbed and the granule concentration, especially at high concentrations. Since these two aspects would lead to an overestimation of the amount of light absorbed at high qAF_8 or high granule concentrations, a linear relationship between qAF_8 and $(n_g \cdot l)$ may be expected. On the other hand, this means that light absorption in patients with STGD1 is probably increased by less than 3-fold.

4.3 Oxygen uptake

Our results suggest that RPE-cells of patients with STGD1 are at increased risk of oxidative stress. During SW-AF-imaging, the potential for oxidation almost doubles from age 20 to age 60 (Fig 25). We found a 3.3-fold increase in the rate of oxygen uptake in 20-year old patients with STGD1 relative to that in age-matched controls, regardless of the exposure regime. However, we cannot conclude whether the oxidant/anti-oxidant balance is affected, and if permanent impairment will occur to the RPE or photoreceptor cells. RPE cells are highly resistant to oxidative stress,[205] but survival of RPE cells under light stress is largely determined by the proportion of lipofuscin and melanosomes.[206] This balance is clearly less favorable in patients with STGD1; the limited anti-oxidative capacity afforded by melanosomes may prove insufficient to cope with situations of increased oxidative stress when it would normally suffice. Perhaps more importantly are indirect effects related to the photoreceptors; evidence has shown that outer segment phagocytosis by RPE-cells is decreased under conditions of oxidative stress.[207, 208] Impairments in this key function of RPE-cells can result in retinal degenerations.[209]

Although we calculated oxygen uptake in STGD1 under the assumption that the photophysical characteristics of RPE-lipofuscin remain unchanged, this may prove incorrect considering the 'abnormal form of lipofuscin' noted by a histological study of STGD1.[197] Furthermore, we have not evaluated the consequences of the consumed oxygen; that requires future work that is able to replicate the in-vivo micro-milieu of RPE cells. We anticipate that this will yield insights into the tolerance of RPE-cells to oxidative stress under physiological cell culturing- and light exposure- conditions. It is of interest to note that AF-imaging in patients with STGD1 at λ = 532 nm, instead of 488 nm, leads to less oxygen uptake at equal optical power: a 0.98-fold versus a 1.32-fold increased uptake relative to daylight, respectively.

4.4 Limitations

This study had several limitations. First, melanosomes can reduce iron-mediated oxidation in RPE in-vitro by protecting against redox-active metal ion-mediated oxidation.[210, 211] However, whether the net result of this process is anti- or even pro-oxidant depends on many factors, such as relative concentrations of metal ions, small molecular weight ion chelators and melanin-binding sites, presence of oxygen, and irradiation conditions.[211] Due to lack of related in-vivo data on these parameters and their interactions, we omitted this part from

our simulation of oxidative stress. Second, the aerobic photoreactivity of melanosomes and melanolipofuscin was not taken into account. These granules display about 6- and 3-fold less oxygen uptake upon irradiation,[212] respectively. In addition, in comparison to lipofuscin, they have a relatively high yield of hydrogen peroxide,[212] which has a long half-life [213] and thus is less prone to cause unwanted oxidative damage. Also, melanolipofuscinogenesis involves a gradual fusion of two granule types,[214] and optical characteristics and oxygen uptake may differ with advanced progression which may be difficult to model accurately in an MC simulation.

4.5 General conclusions
Our numerical simulation of susceptibility to phototoxicity in health and disease indicated a substantial increase in the rate of oxygen uptake by lipofuscin in patients with STGD1. However, sufficient empirical data is lacking on the molecular dynamics of the interplay between increased oxygen uptake, synthesis of oxygen radicals, anti-oxidants, and mechanisms leading to permanent retinal damage. Unfortunately, current in-vivo measurement techniques are insufficiently sensitive to show any effect of sub-threshold light damage in patients. Considerable insight into these dynamics can be gained by numerical simulation and comparisons with empirical data obtained in cells cultured in replicated (patho)physiological conditions. Simulations can also elucidate the relative vulnerability of various retinal areas with different characteristics. We anticipate that this can eventually lead to personalized risk assessments of patients undergoing retinal light exposure in various settings. In high risk patients it may be advisable to largely avoid chronic exposure to light with wavelengths less than 500 nm and to choose autofluorescence excitation above this wavelength.

Appendix
1. Diameter of pupils adapted to daylight
2. Optical screening by melanin in-vivo
3. Optical absorption by lipofuscin in-vivo
4. Oxygen photoconsumption by lipofuscin
5. Table of incorporated parameters

1. Diameter of pupils adapted to daylight
The diameters of pupils adapted to daylight were based on normative data measured at 4400 cd·m^{-2} for the ages 20, 40, and 60.[176] This outdoor lighting condition was chosen, because an overcast day illuminates by about 2200 cd·m^{-2} while full daylight gives about 22700 cd·m^{-2} for the respective illuminances of 1075 and 10752 cd·sr·m^{-2}.[215] We assumed the angle θ subtended by the source (daylight) to amount to 45 degrees (0.79 rad), which gives a solid angle Ω of 0.49 sr based on the formula $\Omega = \frac{\pi}{4}\theta^2$

2. Optical screening by melanin in-vivo

In order to determine the optical transmission through melanosomes in the RPE, we performed a Monte-Carlo simulation of light scattering and absorption based on Mie theory. We used the program MontCarl,[216] which simulates photons as wave packets (*i.e.,* 'photons'). MontCarl allows the user to define properties of 1) the source, 2) the scattering volume with internal layers and objects, 3) scattering and absorptive properties of particles with different sizes, 4) descriptions of their location and concentration, and 5) methods of photon detection.[217, 218]

Monte-Carlo simulations require at least 5 basic parameters; 1) wavelength of the radiation and refractive indices of the media and scattering particles, 2) the absorption and scattering cross-sections of the particles, 3) the particle concentration, 4) the particle diameters, and 5) the dimensions of the system in which scattering takes place. We will address the relevant calculations only briefly, because optical screening by melanin is not the main focus of this study.

2.1 Light absorption by melanin granules

The absorption coefficient of melanin ($\mu_{a,\ melanin}$) may be estimated with information on the concentrations of eumelanin and pheomelanin monomers in a tissue, and using the extinction coefficients of Sarna and Schwartz (1988):[203, 219]

$$\begin{aligned} \varepsilon_{\text{eumelanin}} &= (2.37 \times 10^4 \text{ cm}^{-1} \text{ M}^{-1}) \text{ e}^{-0.0056\lambda}, \\ \varepsilon_{\text{pheomelanin}} &= (1.01 \times 10^5 \text{ cm}^{-1} \text{ M}^{-1}) \text{ e}^{-0.0087\lambda}, \end{aligned} \tag{S1}$$

such that the absorption due to melanin is:[203]

$$\mu_a \text{ due to melanin} = (\varepsilon_{\text{eumelanin}} C_{\text{eumelanin}} + \varepsilon_{\text{pheomelanin}} C_{\text{pheomelanin}}) \ln(10). \tag{S2}$$

We calculated the average diameters of melanin granules using scanning electron microscopy images of isolated RPE melanosomes published earlier (Ref 220, Fig 5B). Since many of these granules are ellipsoidal rather than spherical, we segmented the granules with ImageJ (version 1.48v; http://imagej.nih.gov/ij/; provided in the public domain by the National Institutes of Health, Bethesda, MD, USA), and measured their surface area. We calculated an average sphere-equivalent diameter of 0.786 ± 0.17 μm. Assuming that sphere diameter is normally distributed, we can discretize the distribution by defining 9 classes of granules, *i.e.* each class has a specific size and concentration. MontCarl is able to calculate scattering characteristics of discrete classes of scatterers based firstly on contributions from various angular scattering functions (*e.g.,* 100% Mie function, 100% Henyey-Greenstein, or other combinations), and second with the value of the relevant input parameters of each contribution.

At young age, melanosomes occupy approximately 33% of the apical RPE cell cytoplasm in-vivo.[221] Feeney-Burns determined that melanosomes constitute 8% of the cross-sectional area of an RPE cell in the first two decades of life [199] and, according to the Delesse principle, the area fraction of a tissue component gives an estimate of its volume fraction.[222] From these data we can calculate that each paramacular RPE-cell contain about 552 melanosomes, giving a concentration of $9.41 \cdot 10^{11}$ granules·ml^{-1}. Although RPE melanosomes consist *largely* of eumelanin,[178, 223] we made the simplifying assumption that they consist *entirely* of eumelanin monomers. At an average granule diameter of 0.786 μm, the concentration of eumelanin monomers in the paramacular RPE (M) is then 0.111 M, which allows us to calculate ($\mu_{a,\ melanin}$) (Eq. S1).

At ages 40 and 60, respectively, melanin constitutes 6% and 3.5% of the RPE-cell area/volume.[199] This decline is coincident with a proportional increase in melanolipofuscin [199] presumably due to gradual fusion of melanosome with lipofuscin granules.[214] This is consistent with observations that 1) the polarized distribution of apical melanin and basal lipofuscin is lost with advancing age;[185, 214] 2) that by age 50 most melanin is incorporated into melanolipofuscin;[185] and 3) that by age 90 melanosomes represent almost all RPE pigment granules.[224] The physical implication of this decline is that the optical path length through melanin decreases with age. According to this principle, melanosomes occupy the apical 25% at age 40 and 14.57% at age 60 while maintaining the same local concentration. Histopathology of a 24-year old patient with Stargardt disease revealed a striking apical displacement of melanosomes to the estimated apical fifth part of peripheral RPE-cells.[197] In the posterior pole, a less prominent division line was observed, and melanin content appeared reduced in these cells.[197] We consider it likely that melanolipofuscinogenesis underlies these observations, which may be more complete in posterior RPE-cells as compared to peripheral RPE-cells. Our study is focused on paramacular RPE-cells. Therefore, based on these observations we estimate that melanin is concentrated in the apical 1/5th of the paramacular RPE-cell and that the basal 50% of these granules have been partially incorporated into melanolipofuscin and no longer contributes to effective optical screening. The layer thickness of 'pure' melanin is then approximately 1 micron whereas the local melanosome concentration is increased by 40% higher than normal. The melanosome morphology appeared normal in Stargardt disease,[197] and therefore we assume that granule absorption and scattering characteristics remain unchanged.

With μ_a and the granule concentration (n_g) known, the average absorption cross-section of the melanin granules ($\sigma_{a,\ melanin}$) can be calculated with the well-known relation:

$$\sigma_a = \mu_a / n_g. \tag{S3}$$

σ_a is related to the particle diameter D and the absorption efficiency $\mathbf{Q}_{abs}$ as:

$$\sigma_a = \frac{\pi D^2 \mathbf{Q}_{abs}}{4}. \tag{S4}$$

With the wavelength-dependent $\mathbf{Q}$abs known, we were able to calculate the wavelength-dependent absorption cross-section of the melanin granules.

2.2 Scattering by melanin granules

Mie theory calculates the angle-dependent scattering function of incident radiation based only on the particle aspect ratio *(X)*, the wavelength of incident radiation and the refractive index of the particle material; the former 2 parameters should incorporate the medium of refractive index *(n)*. The ability of the 'full' Mie function to accurately describe a particle's angular scattering functions depends on the accuracy of aforementioned input parameters. In contrast, several earlier studies on biological tissues have employed the Henyey-Greenstein (HG) approximation to describe angular scattering,[182, 184, 223] and have found it to be appropriate.

As input, the HG-function only requires an accurate estimation of the scattering anisotropy factor *(g)*. This parameter can be calculated by employing Mie scattering theory,[225, 226] and using knowledge of the particle aspect ratio and the relative complex refractive index *m = (n + in')/N* of the material. The interested reader is referred to references 226 and 184 for further details. The refractive index of bulk material *N* was assumed to be 1.33, *i.e.* equal to that of water. The real part of the refractive index of melanin *(n)* has been determined experimentally to be 1.7.[227] Mie theory states that the imaginary part of the refractive index is related to the absorption coefficient (μ_a) by: [225]

$$\mu_a = \frac{4\pi n'}{\lambda}. \tag{S5}$$

The absorption coefficient profile of a single melanin granule varies as:[228]

$$\mu_a = c \cdot \lambda^{-3.48}. \tag{S6}$$

A value for *c* = 6.49 x 10^{12} was determined for melanin from RPE cells.[228] By combining Eqs. (S5) and (S6), we can calculate that *(n')* ranges from 0.0137 (λ = 380 nm) to 0.0035 (λ = 700 nm). This provided us with enough information to calculate g; and consequently the angular scattering functions of melanin granules. The HG-function only describes the angle-dependent behavior of scattering; the calculation of the scattering cross section σ_s has to be done by other means. To this end, we calculated the total σ_a on the basis of Mie scattering as described previously,[225, 229] and inserted this as a separate factor into the HG expression.

3. Light absorption by lipofuscin in-vivo

As stated in section 3 of the paper, we accounted for differences in optical absorption by lipofuscin by factoring in the product of the granule concentration and optical path length $(n_g \cdot l)$. Paramacular RPE-cells have a density of 5000 cells·mm^{-2} [230] and an average cell height of 8.8 μm.[185] Lipofuscin granules constitute 7 - 9% of the cell between age 11-50 and 12% between age 51-70.[199] Granules are present both in the periphery[230] and surrounding the nucleus,[206] and lose their polarized distribution from apical melanin granules with advancing age.[185] With a granule diameter of 1 - 1.2 μm in the adult RPE,[231] we can then calculate a concentration of $1.16 – 2.58 \cdot 10^{11}$ lipofuscin granules·ml^{-1} (136 – 303 granules per cell). The optical path length in aforementioned in-vitro experiment of oxygen uptake by lipofuscin granules was 332.5 μm (n_{medium}= 1.33, cuvette path length = 0.25 mm) and the granule concentration was $7.6 \cdot 10^9$ granules·ml^{-1}.[198] In paramacular RPE cells, the average optical path length varies from 7.8 μm (basal 66% at age 0-30) to 9.1 μm (basal 78% at age 31-50) to 10.4 μm (basal 89% at age 51-80). In patients with Stargardt disease, it is 9.4 μm (basal 80% at all ages).

Values of fundus AF in the posterior pole were based on measurements performed in the presence of a calibrated fluorescence reference to normalize fundus AF intensities for fluctuations in laser power and detector gain.[134] The measured values ('qAF') were averaged over 8 specific regions of the posterior pole (see inset in Fig 6 of the main paper). The resulting values ('qAF$_8$') were reported, and a best-fit model of the average qAF$_8$ for a given age was developed based on a 277 healthy individuals aged 5-60.[191] For healthy individuals, we calculated average qAF$_8$ values based on this model for the same age ranges used to calculate $(n_g \cdot l)$ as specified above. An average qAF$_8$ value for patients with STGD1 was calculated based on values reported previously (Fig 3 in paper by Burke *et al.*, 2013)[135], although we decided to only average qAF$_8$ values of the 35 patients below the age of 30. We have two reasons for doing so. First, no correlation of qAF$_8$ with age was found for patients with STGD1.[135] Second, for older individuals the presence of atrophic RPE was noted in the 8 regions used for calculating qAF$_8$, which may artificially lower their qAF$_8$ values.[135] The reported qAF$_8$ levels[135] appeared to decline sharply beyond the age of 30.

4. Oxygen photoconsumption by lipofuscin

Rates of oxygen photoconsumption, at ages ≤40 and 41-80 years, were normalized to the incident photon fluxes and to the concentration of lipofuscin granules ($7.6 \cdot 10^9$ granules·ml^{-1}) by Rozanowska and co-workers.[198] Therefore, we converted the retinal exposures during AF imaging and exposure to daylight (in mW·cm^{-2}) to wavelength-dependent incident photon fluxes (ϕ_p) by ϕ_p (s^{-1}cm^{-2})= H_r / E_{photon} = $H_r \cdot (\lambda / h \cdot c)$ where E$_{photon}$ denotes the photon energy, h the Planck constant, and c the speed of light in vacuum (Eq. S8). At a normalized ϕ_p of $1.61 \cdot 10^{16}$ photons·cm^{-2}·s^{-1}, the fluence rate ranges from 5.7 – 10 mW·cm^{-2}, which agrees well with the range at the sample surface reported earlier (0.5 – 12 mW·cm^{-2}).[198]

The pH of the solvent used (PBS) and RPE cytoplasm is the same (7.4), although the temperatures differ ($T_{in\,vitro} \approx 21°C$; $T_{in\,vitro} \approx 36.5°C$). The maximum oxygen concentration during aforementioned oxygen uptake measurements was 0.26 mM.[198] In the RPE of a light-adapted retina in-vivo this value should be less than 0.123 mM, which is the concentration of oxygen solubilized in pure water at a partial oxygen pressure of about 75 mm Hg.[232, 233] Note that the yield of singlet oxygen increases substantially at oxygen-saturated conditions relative to air-saturated conditions.[234]

We propose to calculate oxygen uptake by lipofuscin as in Eq. (S7). Here, we correct for differences in the influx of photons ϕ_p, media absorption and screening by melanosomes, for the increased optical absorption by lipofuscin in-vivo, and for differences in the concentration of solubilized oxygen relative to that used previously. This is based on the assumption that the rate of oxygen uptake by lipofuscin is proportional to the concentration of solubilized oxygen. We obtain:

$$\text{Lipofuscin O}_2 \text{ - uptake } (in\ vivo) =$$
$$\text{Lipofuscin O}_2 \text{ - uptake } (in\ vitro) \cdot \frac{\Phi_p\ (in\ vivo)}{\Phi_p\ (in\ vitro)} \cdot \frac{[\text{O}_2]\ (in\ vivo)}{[\text{O}_2]\ (in\ vitro)} \cdot \frac{n_{g,\ in\ vivo} \cdot l_{in\ vivo}}{n_{g,\ in\ vitro} \cdot l_{in\ vitro}}, \qquad (S7)$$

where

$$\Phi_p\ (in\ vivo) = \left(\frac{H_r}{E_{photon}}\right) \cdot \exp\left(-\text{OD}_{melanin,\ in\ vivo}\right) = H_r \cdot \left(\frac{\lambda}{h \cdot c}\right) \cdot \exp\left(-\text{OD}_{melanin,\ in\ vivo}\right). \qquad (S8)$$

5. Incorporated parameters

Table S1. List of parameters used in this study.

Parameter	Definition	Parameter	Definition
H_r	Retinal exposure	H_c	Corneal exposure
H_{pupil}	Pupil area	A_{retina}	Retinal area
τ	Optical transmission through the lens and ocular media	D_λ	Wavelength-dependent optical density of ocular lens and media
D_p	Pupil diameter	f_e	Focal length of the eye
α	Visual angle	L_s	Irradiance of the source
Ω	Solid angle	θ	Angle subtended by light source
λ	Wavelength	φ	Optical power
μ_a	Absorption coefficient	μ_s	Scattering coefficient
μ'_s	Reduced/ back scattering coefficient	OD	Optical density
ε	Molar extinction coefficient	C	Concentration (mol·L-1)
l	Optical path length	M	Molarity (mol·L-1)
σ_a	Absorption cross-section	σ_s	Scattering cross-section
D	Particle diameter	Q_{abs}	Absorption efficiency
N	Refractive index (bulk material)	m	Complex refractive index (granules)
n	Real refractive index	n'	Imaginary refractive index
g	Scattering anisotropy factor	X	Particle aspect ratio
c	Scaling factor of melanin absorption coefficient profile	N_g	Granule concentration
qAF_8	Calibrated fundus AF intensity, average of 8 areas in the posterior pole	φ_p	Photon flux
E_{photon}	Photon energy	h	Planck constant
C	Speed of light in vacuum	T	Temperature
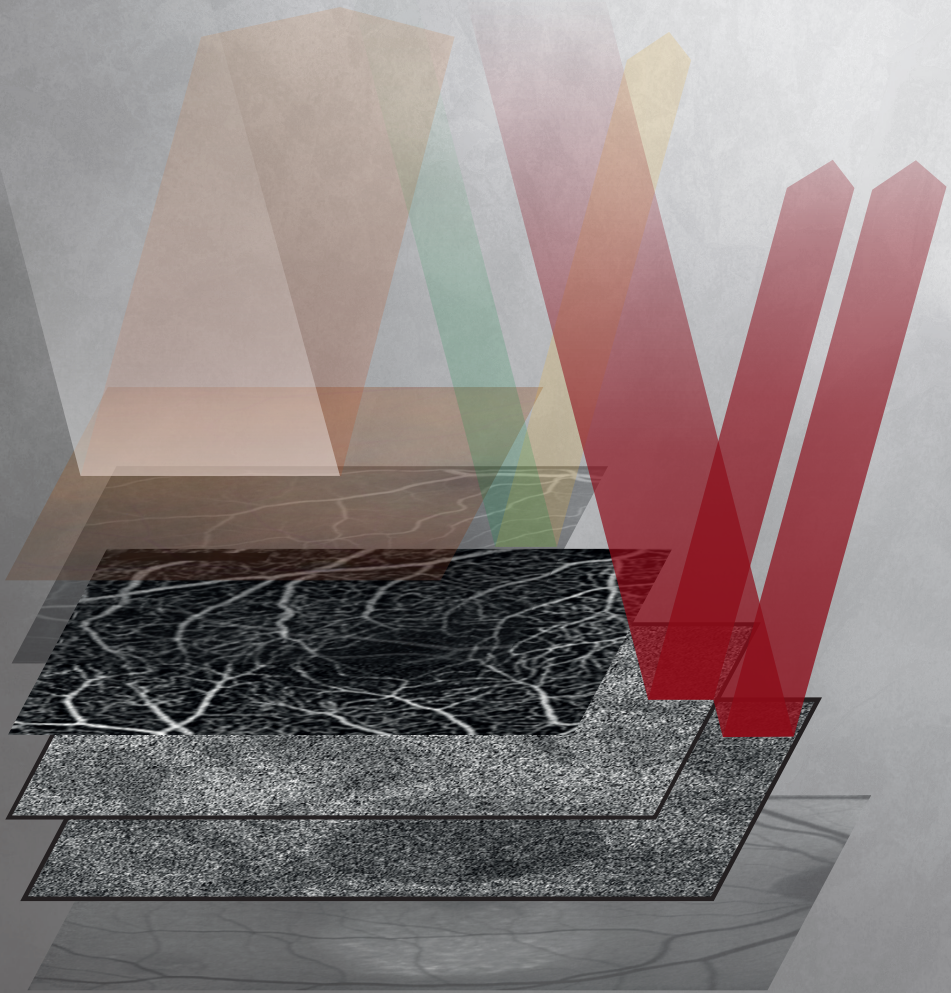
Chapter 3.

Optical coherence tomography
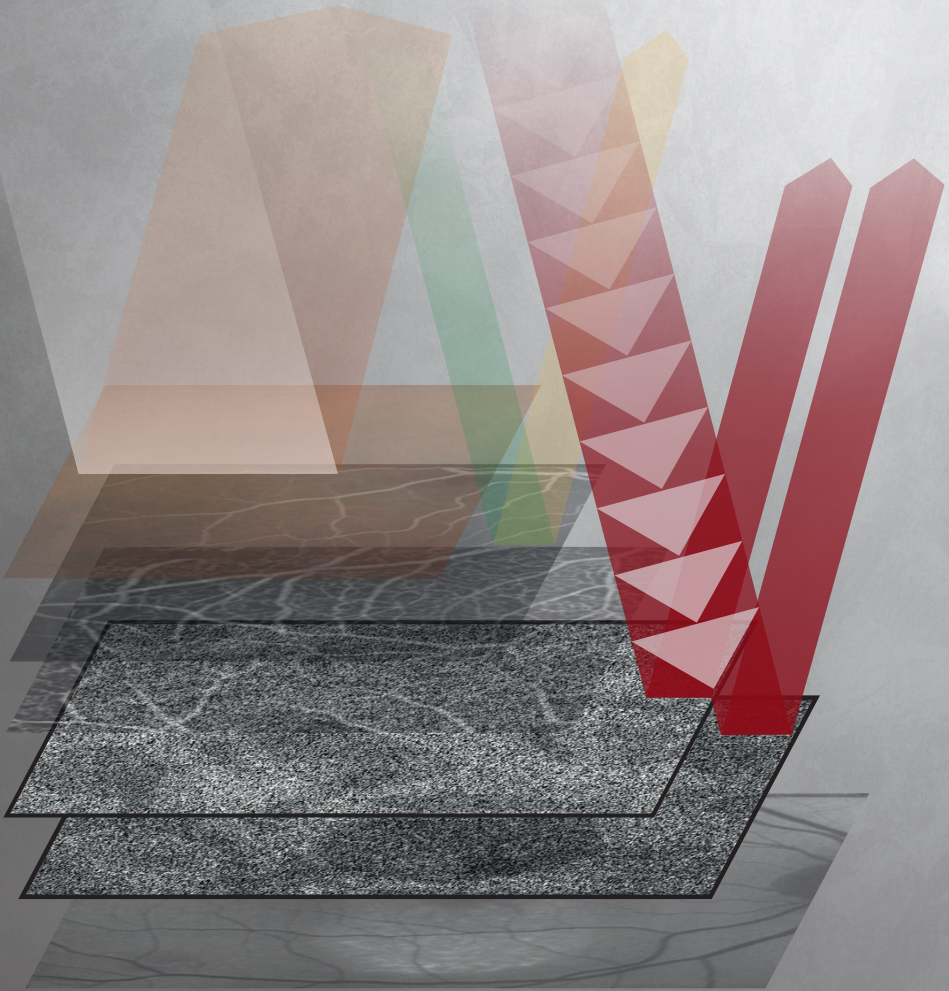
Chapter 3.1

Impact of motion–associated noise on intrinsic optical signal imaging inhumans with optical coherence tomography

Michel M. Teussink
Barry Cense
Mark J.J.P. van Grinsven
B. Jeroen Klevering
Carel B. Hoyng
Thomas Theelen

Abstract

A growing body of evidence suggests that phototransduction can be studied in the human eye in-vivo by imaging of fast intrinsic optical signals (IOS). There is consensus concerning the limiting influence of motion-associated imaging noise on the reproducibility of IOS-measurements, especially in those employing spectral-domain optical coherence tomography (SD-OCT). However, no study to date has conducted a comprehensive analysis of this noise in the context of IOS-imaging. In this study, we discuss biophysical correlates of IOS, and we address motion-associated imaging noise by providing correctional post-processing methods. In order to avoid cross-talk of adjacent IOS of opposite signal polarity, cellular resolution and stability of imaging to the level of individual cones is likely needed. The optical Stiles-Crawford effect can be a source of significant IOS-imaging noise if alignment with the peak of the Stiles-Crawford function cannot be maintained. Therefore, complete head stabilization by implementation of a bite-bar may be critical to maintain a constant pupil entry position of the OCT beam. Due to depth-dependent sensitivity fall-off, heartbeat and breathing associated axial movements can cause tissue reflectivity to vary by 29% over time, although known methods can be implemented to null these effects. Substantial variations in reflectivity can be caused by variable illumination due to changes in the beam pupil entry position and angle, which can be reduced by an adaptive algorithm based on slope-fitting of optical attenuation in the choriocapillary lamina.

Introduction

In many important eye diseases, such as age-related macular degeneration,[235] retinitis pigmentosa[236] and Stargardt disease, pathologic changes of retinal photoreceptors are the hallmark of disease development. Although no treatments exist yet for retinitis pigmentosa and Stargardt disease, several research groups are currently developing gene augmentation therapy. A thorough evaluation of remaining retinal architecture and function is essential to select patients amenable for treatment. We therefore need imaging techniques that can determine miniscule changes in the structural and functional integrity of retinal photoreceptors, for patient selection but also to monitor the effects of therapy.

Current high-resolution imaging techniques, *e.g.* optical coherence tomography (OCT) and adaptive optics (AO) imaging, can already provide information on the structural tissue integrity. However, structural information alone may be insufficient to monitor functional decline.[237] It has been shown that intrinsic optical signal (IOS) imaging can help to detect neural activity (for instance, of the cortical surface of the mammalian brain).[100, 101] The principle of IOS-imaging is based on measuring the transient changes in light reflectance from tissue that are indicative of stimulus-induced alterations in neuronal activity. Reflectance changes in retinal tissue have been associated with slow (seconds to minutes) alterations in light-scattering and -absorption caused by hemodynamic activation,[238] and with fast (milliseconds to seconds) changes in the optical properties of photoreceptors.[239-241] Current in-vivo measurements of phototransduction are either confined to the initial photon absorption kinetics (fundus densitometry)[242] or to the final membrane hyperpolarization (electroretinography, ERG).[243, 244] Imaging of fast IOS, however, provides a unique opportunity to investigate the *intermediate* processes in individual photoreceptors in-vivo.[245, 246] At present, adaptive-optics ultrahigh-resolution OCT (AO-UHR-OCT) is the only in-vivo technique capable of resolving cones in three dimensions close to the fovea.[247]

In contrast to the numerous studies that demonstrated reproducible IOS in animals using ex-vivo retina preparations or in-vivo measurements under anesthesia, comparatively few studies were able to detect fast IOS in awake humans using various techniques.[239-241, 248-253] Several of these human studies showed low reproducibility due to a poor signal-to-noise ratio (SNR), caused by substantial confounding imaging noise relatively to the small IOS amplitudes. The robustness and reproducibility of the acquisition procedure are limited by its low tolerance for retinal motion and the presence of a narrow foveal avascular zone.[240] Eye motion adversely affects IOS-imaging in two important ways. First, the monitoring of the same tissue volume over time is complicated due to tissue displacements out of the field of view (FOV) and/or other motion artifacts (*e.g.* blurring and distortions). Second, the main outcome measure (reflectivity) can be significantly affected by specific eye- or head movements. The magnitude of motion-associated noise is of the same order as that of the

expected signals.[249] Although several motion artifacts in SD-OCT-imaging were analyzed previously (*e.g.* de Kinkelder *et al.*, 2011[98]), no study to date has determined how eye motion can induce noise in IOS-imaging by SD-OCT. This work aims to provide a comprehensive overview of known properties of the fast IOS and their relation to biophysical processes, and to analyze motion-associated IOS-imaging noise. Finally, we will suggest improvements to dedicated optical systems, as well image acquisition and processing, to facilitate studies on this promising technique in the living human eye.

Review of biochemical and biophysical correlates of the fast IOS

Using a variety of methods, fast IOS-imaging studies have found indications that several of the photoreceptor's optical properties change upon visual stimulation. These changes may reflect different biochemical processes.

Photons of the visible spectrum (λ = 400 – 780 nm) have a chance to be absorbed by the photoreceptor's visual pigments and to initiate phototransduction by photoisomerization of rhodopsin. In the rod and cone outer segment (OS), the likelihood of photon absorption in basal disks is greater, relative to apical disks near the OS tips. This so-called self-screening process is less pronounced in the cone OS as a consequence of its tapered structure.[254] Key processes of the phototransduction cascade are schematized in Fig 1 (a). In the process of photoisomerization of the opsin molecule, the first relatively stable isomer (Metarhodopsin II, R_{MII}) is formed about 1 ms after photon absorption. The speed of this formation is quite similar in rods and cones, regardless of their opsins' wavelengths of maximum absorption.[255-259] R_{MII} catalyzes activation of the G-protein transducin, which couples very rapidly with phosphodiesterase (PDE). This enzyme, in turn, catalyzes the hydrolysis of cyclic guanosine monophosphate (cGMP) to a very high rate for as long as it remains active (PDE*). The lifetime of PDE* depends on the inactivation of visual pigment and transducin, which in turn depend on the photoreceptor type and (in case of cones-) on light-intensity. The cytoplasmic concentration of cGMP is reduced very quickly, causing cyclic nucleotide gated (CNG) channel – bound cGMP to dissociate. In the dark, cGMP is responsible for holding open CNG channels to allow the influx of sodium, which maintains the OS membrane in a depolarized state, such that a 'dark current' flows through the cell. This dark current allows voltage-gated calcium influx channels to remain open. The resulting high intracellular calcium concentration causes constant release of the neurotransmitter glutamate in the dark. In the light then, cGMP hydrolysis causes closure of CNG channels leading to hyperpolarization, which causes closure of voltage-sensitive calcium channels along the OS, resulting in cessation of the dark current and inhibition of glutamate release.

Up to now, two types of fast IOS have been described; high-frequency intensity reversals in human cones with a duration of 300-400 ms,[239, 240] and changes in light backscatter from photoreceptors (of various species), that persist for 1-3 s.[260, 261]

The first type of IOS was detected by Jonnal *et al.* (2007).[239] Using a high-speed AO flood-illumination camera, they observed fast stimulus evoked-intensity fluctuations with random starting phase in individual cones. These results confirm that the OS can function as a 'biological interferometer' with sensitivity to sub-wavelength changes in cell length, refractive index, or scatter.[239, 262] The authors suggested that these intensity reversals are driven by interference of coherent light that is reflected off the posterior OS tips and the connecting cilium. Their detection required the source coherence length to exceed the optical path length between these structures.[239]

Similar intensity fluctuations observed with shorter source coherence lengths [240, 241, 250, 253] indicate the presence of several scattering boundaries along the OS length.[240] Of interest, similar signals were detected in 80-100% of the assessed cones,[240, 241] indicating the involvement of a common process among all types of cones. The fluctuation signals' time of onset (2-7 ms) and duration (300-400 ms) closely matched those of single-flash, single-cone electrophysiological recordings.[239, 263] This could indicate changes in cone circulating current itself or associated processes, such as membrane polarization or changing concentrations of cGMP,[240] although it is unknown whether this leads to changes in refractive index, scatter, or cell length through osmotic activity.[239, 262] The involvement of non-linear processes, such as changes in the concentration of activated opsin, transducin, or PDE*, has been ruled out, because the frequencies of these intensity reversals (which increased with stimulus strength) were variable.[239, 240]

Neuronal osmotic swelling is well known to cause increased light transmission due to reduced light scattering.[264] However, the squid and amphibian photoreceptor diameters change only for about 100 - 200 ms upon stimulation,[265, 266] which does not quite match the duration of the fluctuation-type IOS in humans.[239, 240] Unfortunately, we found no similar measurements in mammalian retinas. Further, single-cone ERG recordings in macaques show that photovoltages have largely dissipated by 200 ms,[263] which indicates that the associated ion fluxes have reduced as well. Thus, the biomechanical and ERG results show a close temporal correspondence. The discrepancy in durations of IOS and osmotic changes in the outer segments suggests that other contemporary events contribute, such as altered light scattering.

Flash stimulation, in the absence of guanosine triphosphate, can cause increased scatter from rod disk membranes due to a gain in mass of membranes when proteins are bound from solution ('binding signals').[246] These proteins include tranducin,[246] rhodopsin kinase, and arrestin.[267] In the presence of guanosine triphosphate, transducin can dissociate (Fig 26 (a), step 2), which is measurable by a 'dissociation signal' opposite in polarity to the binding signal.[246] PDE-activity also increases light scatter, which initiates after at least 10 ms in rod disks. Kinetic analysis demonstrated that light scatter due to PDE-activity exceeds the dissociation signal's reduction in light scatter.[267] Further, modelling indicates that PDE-activity in cones returns to baseline about 400 ms after photon absorption,[268] which corresponds
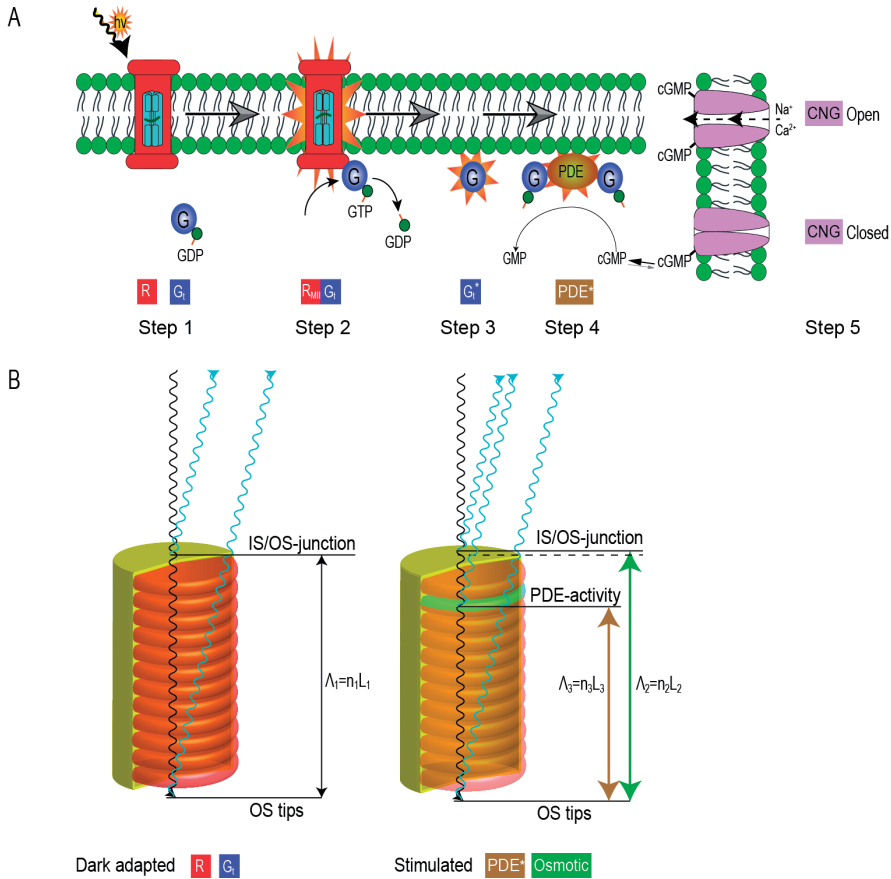
Fig 26. (a) Simplified scheme of key processes involved in phototransduction (modified from Leskov *et al.*, 2000).[269] Upon absorption of visible photons by visual pigment, consisting of rhodopsin and an opsin chromophore (R) (*Step 1*), rhodopsin undergoes conformational changes until Metarhodopsin II is formed (R_{MII}). Consequently, the G-protein transducin (G_t) is bound from solution and is enzymatically activated by R_{MII} by phosphorylation (*Step 2*). Activated G_t (G_t*) then dissociates from R_{MII} (*Step 3*). Next, two molecules of G_t* bind and activate the enzyme phosphodiesterase (PDE*) (Step 4). PDE* catalyzes the hydrolysis of cyclic guanosine monophosphate (cGMP), which is responsible for holding open cyclic nucleotide gated (CNG) channels to allow for the influx of Na^+ and Ca^{2+}. As a consequence of cGMP-hydrolysis after visual stimulation, CNG-channel bound cGMP dissociates, leading to channel closure and membrane hyperpolarization (*Step 5*). Consequently, voltage-sensitive calcium channels close, leading to cessation of the photoreceptor's dark current and inhibition of the release of the neurotransmitter glutamate. (b) The hypothesized involvement of PDE-activity in the generation of the fluctuation-type of fast IOS described earlier.[239] In the dark (*left image*), light rays impinging on the photoreceptor outer segment (black lines) reflect principally off the inner-outer segment junction (IS/OS-junction) and the OS outer tips (blue lines), with the optical path length between these structures $\Lambda_1 = n_1 L_1$. Upon stimulation (*right image*), osmotic swelling may cause changes in the optical path length (Λ_2), as well as light scatter caused by localized PDE-activity (Λ_3). This PDE-activity has a higher probability of occurring in basal disks close to the IS/OS-junction as a consequence of self-screening (see text for details).

closely with the fluctuation-type of IOS.[239] Based on these results we hypothesize that light scattering boundaries can form locally in the OS, which can contribute to optical path length changes of the 'biological interferometers'. This is schematized in Fig 26 (b). In summary, in addition to optical path length changes due to osmotic swelling, PDE-activity may be an important contributor to the interference phenomena reported earlier,[239, 240] and merits additional investigation.

The second type of fast IOS have been measured by depth-resolved OCT in different animals, where IOS of different polarities, *i.e.,* increased or decreased reflectance, were measured from retinal photoreceptors.[252, 260, 261, 270, 271] Following on initial indications of the co-existence of IOS with opposite polarity in the same area,[272] Wang *et al.* (2013) demonstrated significantly lowered IOS amplitudes in frog retina when the lateral resolution was worse than 2 µm. This signal loss is probably caused by the integration of opposite signals in adjacent photoreceptors when groups of cells are imaged in one pixel due to low imaging resolution.[273] Of interest, the SNR remained equal regardless of resolution, due to the greater amplitude of positive IOS (increased reflectance). These findings could very well explain the generally poor reproducibility of previous studies in humans.[248, 251, 252] A sound recommendation for future studies is therefore to employ AO to resolve individual cones, and to avoid pixel crosstalk by using either point-scanning OCT systems or specialized *en-face* line-scanning OCT-systems.[273]

Intriguingly, at the level of the OS, this type of fast IOS displays a random pattern (Fig 27). Previous reports suggested that the positive IOS reflect cone activity. In human retina, standard resolution UHR-OCT revealed a fast (time to peak, about 100 ms) positive signal from the inner/ outer segment (IS/OS)- junction of rods and cones,[248, 249] whereas the outer segment layer showed a fast negative signal in human retina.[248] The absence of the IS/OS junction response in light-adapted conditions and in the peripheral retina [248] suggests that the positive signal reflects cone-activity. Also, if scattering boundaries *within* the OS can explain the fluctuation-type signals that were measured with short-coherence length light sources, then they likely lead to increased backscatter in cone OS as well.[240] Further, this hints at the possibility that intracellular scattering boundaries are responsible for both types of fast IOS. High-resolution IOS-imaging studies that are able to separate rod and cone responses in humans are needed to clarify the cellular sources of positive and negative IOS.
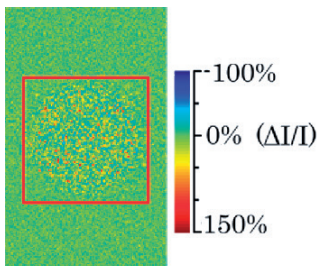

Fig 27. Fast IOS-pattern in frog retina observed with line-scanning *en face* OCT after the application of a circular stimulus. The IOS in this image have similar amplitudes across the image in a random arrangement. Adapted from Wang *et al.* (2013)[273] with permission.

The biophysical underpinnings of both types of fast IOS require closer examination. The suggestion that the different polarities of the second type of fast IOS (Fig 27) resemble binding and dissociation signals of transducin[246, 274] is unlikely, since the dissociation signal is undetectable in the presence of PDE-activity that directly follows it.[267] It is possible to selectively examine the contribution of PDE-activity in IOS, by measuring IOS in functionally intact rod-dominated retinae in the presence of PDE-inhibitors such as 3-isobutyl-1-methyl-xanthine and papaverine. The important question on the previously hypothesized involvement of cell swelling in the generation of fast IOS [239] can be examined, by measuring fast IOS in the presence of CNG-channels blockers such as pseudechetoxin for rods,[275] which selectively inhibits ion fluxes and associated cell swelling. These experiments will aid in elucidating the biophysical nature of fast IOS.

Analysis of motion-associated noise

This section gives an overview of technical and biological sources of dominant noise in in- vivo IOS-imaging in humans by SD-OCT. This noise can be addressed by modifications of the imaging and stimulation concept or by image post-processing to increase the SNR. In Sections 3.1 and 3.2, the topic-related literature is reviewed. In Sections 3.3 and 3.4, our analytical work is presented.

3.1 Motion artifacts, image distortions, and recording discontinuity

Involuntary eye motion during fixation is a major cause of artifacts in OCT imaging,[276] even in highly-cooperate and healthy subjects. When the transversal velocity of the sample is high relative to the OCT-beam size and camera integration time, the transverse resolution and SNR deteriorate.[277, 278] Although high imaging speeds can reduce these effects,[278] it does not eliminate them, as they affect even multi-MHz scanning systems.[279]

Eye motion can occur as a slow shift in gaze (drift), high-frequency motions (tremor), or large, nearly instantaneous shifts in fixation (saccades).[280] Microsaccades cause the most severe motion artifacts: they occur roughly every second in healthy subjects with amplitudes of up to 30 arcmin. Eye motion can produce blurring and discontinuities of structures in B-scans, and saccades appear as ripples in OCT volumes. More complicated motion artifacts include distortions and warping in features of interest.[281] This hinders resolving and monitoring the same photoreceptors over time, which is necessary to avoid crosstalk of fast IOS.[273] That capability is offered by a combination of high-speed AO-UHR-OCT (125 kHz A-scan rate) and dedicated registration/ dewarping algorithms.[84] An alternative solution is online stabilization of retinal imaging, which has been achieved by real-time tracking and compensation for retinal motion with either hardware based systems[282] or trackers based on simultaneous scanning-laser ophthalmoscope (SLO)-imaging.[283] Although the latter can stabilize imaging up to 3.2 μm root-mean-square residual error, which is close to the level of individual

parafoveal cones, this tracker has not yet been combined with AO-UHR-OCT. Therefore, at present, the application of appropriate registration methods remains necessary. One possibility is the manual tracking of landmark cones over time in *en face* projections, followed by lateral registration of image strips demarcated by those cones.[84] Automation of this method is possible by making use of the high statistical power provided by numerous strips from images of the same location,[284] which is relatively insensitive to changes in cone reflectivity and therefore advantageous for IOS-imaging. With respect to B-scan time series, cross-correlation analysis has frequently been used to select out B-scans that were acquired at a different location than the reference location.[271]

Finally, the capacity to monitor the same tissue over time is limited when the OCT's field-of-view (FOV) is small relative to the amplitude of displacement. Cellular resolution OCT-imaging requires sufficient oversampling to maintain feature contrast and high SNR. Therefore, the detector speed typically limits the FOV. It is also limited by the size of the isoplanatic patch, which depends on the accuracy of wavefront aberration correction.[285] Therefore, a useful FOV of AO-OCT typically spans no more than 60 arcmin retinal eccentricity. Microsaccadic displacements of the retina relative to such a small FOV can be substantial because those movements commonly spread to 24 arcmin, *i.e.* nearly half of the FOV.[286] Several techniques can increase the stability of fixation and reduce the amplitude of microsaccades, such as using a combination of a bulls eye and a crosshair as a fixation target,[287] and by using a bite bar, instead of a chin rest.[288, 289] Also, large, bright stimuli used for IOS-induction in the fovea can significantly reduce fixational stability.

Many of the potential technical difficulties posed by these eye movements can be avoided by imaging of IOS at larger foveal eccentricities. In eyes endowed with good optics, individual cones can be seen at 0.5° retinal eccentricity even without adaptive optics,[290] which also holds for SD-OCT.[291] This comes with the benefit of larger FOV's with less pronounced influences of eye movements. For this promising imaging technique to gain clinical relevance, though, robust imaging of IOS at the macula lutea is required. We anticipate that this will occur with 1) future improvements of wavefront aberration correction to enable enlargement of the isoplanatic patch, with 2) the development of faster cameras to allow these systems to enlarge the FOV, and 3) by improved stabilization of AO-OCT-imaging by either hardware-based retinal tracking or automated registration methods.

3.2 Optical Stiles–Crawford effect

In 1933, Stiles and Crawford[292] discovered that a beam of light, when displaced from the pupil center, is perceived less bright (reduced luminous efficiency), in the absence of changes in focus, illumination, or pupil diameter. The general consensus is that this effect, apparent only in photopic conditions, originates from the orientation of the cone optical apertures.

They point roughly towards the same location[293] - usually the center of the pupil, although marked differences between individuals exist.[294] Its optical counterpart, the optical Stiles-Crawford effect (OSCE),[295, 296] measures the directional dependence of fundus reflections to determine cone directionality. Gao *et al.*[297] used OCT (source λ_{mean}, 842 nm) to measure cone directionality. The principal sources of retinal reflections were identified in the OS tips and the IS/OS- junction, and reflections along the OS length may also contribute.[297] In the infrared, the magnitude of the OSCE in the dark-adapted- and in the bleached state is comparable.[298, 299] Although the OSCE is quite faint in the infrared, normalized reflectance data in OCT indicate that cone reflectance changes substantially upon displacement of the OCT-beam entry position from the pupil center, as a consequence of reduced waveguiding of the imaging light through the cones.[297] These alterations may mask or mimic IOS-related dynamic optical changes and therefore contribute to motion-associated IOS-imaging noise. The magnitude of the OSCE is fairly constant from 0.5^0 to at least 3^0 retinal eccentricity, which is likely related to the more cone-like shape of the parafoveal cones.[300] However, and this is important, SLO measurements at $\lambda = 514$ nm indicate that the directionality of cones across the central retina (0.5 - 3^0 retinal eccentricity) is not symmetrical, with directionality varying between 0.05 and 0.3.[296] This suggests that, even with information on the beam pupil entry position, it is not possible to normalize for the OSCE in the stimulated region, based on the reflectivity change of a reference region at equal retinal eccentricity.

To minimize this impact, maintaining alignment with the peak of the OSCE function is important. Due to the peakedness of the OSCE in the perifoveal area, bite-bars may be critical to abolish optical misalignments caused by head motions. Since the OSCE significantly diminishes beyond 3^0 retinal eccentricity,[296] SD-OCT imaging of single cones in these locations, which is possible even without adaptive-optics,[291] is anticipated to benefit IOS-imaging in humans due to a reduced influence of this noise factor.

3.3 Sensitivity fall-off

Typically, IOS-imaging studies of fixed samples determine the presence of a dynamic optical change by pixel-wise subtraction of the intensity at time t by the mean intensity at baseline, and by normalizing to that intensity as:[272]

$$\Delta I_{x,z,t} / \overline{I}_{x,z,baseline} = \frac{I_{x,z,t} - \overline{I}_{x,z,baseline}}{\overline{I}_{x,z,baseline}}. \tag{7}$$

Eq. (7) calibrates for the intensity of background light ($\overline{I}_{baseline}$) of each sampled tissue volume, thus allowing for the extraction of dynamic optical changes ($\Delta I/I$). However, its assumption that the optical conditions governing the background intensity remain invariant over time is questionable in the case of sample motility. Characteristic for Fourier-domain OCT is the depth dependent sensitivity fall-off by which image quality rapidly degrades in

regions corresponding to deeper locations of the sample. Its causes have been discussed in detail by Nassif *et al.*[73] When the head is relatively unfettered (*i.e.,* when using a chin- and headrest), axial displacements of the sample over time caused by heartbeat,[98] breathing,[98] and bulk head motion will cause it to be sampled at different sensitivities as a consequence of depth-dependent sensitivity fall-off, thus changing the background light intensity. Fall off, *S(z)* be modeled with a Gaussian (Fig 28 (a)):

$$S(z) = \exp\left(-z^2 / \sigma^2\right), \tag{8}$$

where *z* represents the distance from zero optical path length delay, *i.e.* the position in the eye at which the optical path length differences of sample and reference arms are matched to within one coherence length. The width **σ** is the axial distance at which the sensitivity has dropped by 3 dB. Sensitivity fall-off can be measured with a mirror sample and by axial displacement of either the sample or reference arm. Signal decay with depth can be corrected by first averaging many A-scans and subtracting the result from each A-scan to remove fixed pattern noise, after which the power magnitude of each A-line can be calculated by squaring the complex depth profile. Each A-scan is then divided by *S(z)*.[301]

We illustrate the influence of fall-off on IOS-imaging with a timelapse SD-OCT measurement (without stimulation). Based on a measurement of fall-off of our system, we predict an intensity change of 2% by axial movements of only 10 μm. This system is a standard resolution (~21 μm lateral, axial ~6 μm, assuming a tissue refractive index of 1.38), high speed (70 kHz, 137 B-scans/s) SD-OCT operating at λ_{mean} = 840 nm. It is equipped with transversal motion compensation by a synchronized line- scanning ophthalmoscope (LSO)- based active retinal tracker, which is detailed further in[302]. Mis-tracked B-scans that showed a sub-threshold cross-correlation with a scan through the foveal pit were selected out. Fig 28 (b) shows a representative average of 900 B-scans after flattening to the IS/OS- junction. We segmented this junction with OCT-SEG, a standalone MatLab OCT-segmentation application[303] and coupled it with additional automated scripts written in MatLab (R2011b, The MathWorks, Inc., Natick, MA) to correct for segmentation errors and for axial registration. For each B-scan, the retinal depth was calculated as the mean depth of the IS/OS-junction. Fig 28 (c) shows a scatter plot of mean intensity in a region of interest (red box in Fig 28 (b)) versus retinal depth, before and after fall-off compensation. The data sets were fitted with models of the expected intensity decay, and of a linear (representing no correlation with depth), respectively. The correlation (Pearson's R= -0.54, $P < 10^{-4}$) indicates that 29% of the signal variance is accounted for by axial motion. The correlation disappeared after compensation (R= -0.008, P = 0.79). In Fig 28 (d), intensity and retinal depth are plotted versus time, in both the corrected and uncorrected case, which shows that depth-dependent intensity fluctuations are substantially reduced.
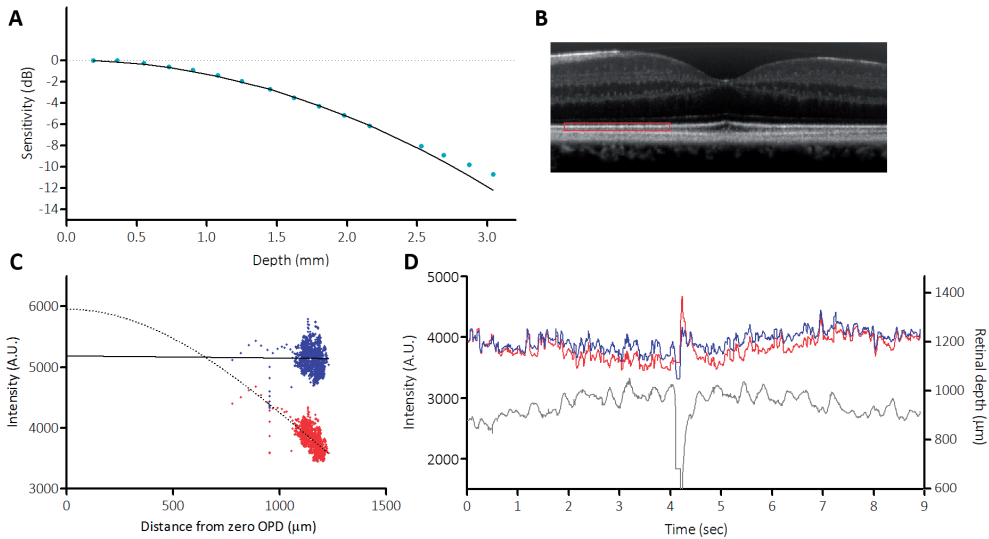
Fig 28. Effect of sensitivity fall-off on time-resolved SD-OCT imaging. (a) Measured (blue dots) sensitivity fall-off versus distance from zero optical path length delay and a Gaussian-fit (line) by using Eq. (8). (b) Mean image (n = 900) of motion-tracked B-scans after axial flattening to the IS/OS-junction. Red box: region of interest (ROI) of the IS/OS-junction, used to plot intensity data in (c) and (d). (c) Mean intensity versus retinal depth. Data is plotted before correction of sensitivity fall-off (red) and fitted with a model of the intensity decay with depth, which was calculated from sensitivity measurements shown in (a). The corrected intensity (blue) was fitted with the expected linear curve (dotted line). (d) Comparison of original (red line) and corrected (blue line) mean intensity of the ROI over time, plotted together with retinal depth (grey line), showing reduced variation with retinal depth after fall-off compensation. However, substantial variability in reflectivity remains. See text for details.

It should be noted that heartbeat causes axial shifts of $81 \pm 3.5 \mu$m,[98] in our case corresponding to about 17% intensity change. As compared to the frequently reported IOS-amplitudes of a few percent, and even compared to the largest reported IOS amplitudes (40% in individual OS in frog retina)[273], fall-off related noise can be substantial. Our results agree with previous suggestions[251] that compensation for fall-off may benefit in-vivo IOS-measurements. It should be emphasized that conditions for which the spectrometer is sensitive, such as alignment, temperature and air flow, should be stabilized to avoid significant variations in fall-off. A hardware solution to the problem is offered by swept-source OCT, which inherently suffers less from fall-off by eliminating the sensitivity of the spectrometer to higher fringe modulation.[304] However, these systems operate at longer wavelengths (1050 nm), which comes with the disadvantage of a lower axial resolution.

3.4 Illumination artifacts

Variations in the eye's light path and optical alignment can contribute to large-scale alterations in light transmission. These variations include head drifts that lead to optical axis misalignments, accommodation changes, media turbidity, floaters, and tear film quality, which colloquially contribute to illumination artifacts. A severe case of this variability can be observed when comparing the intensity of epiretinal reflections visible in Fig 29 (a) and (b) and the corresponding intensity of the outer retinal layers in two mean images corresponding to two different time periods of a B-scan time series. As explained in section 3.2, to allow for the extraction of IOS by calculating $\Delta I/I$ by means of Eq. (7), the differences in background intensity (I) caused by variable illumination must be reduced. Srinivasan *et al.* (2009)[248] proposed a normalization method, by dividing the linear amplitude reflectance of a layer of interest to that of an inert (irresponsive to stimulation) reference layer. This was helpful, but not required to detect IOS by SD-OCT.[248] This type of normalization rests on the assumption that reflectivity changes in both layers show a highly linear correspondence. To verify this, we analyzed (fall-off corrected) scans without stimulation according to Srinivasan *et al.* (2009)[248] (Fig 29). As shown in Fig 29 (c), there was a lack of linear correspondence in reflectance changes in the OS and RPE-layers, leading to inadequate compensation of illumination-related intensity fluctuations by normalization to the RPE-reflectance, shown in Fig 29 (d), indicating that this normalization method does not sufficiently normalize for illumination artifacts. This is probably due to differences in the intrinsic scattering properties of the two layers, such as angle-dependent scatter or tissue-specific attenuation coefficients.
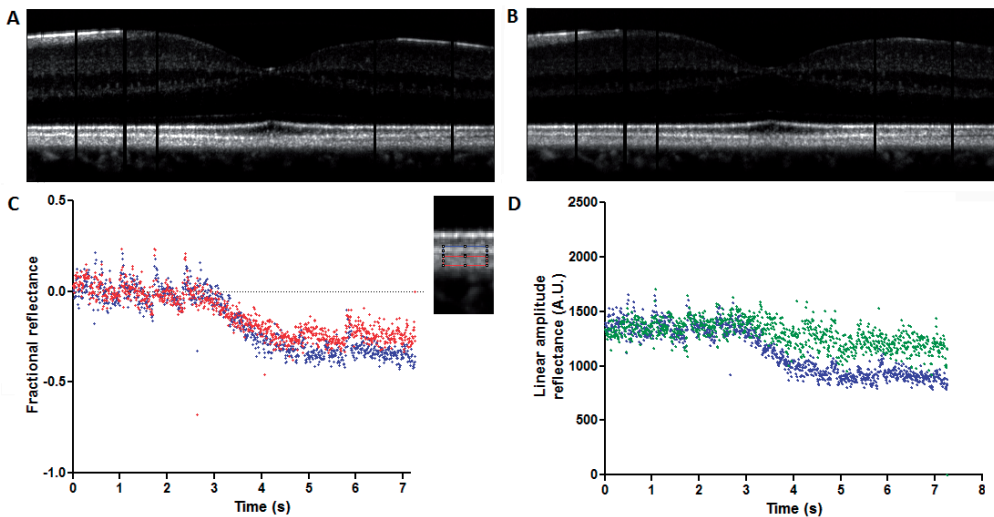
← **Fig 29. Influence of variable illumination on OCT reflectivity.** Epiretinal specular reflections are prominent in mean intensity projections of scans at t_{0-2s} (a), but less so at t_{6-8s} (b), together with increased reflectivity in deeper layers. (c) The fractional reflectivity changes of a layer of interest, such as the OS (blue dots) and a reference layer, the OS/RPE-complex (red dots) do not show a highly linear correspondence. The axial positions of these layers (inset in the top right of (c)) were identical for each B-scan. We tested if normalization to the OS/RPE complex band is sufficient to suppress noise caused by variable illumination, as proposed previously.[248] The median value of the linear amplitude reflectance of these bands was determined for each A-scan (excluding vessel shadows). A random set of these values was averaged per B-scan, and the fractional reflectance relative to the first B-scan was determined. (d) The linear amplitude reflectance of the OS-band (blue dots) still shows the change in reflectance after normalization (green dots), although a partial compensation effect is evident.

For the purpose of IOS-imaging, it is possible to estimate the background illumination by modelling its attenuation as it propagates through an inert medium with relatively stable scattering. Calibration for changes in background illumination over time allows for an approximation of the tissue's inherent scattering potential. Scattering declines exponentially with depth, and can be modelled as (modified from Zhang *et al.,* (2012)[305]):

$$I(z) = A_0 \exp(-2\mu z) + A_1, \tag{9}$$

where $I(z)$ is the reflectivity after light has travelled through a distance z in a medium with attenuation coefficient μ, and with A_0 and A_1 accounting for the illumination intensity of the incident light beam and the noise floor of the OCT image, respectively. The factor 2 is due to round trip attenuation. This single-scattering model is suited for modelling the exponential decline in the human retina.[301] By slope-fitting Eq. (9) to the decline of reflectivity with depth, with μ, A_0 and A_1 as running parameters, changes in background illumination can be estimated. Compensation for the axial confocal point spread function [306] was not taken into account in the model, since our estimated 'apparent' Rayleigh length of 860 μm in tissue would affect the estimate of μ by only 0.29 mm^{-1}, which is small in comparison to typical $\mu_{choroid}$ values of 27 mm^{-1}.[307] Since this approach is sensitive to speckle noise, A-scan averaging helps to lower speckle noise. For IOS-imaging, spatial averaging is preferable over temporal averaging. To estimate μ with sufficient confidence, reflectivity data from a minimum axial distance d = ½ / μ, of the same tissue type, must be used.[301]

The capillary lamina directly below the RPE/ Bruch membrane, indicated in Fig 30 (a), appears to be a suitable reference layer for several reasons. First, it provides a sufficient fitting range d of 18.2 μm. Second, choriocapillary blood flow (0.3 – 3.6 mm/s) is slow relative to the choroidal blood flow, virtually steady, and this layer appears to be relatively inert for the fast IOS duration, as suggested by a recent fMRI study in rats showing slow choroidal blood volume changes upon single-flash stimulation (time to onset, ~1.5 s, peak, ~27 s). Flicker stimulation induced no changes.[308] Third, changes in light scattering in this layer caused by

changes in μ are expected to be small, because capillary pulsation is very weak (to diminish the danger of rupturing the thin capillary walls) and due to the uniformity in blood flow.

Speckle noise is a major source of noise in OCT images, and it is usually suppressed by spatial or temporal averaging. In the former, neighboring pixels in one image are spatially averaged (*e.g.*, mean, median, or moving average). In the latter, the averaging occurs in time, for instance by averaging of B-scans. We suppressed speckle noise by A-scan averaging. Since changes in illumination typically occur slowly relative to the B-scan rate, the largest differences most likely arise from speckle noise. Fig 30 (b) shows a representative averaged and modified A-scan with a curve fit.

Finally, the effect of background illumination on the pixel intensity is normalized:

$$I(normalized)_{x,z,t} = \left(\frac{I_{x,z,t} - A_{1,t}}{A_{0,t}} \cdot \bar{A}_1 \right) + \bar{A}_0, \tag{10}$$

where $\bar{A}_1$ and $\bar{A}_0$ are the time-averaged values of the illumination intensity A_1 and the OCT noise floor A_0 at time t, respectively. In Fig 30 (c), the mean intensity of the combined IS/OS-junction, outer segment tips, and RPE/Bruch membrane band at either sides of the foveal pit are shown. After correction by Eq. (10), the large-scale intensity changes have been reduced, although the corrected curves in Fig 30 (c) exhibit a temporal increase in reflectivity of equal magnitude, probably due normalization for reduced reflectivity of the choriocapillaris. In Fig 30 (d), both normalization techniques are directly compared, where more high-frequency noise is apparent after RPE/OS layer normalization. The coefficient of variation after normalization by the proposed technique was 6.88% versus 9.94% after RPE/OS layer normalization, which indicates the benefit of the proposed noise-suppression technique. Previous studies on slow IOS have shown that visual stimuli can induce a slow reduction of fundus reflections that are indicative of hemodynamic activation.[309] However, because slow IOS typically onset several seconds after visual stimulation, which is well beyond the signal duration of reported fast IOS, their effect on this correction procedure is of limited significance. Inconsistent sampling of the same tissue volume may be an additional factor, since a rotation or shift of the eye, compensated by the tracker, will change the angle of incidence of the beam onto the retina. Both factors may have affected the estimation of illumination parameters. A solution is to employ volumetric imaging with orthogonal scan patterns to verify consistent recording of the same tissue volume, and alternatively, a bite-bar can be used to abolish bulk displacements of the eye.
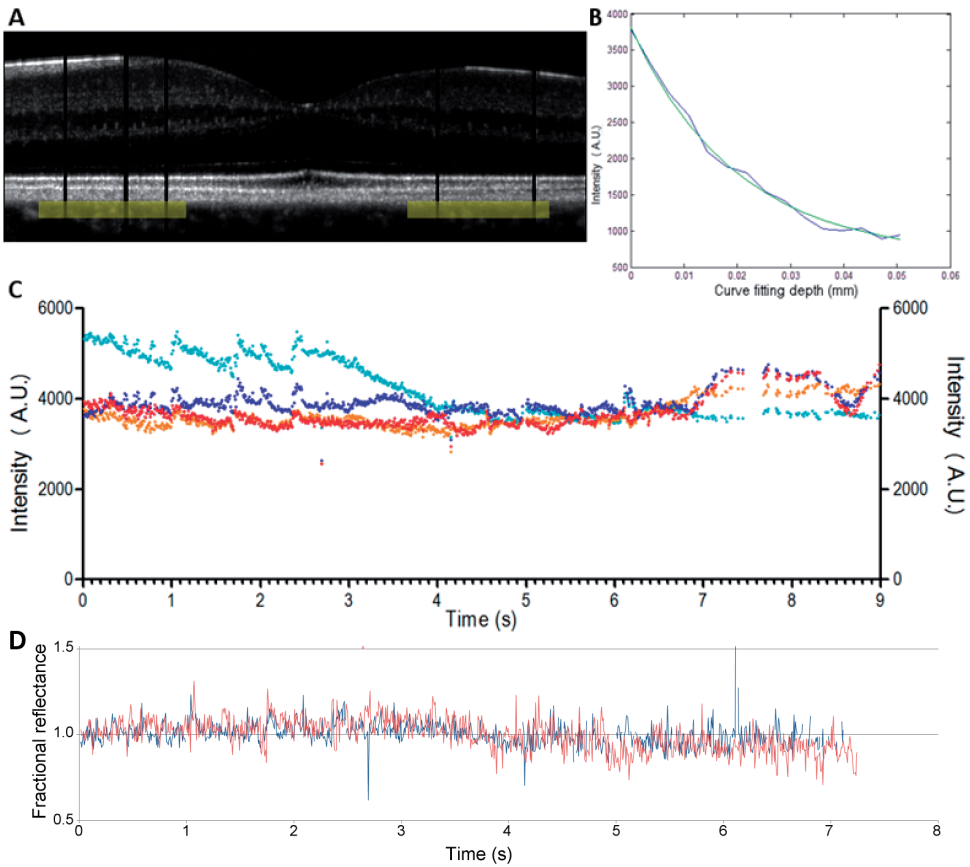
Fig 30. Compensation for variation in background illumination in timelapse OCT–recordings.
(a) Mean image of axially flattened B-scans (n = 400). 125 A-scans per choriocapillary bed, indicated in yellow, were averaged and used to estimate the illumination parameters (see text). Vessel shadows were blotted out (b) Example curve fit of reflectivity with depth using Eq. (9). Shown in blue is the intensity with depth after noise suppression by A-scan averaging. The fitted curve is shown in green. (c) Effect of compensation. The mean intensity of a region-of-interest, comprising the IS/OS-junction, OS/RPE and RPE bands of the same A-scans used for averaging in (a), was used as an indication of general reflectivity changes over time (light blue: left side, orange: right side). After normalization using Eq. (10) of the same regions of interest on the left side (blue) and the right side (red), the large-scale intensity variations caused by misalignments of the optical axes of OCT and the eye have been reduced. (d) Direct comparison of normalization for reflectivity in the RPE/OS layer (blue line) and of normalization by the proposed technique (red line).

Conclusions

In this study, we analyzed the literature for significant findings in IOS-imaging, and we analyzed methods to compensate for noise derived from different sources. This led us to propose a hypothesis of the biophysical underpinnings of the fluctuation-type and reflectivity change-type of fast IOS. The hypothesis incorporates light scattering changes due to the potential involvement of protein binding and PDE-activity, which have thus far not been considered. This involvement could be the cause of stimulus-evoked scattering boundaries within the outer segments of cones.[240, 241, 250, 253] Further, this involvement could explain the existence of reflections within the outer segment on OCT and the random pattern in which fast IOS occur (Fig 27),[273] although a differential polarity of fast IOS among rods and cones could serve as an alternative explanation. Important unresolved questions include 1) whether the fluctuation and non-fluctuation types of fast IOS reflect (some of) the same processes; 2) whether PDE-activity and osmotic swelling are principally responsible for the generation of both types; and 3) whether IOS generated by rods and cones are distinct in signal polarity.

We analyzed important sources of noise in SD-OCT IOS-imaging. While illumination artifacts and the optical Stiles-Crawford effect have received only minor attention earlier,[248] sensitivity fall-off and 1/f noise were in the focus.[154, 249, 251] Our data suggest that compensation for sensitivity fall-off suppresses noisiness in in-vivo IOS-imaging by SD-OCT. We found that normalization by the RPE-reflectivity inadequately compensates for illumination artifacts. An alternative approach, based on slope-fitting of optical attenuation though the choriocapillaris, was found more adequate. By effective suppression of these illumination artifacts, it facilitates comparisons of reflectivity between stimulated and unstimulated areas. Several lines of evidence suggest that the combination of lateral resolution and stability of retinal imaging are critical factors, which have been limited and so have prevented the acquisition of robust and reproducible IOS-measurements in awake humans by OCT. It is anticipated that with future improvements in hardware-based retinal trackers for high-speed AO-UHR-OCT setups,[282] implementation of trackers providing higher imaging stability,[283] and/or the application of appropriate registration methods,[84, 284] these issues can be resolved. Our analysis of the various causes of imaging noise indicates that significant fluctuations in photoreceptor reflectivity may be caused by sensitivity fall-off or variability in illumination even in highly cooperative and healthy subjects. Results from previous studies[297] suggest that cone reflectivity can be substantially affected by the OSCE. The application of bite-bars addresses these three issues, and is likely to adequately suppress this noise. For the clinical implementation of IOS-imaging, however, the complexity and costs of these setups must be significantly reduced. Also, customized bite-bars are impractical to use in daily clinical practice. The currently proposed algorithms can serve as a basis for dedicated correctional post-processing algorithms that are most likely needed in the absence of bite-bars. Alternative means to calibrate for the OSCE other than bite-bars, however, remain to be explored.
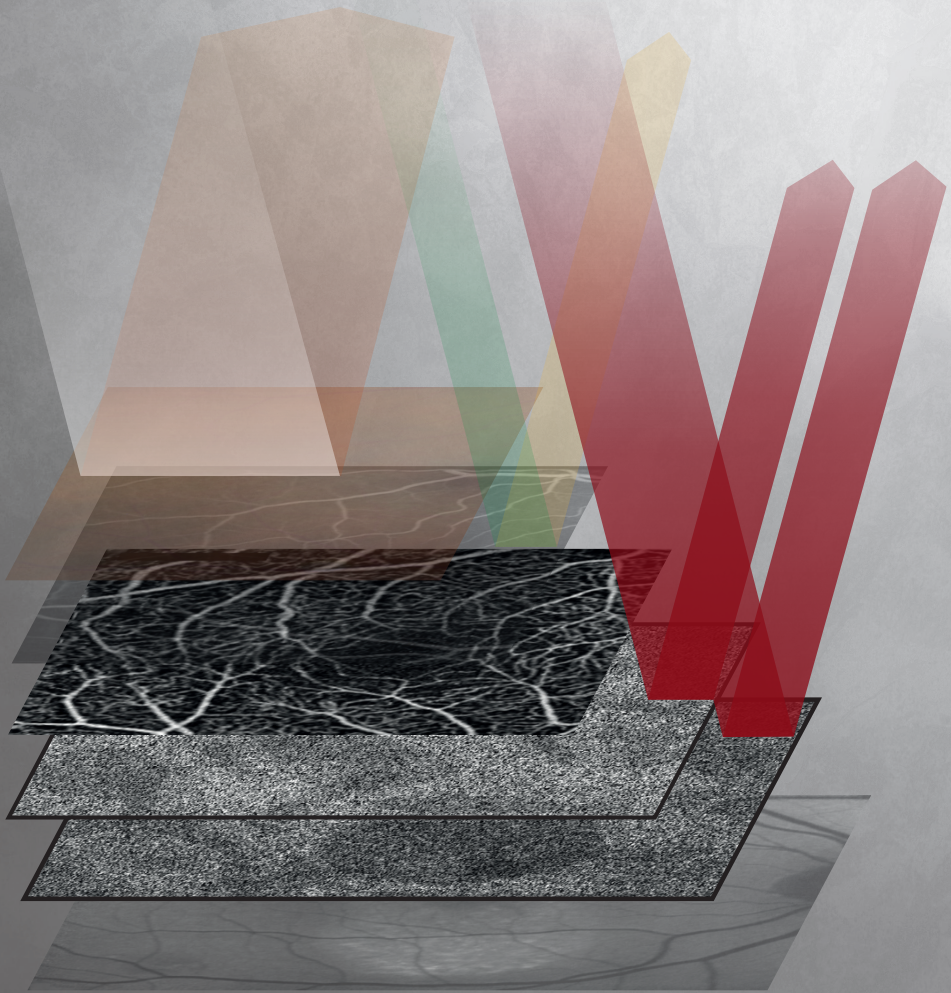
Chapter 3

Chapter 3.2

Optical coherence tomographic angiography compared to fluorescein and indocyanine green angiography in chronic central serous chorioretinopathy

Michel M. Teussink
Myrte B. Breukink
Mark J.J.P. van Grinsven
Carel B. Hoyng
B. Jeroen Klevering
Camiel J.F. Boon
Eiko K. de Jong
Thomas Theelen

Abstract

Purpose. Abnormal choroidal blood flow is considered important in the pathogenesis of chronic central serous chorioretinopathy (CSC). Optical coherence tomography (OCT) angiography can image ocular blood cell flow and could thus provide novel insights in disease mechanisms of CSC. We evaluated depth resolved flow in chronic CSC by OCT angiography compared to fluorescein angiography (FA) and indocyanine green angiography (ICGA).

Methods. Eighteen eyes with chronic CSC, and 6 healthy controls, were included. Two human observers annotated areas of staining, hypofluorescence and hot spots on FA and ICGA, and areas of abnormal flow on OCT angiography. Inter-observer agreement in annotating OCT angiography and FA/ICGA was measured by Jaccard indices (JIs). We assessed co-location of flow abnormalities and subretinal fluid visible on OCT, and the distance between hotspots on ICGA from flow abnormalities.

Results. Abnormal areas were most frequently annotated in late-phase ICGA and choriocapillary OCT angiography, with moderately high (median JI, 0.74) and moderate (median JI, 0.52) inter-observer agreement, respectively. Abnormalities on late-phase ICGA and FA co-located with those on OCT angiography. Aberrant choriocapillary OCT angiography presented as foci of reduced flow surrounded by hyperperfused areas. Hot spots on ICGA were located near hypoperfused spots on OCT angiography (mean distance, 168 µm). Areas with current or former subretinal fluid were co-located with flow abnormalities.

Conclusions. On OCT angiography, chronic CSC showed irregular choriocapillary flow patterns, corresponding to ICGA abnormalities. These results suggest focal choriocapillary ischemia with surrounding hyperperfusion that may lead to subretinal fluid leakage.

Introduction

Central serous chorioretinopathy (CSC) is characterized by a serous retinal detachment, sometimes accompanied by a detachment of the retinal pigment epithelium (RPE).[310-313] The leakage of fluid through the RPE often occurs at the macula, resulting in central vision loss, disturbed color vision, (para-) central scotoma, metamorphopsia and/or micropsia.[311, 313-315] Patients with CSC are typically male (male/female ratio 6:1), with an average age of 45 to 51 years.[310, 312] Besides the male gender, the most consistent risk factor appears to be the use of corticosteroids, as well as circumstances where corticosteroid levels are increased, such as Cushing disease and pregnancy. In addition, a type A personality and certain genetic factors may increase the risk for CSC.[310, 316, 317] Although the precise pathophysiological mechanism is still unclear, multimodal imaging indicates that subretinal fluid (SRF) accumulation in CSC results from a thickened, congested, hyperpermeable choroid leaking fluid through a dysfunctional RPE.[318-321]

Two main forms of CSC can be distinguished: the acute and chronic form.[310, 312, 313, 320] Patients with acute CSC usually present with sudden and marked central vision loss, caused by SRF leakage at the macula due to a focal leak in the RPE that is visible on fluorescein angiography (FA).[310, 311, 322] The prognosis is favorable in this type and spontaneous recovery is often seen within 2-3 months.[310] In contrast to acute CSC, chronic CSC is typically not self-limiting and SRF persists for more than 3 months. Patients with chronic CSC have more diffuse multifocal leakage on FA and indocyanine green angiography (ICGA), as well as irregularly distributed widespread RPE changes associated with various degrees of low-grade, more distinct leakage on angiography: diffuse retinal pigment epitheliopathy (DRPE). Such persistent serous neuroretinal detachments may cause progressive and irreversible photoreceptor damage, resulting in a far worse visual prognosis of chronic CSC as compared to the acute form.[311, 323, 324]

Previous studies have examined blood flow in CSC by use of FA/ICGA imaging, and observed choriocapillary congestion.[319] In an ultrastructural study of a cynomolgus monkey model of CSC, damage of choriocapillary endothelial cells underneath damaged RPE cells that were covered by fibrin platelet clots was observed, which led to the suggestion that choriocapillary hyperpermeability occurs in CSC.[325, 326] Blood flow in CSC has also been examined using other optical imaging modalities. For instance, choroidal hypoperfusion was demonstrated with laser Doppler flowmetry.[327]

Spectral-domain optical coherence tomography (SD-OCT) is a noninvasive, high-speed, high-resolution, three dimensional imaging technique frequently applied in patients with CSC to evaluate SRF and photoreceptor damage.[328] SD-OCT may also be used to perform angiography in a non-invasive manner. Split-spectrum amplitude decorrelation angiography

(SSADA) is a clinically feasible, commercialized technique which can visualize capillary blood flow, but without determination of the flow direction.[96] In contrast to dye assisted FA and ICGA imaging, OCT angiography detects movements of blood cells, instead of serum extravasation or staining of vessel walls and tissue. SSADA has been used recently in the examination of abnormal vascular structures in macular telangiectasia type 2,[329] and of choroidal neovascularization in age-related macular degeneration,[330, 331] as well as chronic CSC.[332] Hence, OCT angiography could provide additional information on the blood supply in CSC, and it could therefore help to better understand the underlying pathophysiology of the disease. In our current study we compared OCT angiography in chronic CSC to established angiographic imaging modalities like FA and ICGA.

Methods

We studied 18 eyes of 11 consecutive patients (6 male, 5 female) with chronic CSC seen at the outpatient clinic of the Department of Ophthalmology of the Radboud University Medical Center (Nijmegen, the Netherlands) from November, 2014 to January 2015. All study participants gave oral informed consent for OCT based angiography imaging. In addition, 6 healthy volunteers (3 male, 3 female) with no medical history of ocular or cardiovascular diseases and/or diabetes mellitus served as controls. Ethical approval for retrospective analysis of this observational case series was granted by the institutional review board at the Radboud University Medical Center and the study adhered to the tenets of the Declaration of Helsinki. The diagnosis of chronic CSC was based on a history with persistent fluid of at least 3 months, as well as RPE damage (DRPE) due to longstanding SRF. Active chronic CSC was defined by active leakage of fluid under the neuroretina confirmed by SD-OCT and by hyperfluorescent spots on ICGA and/or at least one ill-defined leakage spot on FA. Patients were included if OCT angiography, FA and ICGA were performed on the same day to maximize the comparability of the angiographic techniques. Patients with other ocular disorders commonly associated with serous SRF, such as choroidal neovascularization, polypoidal choroidal vasculopathy, diabetic retinopathy, retinal vascular occlusion, and myopia > 6 diopters were not eligible.

For SD-OCT, fundus autofluorescence (AF), FA and ICGA imaging, we used the Spectralis™ HRA+OCT device (Heidelberg Engineering, Heidelberg, Germany). Simultaneous FA and ICGA imaging were performed after patients were given a 2.5 ml intravenous injection of 25% fluorescein solution mixed with 12.5 mg indocyanine green (ICG-Pulsion® 25 mg). FA and accompanying ICGA images were selected from the early phase (30 to 60 seconds post-injection) and the late phase (6 to 8 minutes post-injection) of the dye transit. Following ICGA/FA imaging, the presence of sub-macular fluid deposits was evaluated based on SD-OCT.

OCT angiography

We used a newly developed SD-OCT device (OptoVue RTVue XR Avanti™ AngioVue™, Optovue Inc, Fremont, CA) to obtain SSADA images. This instrument has an A-scan rate of 70 kHz and an axial resolution in tissue of 5 μm, using a light source with a center wavelength of 840 nm and a spectral bandwidth of 45 nm. Two consecutive B-scans (M-B frames) of 304 A-scans each along the fast scanning axis were recorded at each of the 304 positions along the slow scanning axis. According to this protocol, horizontal priority fast transverse (x-fast) scans and vertical priority fast transverse (y-fast) scans were obtained consecutively to record a 3-dimensional data cube. The M-B frames were analyzed for highly decorrelated pixels, which are co-located with moving blood cells in retinal and choroidal vessels. These data were used to reconstruct three-dimensional blood flow images as described previously.[96] Scans with insufficient quality due to blinking (appearing as straight, black stripes), or fixation loss were excluded. After selecting the best scans, residual axial and saccadic motion artifacts were corrected using the contained software (ReVue™, Optovue Inc.). OCT angiography images of four vascular layers (inner vascular plexus, deep retinal vascular plexus, outer retina, and choriocapillaris), and a full thickness OCT angiogram including all retinal layers and the choriocapillaris, were then exported. Examples of these images in a healthy control subject and a patient with chronic CSC are depicted in Fig 31.
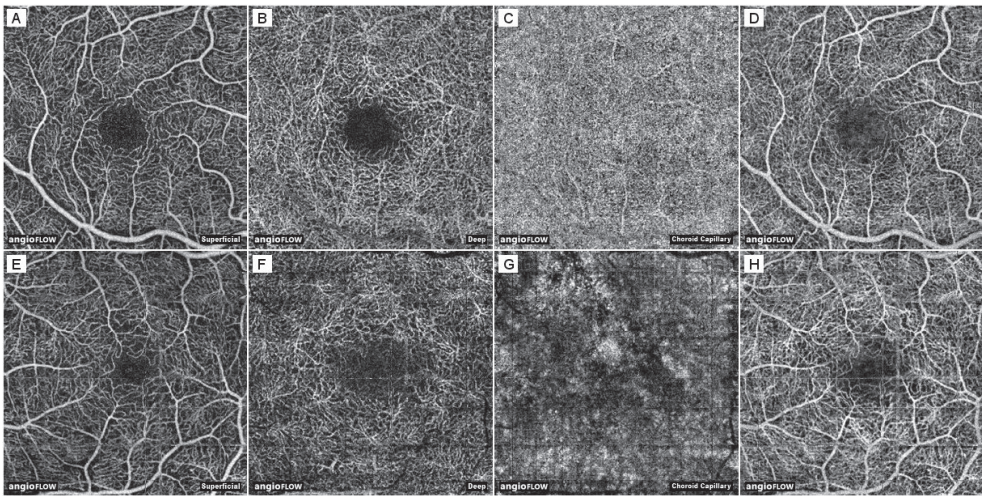
Figure 31. OCT angiography of a healthy subject and of a patient with chronic CSC. A-D, Right eye of a healthy 25 year-old female, E-H, Left eye of a patient with chronic CSC (patient 4, see Table 5). A and E, The inner vascular plexus ('Superficial'). B and F, The deep retinal vascular plexus ('Deep'). C and G, Choriocapillaris ('Choroid cap'). The choriocapillaris was defined as a 20 µm band below the RPE-Bruch's membrane complex. It was segmented by the ReVue software and, if needed, corrected for significant segmentation errors. D and H, Full-thickness OCT angiogram. Outer retina not shown.

Image readings and annotations

OCT angiography images and FA/ ICGA images were aligned using a semi-automatic registration tool, developed in MeVisLab (version 2.5a, MeVis Medical Solutions AG, Bremen, Germany), that translates, rotates, and rescales the target image to accurately match three user specified landmark locations on both the source (FA) and target (OCT angiography of the superficial layer) images.[157] The same transformation matrix was applied to ICGA images for co-registration.

All image readings were performed at NANOREAD (Nijmegen Angio OCT Reading Center) by experienced and masked observers, and were done separately on the same computer. Each observer (author M.B. & T.T.) annotated areas showing leakage and hypofluorescence in the FA and ICGA images and regions in the OCT angiography images with visually evident deviations from the normal appearance. In Fig 32, the image registration and annotation processes are depicted in a flow chart together with illustrative examples. A representative example of registered images is shown in Fig 33. OCT angiography images of five healthy volunteers, who were not part of the study, served as a reference. Images of patients and controls were anonymized and randomized, by replacing filenames with unique random numbers and subsequent sequential rearrangement according to consecutive numbering. The region-of-interest (ROI) function of ImageJ (version 1.46r, National Institutes of Health, Bethesda, MD) was used for annotation purposes.

Image analysis

To determine the inter-observer agreement of image annotations, the number of images annotated by both observers was determined. In case both observers annotated the image, we calculated the spatial overlap of the annotations by the Jaccard index (Jl) as:

$$JI(R_1, R_2) = \frac{R_1 \text{ pixels} \cap R_2 \text{ pixels}}{R_1 \text{ pixels} \cup R_2 \text{ pixels}}$$

Indices were calculated separately for each observer's set of annotations, and were then pooled together. The spatial correspondence of abnormalities visible in OCT angiography images with FA/ICGA was firstly determined by the frequency of annotations on both modalities. In those cases, we calculated JIs to determine the extent of their overlap. We tested if the overlap of each combination of OCT angiography images and FA/ICGA images was different from all other combinations with the Mann-Whitney *U*-test. We also tested if this overlap, in terms of JIs, was correlated between both eyes of a patient. *P* - values < 0.05 were considered statistically significant.
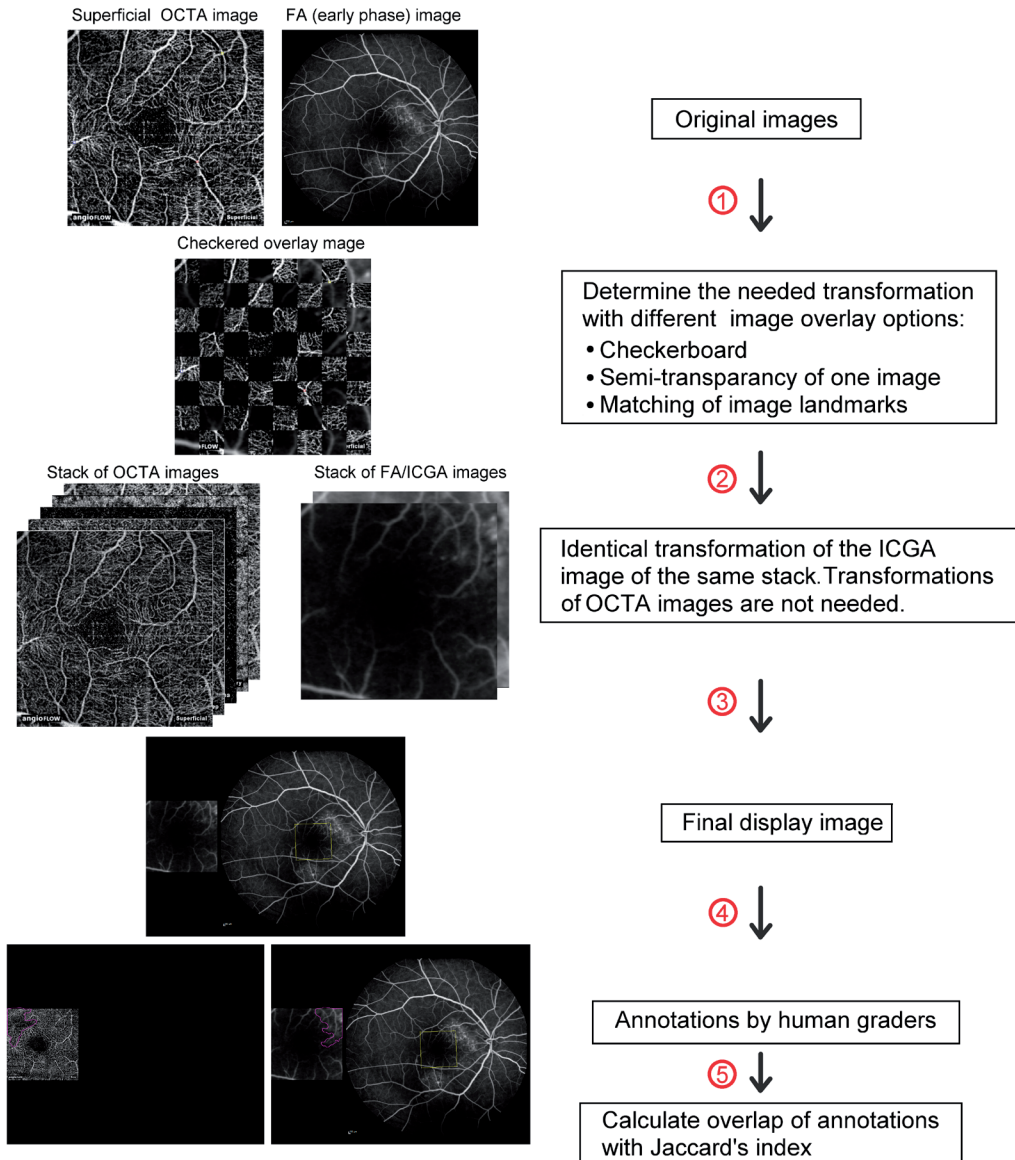
Figure 32. Flow chart of the image registration and annotation procedures. Original images, *i.e.* superficial retinal OCT angiography and FA images, were registered by an observer, using a variety of image overlay options (*Step 1*). Simultaneously acquired ICGA images were transformed identically to the FA image (*Step 2*). The final display image, with a standard layout, was then created, which included the original FA/ICGA image containing contextual information (*Step 3*). Annotations were made by human observers (*Step 4*), after which the overlap of annotations was calculated by Jaccard's index (*Step 5*). See text for details.
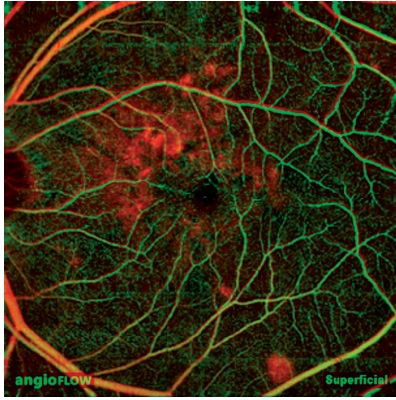
Figure 33. Example of image registration. Overlay of an early-phase FA image (red) registered to a superficial OCT angiography image (green), with overlapping vessels indicated in yellow.

Image analysis was performed to determine the correspondence between hot spots or profound hypofluorescence in late-phase ICGA images, and focal areas of decreased flow in the choriocapillary lamina on OCT angiography images, in terms of the distance between their centers. These centers were determined by the center of mass of the annotated areas. In case adjacent foci appeared confluent on ICGA images, they were often amalgamated in a single ROI as 'beads on a string'. A watershed algorithm was applied to split these ROI's to facilitate the distinction of different foci. Subsequently, the shortest distances between leakage hot spots or hypofluorescent foci in ICGA images and dark spots in OCT angiography images with a visually evident correspondence were calculated (Fig 34).
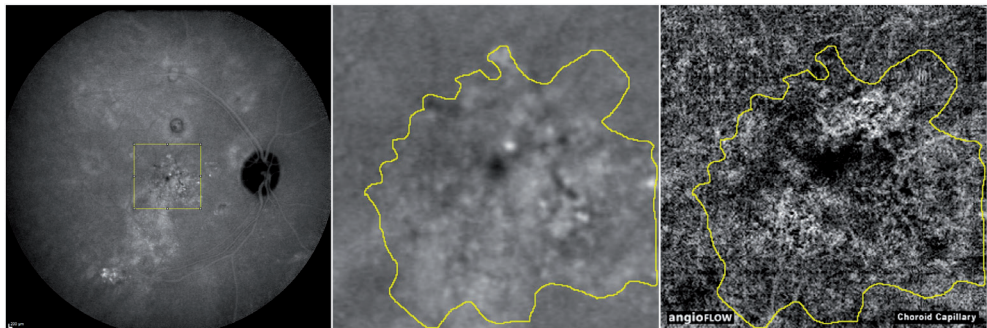
Figure 34. Annotation and quantitative analysis of hyperfluorescent areas on ICGA and aberrant flow on OCT angiography. Left image, late-phase ICGA image of a patient with chronic CSC with location of the registered image (yellow frame). Middle image, detail of abnormalities in the registered ICGA image. Right image, the aberrant flow pattern on OCT angiography of the choriocapillaris is co-located with the annotated region on late-phase ICGA; the darkest region corresponds with a hypofluorescent spot on ICGA, bordered by increased flow co-located to the leakage hotspot and late staining. The annotated region is depicted by the yellow line.

Fundus autofluorescence

To determine whether the results of OCT angiography of the choriocapillaris were affected by light-absorbing chromophores of the RPE, we compared OCT angiography images to AF images that were recorded on the same day. AF images were registered to OCT angiography images as described earlier. We considered OCT angiography signals above or below the mean ± 2 standard deviations of apparently uninvolved areas, respectively, as abnormal choriocapillary flow. Uninvolved areas were determined by a lack of annotations, absence of large vessel shadows, and in the near vicinity of the image border, as irregular flow at the image borders was common even in healthy subjects. Thresholded pixels of increased or decreased flow were overlaid on the registered AF images. Finally, two observers (M.T., T.T.) evaluated whether there was any co-location of focally changed AF signals and choriocapillary flow.

Results

Patient demographics are depicted in Table 5.

Table 5. Clinical characteristics of the patients included in this study

ID/Gender /Age, y	Eye(s) Included	Signs of Chronic CSC on FA, ICGA and OCT	Active Chronic CSC on FA, ICGA and OCT	Previous Treatment(s)
P1/F/55	OD	yes	yes	1 x MP
P2/M/58	OD	yes	yes	NA
P3/F/64	OD	yes	yes	NA
	OS	yes	yes	NA
P4/M/40	OD	yes	no	NA
	OS	yes	yes	NA
P5/M/71	OD	yes	no	2 x PDT
P6/F/56	OD	yes	yes	NA
P7/F/38	OD	yes	no	NA
	OS	yes	yes	1 x PDT
P8/F/56	OD	yes	no	1 x MP
	OS	yes	yes	NA
P9/M/59	OD	yes	yes	2 x MP, 1 x PDT
	OS	no	no	NA
P10/M/62	OD	no	no	NA
	OS	yes	yes	NA
P11/M/47	OD	yes	yes	NA
	OS	yes	no	2 x MP, 1 x PDT

CSC: central serous chorioretinopathy; FA: fluorescein angiography; F: female; ICGA: indocyanine green angiography; M: male; MP: micropulse laser therapy; NA: not applicable; OCT: optical coherence tomography; OD: right eye; OS: left eye; PDT: half-dose photodynamic therapy.

Inter-observer agreement

A total of 255 images were analyzed, including 100 FA and ICGA-images of patients, and 125 and 30 OCT angiography images of patients and healthy subjects, respectively. In 132 images (52%), abnormalities were annotated by both observers (83 FA/ICGA images and 49 OCT angiography images). An example of image annotations by both observers is shown in Fig 35. The corresponding JIs as indicators of inter-observer agreement and numbers of annotated images are summarized in Table 6. FA and ICGA images were annotated with moderate agreement (median JIs, 0.43-0.67). Of the various OCT angiography images, choriocapillary flow images were most frequently annotated by both observers (80% of the patient images, 17% of the control images) with moderate inter-observer agreement (median JI, 0.52). OCT angiography images of retinal layers were annotated less often than choriocapillary flow images. The inter-observer agreement in annotating abnormal choriocapillary flow was similar to FA and ICGA, both in terms of the frequency of annotations and the agreement scores.

Table 6. Inter–observer agreement of annotated vascular abnormalities in FA, ICGA and OCT angiography images

FA/ICGA	JI		Annotations made by observers		
	Mean (SD)	Median	Both	Either	None
FA (early phase)	0.46 (0.29)	0.35	19	1	5
FA (late phase)	0.59 (0.23)	0.58	20	2	3
ICGA (early phase)	0.43 (0.29)	0.47	22	1	2
ICGA (late phase)	0.67 (0.15)	0.74	22	2	1
OCT angiography					
Superficial	0.28 (0.22)	0.28	4	9	18
Deep	0.27 (0.19)	0.26	11	10	10
Outer retina	0.47 (0.17)	0.40	7	16	8
Choroid cap	0.49 (0.22)	0.52	21	5	5
FT-OCTA	0.5 (0.2)	0.53	6	11	14

JI: Jaccard index; FA: fluorescein angiography; ICGA: indocyanine green angiography;
FT-OCTA: full thickness OCT angiogram; OCT: optical coherence tomography; SD: standard deviation.
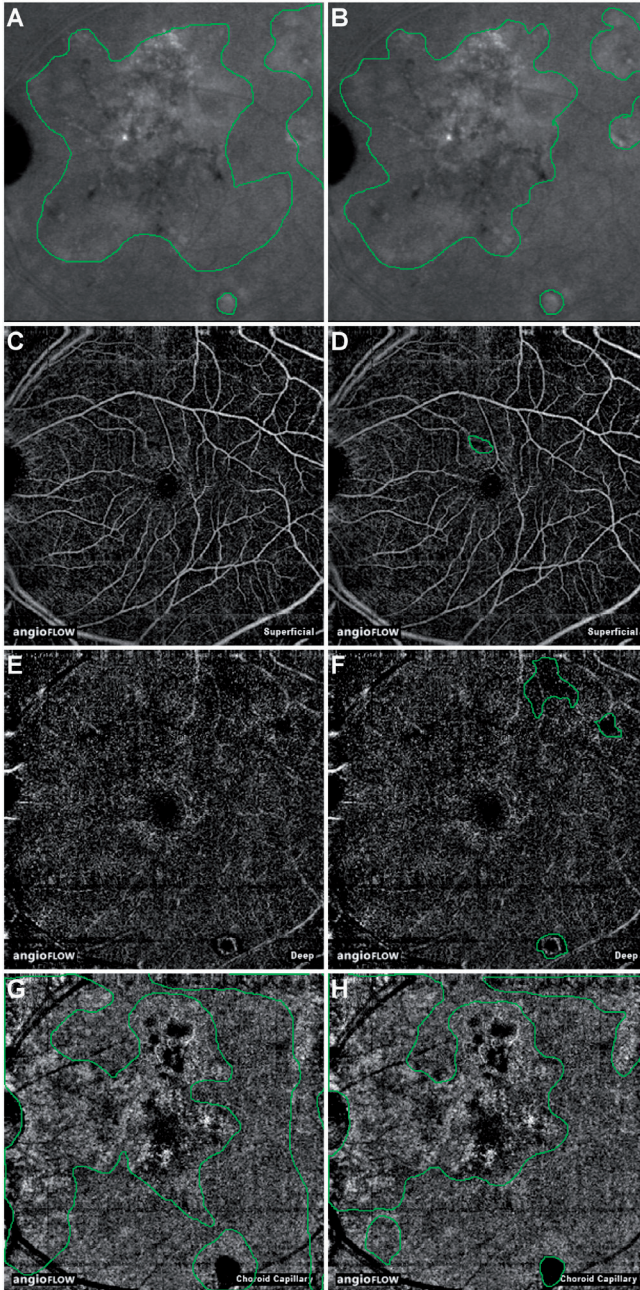
Figure 35. Examples of image annotations. A and B, late-phase ICGA images (left eye of patient 8, 6x6 mm). C and D, superficial OCT angiography images. E and F, deep OCT angiography images. G and H, choriocapillary OCT angiography images. Left column, annotations by observer 1; right column, annotations by observer 2. The Jaccard indices (JIs) of overlap between late-phase ICGA and superficial- and deep- OCT angiography were 0.006 and 0.022, respectively (observer 2). The JIs of overlap of late-phase ICGA with choriocapillary OCT angiography were 0.43 and 0.55 for observers 1 and 2, respectively.

Chapter 3

General correspondence between OCT angiography and FA/ICGA
Table 7 summarizes the overlap of annotated abnormal areas observed with various angiographic imaging modalities expressed in JIs. Choriocapillary flow images and late-phase FA/ICGA images corresponded best in determining abnormality with moderately low overlap of the annotated areas (median JI of both FA and ICGA vs. choriocapillary, 0.41). In general, there was a poor overlap between annotated changes on FA and OCT angiography images, with median JIs ranging from 0 to 0.05. The correspondence between aberrant choriocapillary flow and abnormalities on late-phase FA/ICGA was higher than the correspondence of abnormalities in early or late FA images and abnormalities in retinal OCT angiography images ($P < 0.001$). In general, the JIs showed a significant correlation between both eyes (Spearman's $\rho = 0.59$, $P = 4.5 \cdot 10^{-7}$).

The annotated choriocapillary flow patterns had a highly variable appearance. In some cases, we observed mottled flow patterns with patches of increased and decreased flow. Mostly, however, we observed irregular patterns with large and semi-confluent patches of decreased flow adjacent to similar patches with increased flow. A small number of patches with decreased choriocapillary flow corresponded with RPE-detachments visible on SD-OCT. Several other patches corresponded with focal areas of a thickened RPE below a SRF pocket, which appeared to produce shadow artifacts on late phase ICGA. In general, light-absorbing fluorophores in the RPE, as visualized by AF imaging, had no apparent correspondence with the appearance of choriocapillary flow on OCT angiography of CSC. A few sporadic hyper-AF areas corresponded with decreased flow areas, although not all hyper-AF in the same images corresponded with decreased flow and vice-versa. The same was true for the correspondence between hypo-AF and increased flow, and for other combinations. Areas of aberrant choriocapillary flow were generally co-located with locations of current SRF accumulation visible on SD-OCT, or with locations where SRF had resolved. The aberrant flow patterns appeared similarly heterogeneous in treatment naive patients and treated subjects, with no consistent differences in eyes that received micropulse laser treatment or photodynamic therapy.

Correspondence between hot spots on ICGA and aberrant choriocapillary flow
We also studied the relationship between decreased choriocapillary flow and hot spots or hypofluorescence on ICGA (Fig 34). In most areas with decreased flow on OCT angiography we were unable to observe a corresponding, well-defined focus of abnormal fluorescence on late phase ICGA (75 out of 117 areas, or 64.1%). The remaining areas with decreased flow, however, overlapped largely with hypofuorescent areas on ICGA. Twelve (29.3%) out of 41 leakage areas and hot spots on late phase ICGA appeared to be connected with areas of decreased choriocapillary flow on OCT angiography, versus 24 (42.9%) out of 56 hypofluorescent spots on late phase ICGA. The mean distance between hot spots on ICGA and matched areas with decreased signal in choriocapillary flow images on OCT angiography

was 168 μm (SD, 133 μm), or 17 pixels. The mean distance of hypofluorescent spots was 133 μm (SD, 70 μm), or 13 pixels. Areas of increased flow, however, were often found adjacent to leakage hot spots on ICGA. For choriocapillary flow images and corresponding FA/ICGA and AF images of all included patients and controls, see the Appendix.

Table 7. Overlap of image annotations on FA/ICGA and OCT angiography in 11 patients with chronic CSC

FA/ ICGA	OCT angiography	Mean JI (SD)	Median
FA (early phase)	Superficial	0.04 (0.1)	0
	Deep	0.06 (0.1)	0.01
	Choroid cap	0.25 (0.21)	0.22
	FT-OCTA	0.1 (0.19)	0
FA (late phase)	Superficial	0.03 (0.06)	0
	Deep	0.09 (0.14)	0.02
	Choroid cap	0.38 (0.22)	0.41
	FT-OCTA	0.11 (0.15)	0.05
ICGA (early phase)	Superficial	0.12 (0.2)	0
	Deep	0.09 (0.12)	0.04
	Choroid cap	0.27 (0.18)	0.24
	FT-OCTA	0.1 (0.15)	0.05
ICGA (late phase)	Superficial	0.04 (0.06)	0
	Deep	0.08 (0.11)	0.05
	Choroid cap	0.41 (0.19)	0.41
	FT-OCTA	0.14 (0.2)	0.05

Choroid cap: choriocapillaris; CSC: central serous chorioretinopathy; JI: Jaccard index; FA: fluorescein angiography; ICGA: indocyanine green angiography; FT-OCTA: full thickness OCT angiogram; OCT: optical coherence tomography; SD: standard deviation.

Chapter 3

Discussion

In this study, we compared OCT angiography characteristics of patients with chronic CSC to FA and ICGA findings. We found typical changes in the choriocapillary flow pattern of chronic CSC patients, which corresponded to areas affected by subretinal fluid accumulation. There was moderate inter-observer agreement on changes in choriocapillary flow images of CSC patients, and there was moderate spatial correspondence between late FA/ICGA and choriocapillary flow images.

Kitaya *et al.* (2003) used laser Doppler flowmetry to show that eyes with CSC had reduced choroidal blood flow relative to the unaffected fellow eye.[327] Using combined FA/ICGA imaging, Scheider *et al.* (1993) also confirmed the reduction in choroidal blood flow in CSC and demonstrated that the hypoperfusion persisted after clinical improvement.[333] In our study, changes of the choriocapillary flow pattern on OCT angiography appeared as focally increased and decreased pixel values, indicating coexisting increased and decreased flow, respectively. Even though, the appearance of these changes was significantly different from the fairly homogeneous appearance of the healthy choriocapillary layer, there was only a moderate inter-observer agreement. Obviously, the border between the appearance of healthy and affected tissue in OCT angiography may not easily been drawn between observers. This phenomenon has been observed earlier in a study that evaluated the agreement among highly experienced retinal specialists in grading of FA images for the presence of active choroidal neovascularization.[334] A multimodal approach in angiographic techniques may help to improve the identification of pathological changes. One has to keep in mind, however, that OCT angiography measures blood flow dependent on intravascular cell movements, while FA/ICGA images the flow of blood plasma, independent of cell movement. Therefore, these three techniques give blood flow information that is supplementary to each other.

On OCT angiography, we observed choriocapillary hypoperfusion with hyperperfusion in the surrounding area. This is consistent with results of earlier studies, showing focal filling defects in the choriocapillaris with dilated and tortuous feeding arterioles and dilated venules.[319, 335-337] These filling defects may be caused by capillary congestion and/or rarefaction.[319] Areas of irregular choriocapillary texture on OCT angiography partially co-located to areas with late staining on ICGA. Also, many hot spots on late-phase ICGA, if present, were in close proximity of relative ischemia on OCT angiography within those areas of irregular texture. Taken together, these data suggest that reduced blood perfusion in the choriocapillaris may be surrounded by reactive hyperperfusion. Hyperperfusion leads to increased hydrostatic pressure within the fenestrated choriocapillaris. Together with chronic hypoxic damage, this may lead to disintegrity of the continuity of the RPE,[338] and to subretinal fluid leakage with serous neuroretinal detachment in chronic CSC.[339, 340]

According to our data, the abnormal vascular situation in the choriocapillary layer appeared to persist even after resolution of SRF and seemed to be independent of any kind of treatment. It is still unclear, why different treatment modalities may lead to successful fluid resorption. The mechanism of action of photodynamic therapy has been postulated to include short-term choriocapillary hypoperfusion and long-term choroidal vascular remodeling with subsequent reduction of vascular hyperpermeability and leakage.[328, 341, 342] On the short term, the hypoperfusion may lead to more ischemic RPE damage. Because of the long time period between photodynamic therapy and our study measurements, we may have missed any therapeutic effects visible on OCT angiography. It may be useful to prospectively follow patients after photodynamic therapy by OCT angiography to learn more about the therapeutic mechanism of this treatment. Subthreshold micropulse diode lase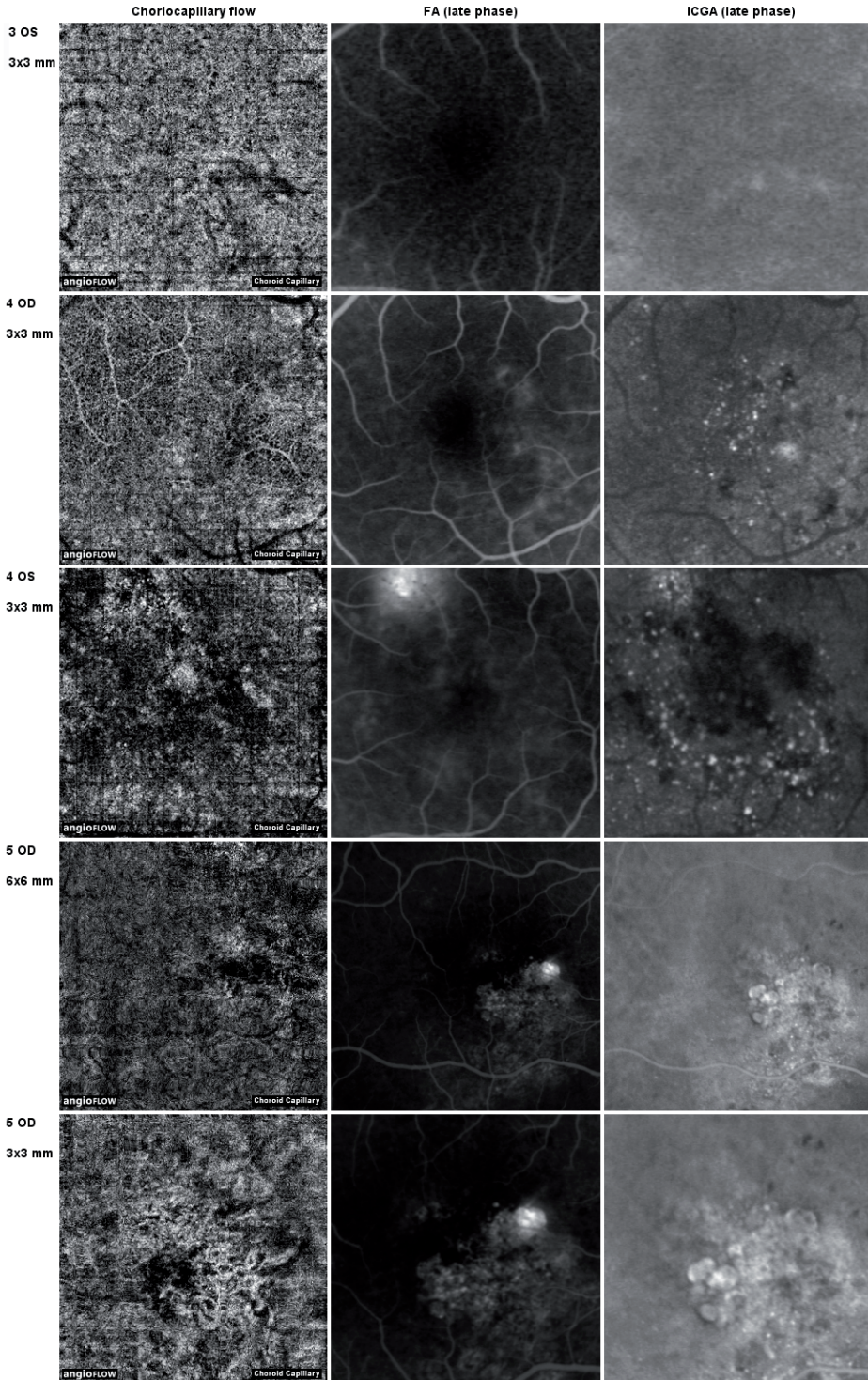r treatment is applied in an attempt to trigger the regeneration of the RPE and a long-term metabolic increase at the chorioretinal junction,[343] which may increase SRF resorption by the RPE.[344] Micropulse laser treatment is not thought to affect the choriocapillaris directly. The lack of effects on choriocapillary flow in patients after micropulse laser treatment is therefore not surprising.

Our study is mainly limited by the small number of patients and the retrospective and cross-sectional data acquisition. As a consequence, we have studied a combination of treatment-naive patients and patients who were previously treated by micropulse laser or photodynamic therapy once or multiple times. We do not have pre-treatment data and we did not monitor patients over time. To further improve our knowledge of the vascular changes in chronic CSC, prospective and longitudinal studies are required to monitor vascular changes during the natural course and during different treatment strategies. Although we found no consistent effects of chromophores in the RPE on the appearance of choriocapillary flow, save for a few sporadic cases, a comprehensive analysis of potential confounders on the appearance of OCT angiography signals was out of the scope of this study. This is important in OCT angiography studies of retinal diseases in which layers with high light-absorption are affected. Therefore, future studies should include SD-OCT and AF imaging to determine potential imaging artifacts. The fields of view on OCT angiography were of considerably smaller size than those currently used in ICGA or SD-OCT. Peripheral areas with obvious FA/ICGA irregularities were therefore missed. Future studies should aim to include the complete posterior pole with all angiographic abnormalities by OCT angiography scanning. This could be achieved by a montage of many high-resolution OCT angiography scans or by improved OCT hardware-software combinations capable to visualize larger fundus areas with high resolution.

In conclusion, OCT angiography showed significant textural changes of the choriocapillary flow pattern in chronic CSC patients. Our results suggest foci of ischemia surrounded by reactive choroidal hyperperfusion as an important factor in the pathogenesis of chronic CSC. Prospective OCT angiography studies on chronic CSC are needed to better understand the pathogenesis and treatment response of this visually threatening disease.

Chapter 3

Appendix

	Choriocapillary flow	FA (late phase)	ICGA (late phase)

1 OD
6x6 mm

2 OD
6x6 mm

2 OD
3x3 mm

3 OD
6x6 mm

3 OD
3x3 mm

| Choriocapillary flow | FA (late phase) | ICGA (late phase) |

3 OS

3x3 mm

4 OD

3x3 mm

4 OS

3x3 mm

5 OD

6x6 mm

5 OD

3x3 mm

| | Choriocapillary flow | FA (late phase) | ICGA (late phase) |

6 OD
6x6 mm

7 OD
6x6 mm

7 OD
3x3 mm

7 OS
6x6 mm

7 OS
3x3 mm

	Choriocapillary flow	FA (late phase)	ICGA (late phase)

8 OD

3x3 mm

8 OS

6x6 mm

8 OS

3x3 mm

9 OD

3x3 mm

9 OS

3x3 mm

Chapter 3

Choriocapillary flow	FA (late phase)	ICGA (late phase)

10 OD
3x3 mm

10 OS
6x6 mm

10 OS
3x3 mm

11 OD
3x3 mm

11 OS
3x3 mm

C1 (OS) 3x3 mm **C2 (OD) 3x3 mm** **C3 (OD) 3x3 mm**
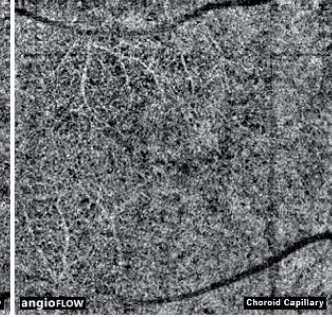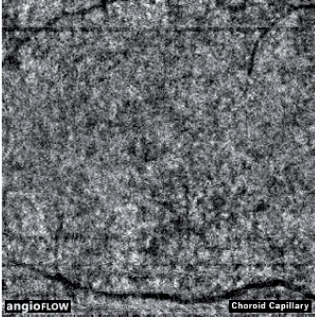
C4 (OD) 3x3 mm **C5 (OD) 6x6 mm** **C6 (OD) 3x3 mm**
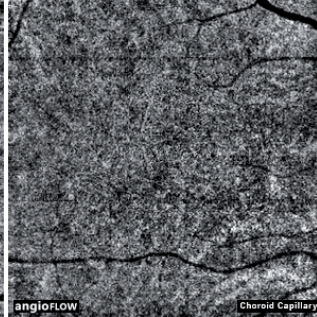
Chapter 3

Chapter 4.

General discussion

In this thesis, we investigated a variety of retinal imaging biomarkers and their correlation with retinal disease progression. The introduction of high-resolution imaging techniques such as cSLO and OCT has increased our insight in the development and progression of retinal pathology, such as choroidal neovascularization, macular edema, and diseases affecting the photoreceptors or the RPE. Recently, researchers have also investigated more subtle alterations in these retinal images and their correlation with disease progression. The earliest signs of retinal pathology may be difficult or even impossible to detect with the naked eye, and therefore may require computer-aided image analysis. Detection of these early signs may be critical to start therapeutic interventions as soon as possible, before irreversible loss of visual function occurs. In this thesis we used cSLO and OCT to discover, and to advance our knowledge of, signs of retinal function and pathology. In the following sections, we elaborate on our studies of such signs, associations with the development and progression of retinal diseases, and we identify possible directions for future research.

Quantitative analysis of fundus autofluorescence

Three investigations were conducted mainly by autofluorescence (AF) imaging. First, we used this technique to study the effects of long-term protection from daylight on the disease course of STGD1. We chose a method that allows for the quantification of focal AF abnormalities relative to the surrounding area[116, 124, 345, 346] in a highly observer-independent m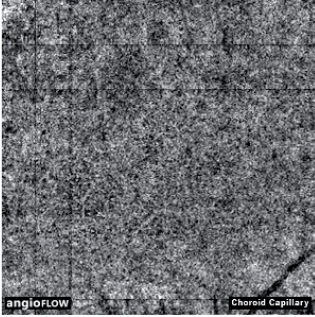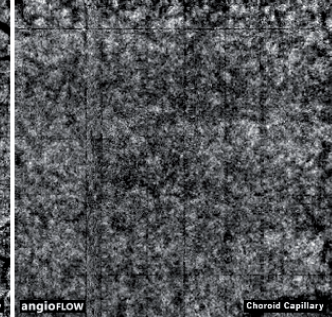anner. Because of the absence of geographic atrophy as a clinical endpoint[57] in our study patients, we measured more subtle AF changes as imaging biomarkers of disease progression. Age-related macular degeneration is a disease in which photodegradation of lipofuscin bisretinoids is causally linked just as in STGD1.[26] However, population-based studies have shown contradictory results regarding the causal role of light exposure in the pathogenesis of AMD.[347-349] It should be borne in mind that assessing retinal exposure to sunlight based on patients' recollection of their habits with respect to protecting their eyes from sunlight over a whole life is a difficult task.[350] In contrast, our study provides a rare opportunity to study light as a risk factor for the progression of STGD1 under relatively well-controlled conditions.

Recent studies found that older *Abca4*^{-/-} mice with greater accumulations of RPE lipofuscin also exhibit greater photoreceptor atrophy after light exposure.[125] Light deprivation may therefore be especially relevant for the 86%[135] of patients with abnormally high fundus AF. As described in chapter 2.3, higher AF correlates with proportionally greater light absorption by lipofuscin. This subgroup of patients may therefore be at an elevated risk for lipofuscin photooxidation that could lead to progressive RPE dysfunction. These mouse studies also showed that with *Abca4*^{-/-}-associated disease progression, photoreceptor atrophy can occur by light-independent mechanisms.[125] This suggests that patients with advanced STGD1 may develop photoreceptor atrophy regardless of light-deprivation therapy, and therefore stand to gain less benefit.

Despite the projected benefits, the clinical feasibility of ≥90% occlusive sunlenses as a treatment modality is highly questionable. Patients generally reported great discomfort when wearing them—although, as mentioned in Chapter 2.1, patient compliance was high. If reduction of photo-oxidative modifications to lipofuscin bisretinoids led to our observations, then attenuation of short-wavelength visible light is likely an equally efficacious[125, 138, 351] yet clinically more feasible alternative. Our simulation on the wavelength dependence of this photo-oxidative stress (Chapter 2.3, Fig 24) indicates that a long-pass filter at $\lambda \geq 500$ nm already prevents most of the photo-oxidative stress in the RPE of these patients. In addition, long-term monocular light deprivation, alternating between both eyes at regular intervals, might have adverse effects in adults. To my knowledge, no research has been done on the maintenance of circadian rhythms under monocular deprivation. Also, long term light deprivation was suspected to cause cones to lose their orientation to the pupil center, however this hypothesis could not be proven.[352, 353] Whether or not this effect can be prevented by frequently alternating treatment between both eyes, remains to be determined. More research is therefore needed to provide patients with an accurate indication of the risks of long-term usage of these lenses.

During counseling, patients with Stargardt disease are commonly advised to limit viewing of intense sunlight based on hypothetical grounds and on evidence from in-vitro- and animal studies. According to our more directly applicable results there is merit to providing such advice.

Qualitative analysis of fundus autofluorescence and OCT

In Chapter 2.2, we investigated the progression of outer retinal damage and atrophy in birdshot chorioretinopathy (BCR) by means of multimodal imaging. Despite recent advances in the laboratory, imaging and clinical diagnostics, monitoring of disease activity and progression of BCR remains difficult; our study addressed this challenge by documenting retinal changes over a long follow-up period.

Our findings suggest that retinal deterioration in BCR may not occur diffusely across the fundus but rather follows a disease front. This is in accordance with recent findings[153, 354] and suggests that IS/OS-disruption may be a suitable progression marker, due to the frequency of occurrence. Only circular chorioretinal lesions do not appear to follow this disease front. The heterogeneity and apparent lack of correlation among our study patients, in terms of clinical activity and the presence of (chorio-) retinal lesions, underscores the difficulty in predicting if and when an individual patient will develop central retinal damage and atrophy. It is possible that the extent and progression rate of outer retinal deterioration in the periphery is correlated with that in the central retina. Future studies should determine if this is the case.

Chapter 4

Interestingly, hyper-AF correlates with outer retinal damage in patients with BCR. Therefore, AF imaging may also be useful to monitor the disease over time and test therapeutic interventions for their efficacy, which may also be reflected by the restoration of outer retinal architecture that we detected in some patients. This effect initiated fairly recently in all four patients, contemporary with intensification of immunosuppressive treatment. We found that restoration can occur not only early on during the disease course [160] but in patients of longer disease duration as well. Our department has adopted an aggressive treatment strategy of active inflammation, which aims to suppress even mild inflammation in BCR in order to preserve visual function (LAW. de Vries, *personal communication*). According to our data, this strategy may lead to restoration of outer retinal structure in a significant number of patients.

Risks of fundus autofluorescence imaging

In Chapter 2.3, we investigated whether AF imaging itself has the potential to cause retinal photic stress in patients with STGD1. To our knowledge, this is the first attempt to numerically simulate induction of photooxidation in the retina in-vivo. As such, it provides a framework for the objective comparison of a variety of exposure regimes in the wavelength range of 380-700 nm, for subjects of different ages. We have also identified a number of parameters that await empirical measurement; we anticipate that more accurate indications of oxygen uptake can be obtained when these parameters are incorporated into this framework.

Evidence from measurements of quantitative AF in patients with STGD1[135] indicates that light absorption by lipofuscin and, by extension, oxygen uptake may already be dramatically increased as early as 7 years of age regardless of the exposure regime. This suggests that oxidative stress in the RPE is increased considerably in patients with STGD1. However, the increased oxygen consumption during daylight may have another effect: chronic hypoxia in the RPE. Consider that lipofuscin accumulation may also reduce diffusion of oxygen from the choroid to the retina.[355] Due to the strong dependence of the outer retina on the choroidal circulation for supply of oxygen and nutrients, this hypoxia may affect the functional and structural integrity of the RPE and photoreceptors. Although RPE-cells can survive hypoxic conditions,[356] their functionality appears to be affected[357] and this may have adverse consequences for photoreceptor cells. Future studies are warranted to measure the oxygen tension in the RPE of patients with STGD1, in order to determine whether the increased oxygen uptake in these patients (Chapter 2.3) is substantial and whether or not it is correlated with hypoxic conditions. We showed that AF-imaging causes additional oxidative stress in the RPE of these patients. Since, at this point, we cannot predict whether this poses a health risk, it would be prudent to limit the acquisition of AF- and fluorescein angiography images of these patients to the minimum required for diagnosis and follow-up. A feasible alternative has been proposed by Cideciyan *et al,*[171] by reducing the retinal exposure and therefore oxidative stress four-fold.

Detection of functional photoreceptors with OCT

Chapter 3 describes our studies focused on functional spectral-domain OCT. Chapter 3.1 contains our study of intrinsic optical signal (IOS) imaging with optical coherence tomography. Considering that the term IOS is relatively vague and is used to describe a wide variety of stimulus-evoked optical changes, we clarified the terminology used in the literature and we reviewed evidence of the biochemical and biophysical characteristics of the phototransduction-associated fast IOS. This comprehensive analysis provides insight into specific methodological requirements of OCT, to enable signal detection in awake humans.

The experimental part of our study investigated relevant motion-associated imaging noise pertaining to the concept of intensity-based analysis of IOS ($\Delta I / I$).[260] We showed and discussed various factors that can cause the background intensity to fluctuate as a consequence of eye or head movements, which probably underlies the poor reproducibility of these signals in awake humans. In a recent review the plethora of techniques used to investigate fast IOS was discussed.[358] Subcellular 3D-imaging with a line-scanning OCT has shown that focal IOS of opposite polarity and of inconsistent amplitudes coexist *within* the outer segments (OS),[359] with highly complicated and poorly consistent courses. Whereas early in-vitro work on isolated rod OS disk membrane utilized IOS to dissect specific processes involved in phototransduction,[246] these recent imaging results suggest that intensity-based IOS reflect the sum of various biochemical processes occurring in concert.[358] None of these processes appear to have a dominant influence in the measured signal.[358]

In the light of the difficulties encountered in intensity-based IOS imaging, it is groundbreaking that a recent paper demonstrated reproducible fluctuation-type fast IOS in awake humans using a swept-source full-field and monochromatic aberration-corrected OCT (SS-FF-OCT).[360] The authors showed consistent increases in the optical path length of OS colocalized with the stimulated retinal area, which rules out the involvement of localized PDE-activity in generating IOS, since that would predict decreases in the measured path length in these biological interferometers (Chapter 3.1, Fig 26). The fact that this technique is based on differences in backscattered photons desensitizes it to the various factors that cause fluctuation in the backscattered intensity that caused substantial noise in earlier intensity-based IOS- measurements (Chapter 3.1). Therefore, I speculate that this technique will be able to perform high-resolution mapping of functional photoreceptors clinically. This ability will be critical in future studies on gene therapy to objectively and accurately determine the therapeutic efficacy in terms of restored visual function.

Detection of abnormal blood flow with OCT

We studied abnormal blood flow patterns in chronic CSC with OCTA, as described in Chapter 3.2. Other similar studies have focused on neovascular disease in CSC and have documented well-defined vascular networks associated with CNV's and focal areas associated with pigment epithelial detachments.[99, 332, 361, 362] In contrast, our study describes aspecific changes of the choriocapillaris in CSC that may be helpful to both understand basic pathophysiology and progression to neovascular disease in those patients.

First of all, I note that we probably misinterpreted the increased and decreased decorrelation signals in OCTA images as increased or decreased flow. Empirical evidence indicates that the time interval between A-scans at the same location, using the Optovue device, is probably poorly matched with intravascular flow speeds and so probably carries no quantitative flow information.[363] A more appropriate interpretation is either presence or absence of flow, with most of the visible variation due to either vessel density, vasodilation/- constriction, or projection artifacts from superficial vessels.[364] Further, we did not correct for projection artifacts in our images prior to annotations even though preliminary corrective algorithms were known.[365] My department has done a follow-up study with such correction algorithms, and our previous results were completely repeated without significant change to the previously described results (T. Theelen, *personal communication*).

Upon reinterpretation of the choriocapillary flow images in Chapter 3.2 according to aforementioned[364] principles, areas of increased decorrelation reflect areas of hyperdense choriocapillary flow. We found this feature to be very common in involved eyes of chronic CSC and always present in case of—and adjacent to—areas of absent flow. Local choriocapillary dilation in CSC[337] or increased choriocapillary density may underlie this hyperdense flow in the context of reactive hyperperfusion. Of particular interest is a recent study that found choriocapillary flow patterns very similar to our patients', in patients with focal choroidal excavations (FCE) and CSC.[366] Results from OCTA and ICGA were indicative of reactive hyperperfusion adjacent to areas of absent flow,[366] which supports our theory of focal choriocapillary ischemia with reactive hyperperfusion in chronic CSC. Future research using quantitative OCTA[330] will be able to prove this theory.

I speculate that OCTA-guided PDT treatment, focusing on areas with hyperdense choriocapillary structures, might improve the therapeutic efficacy of PDT. Note that the postulated effect of PDT—induction of choriocapillary hypoperfusion[341, 367]— is not expected to be directly visible on OCTA, because our OCTA-device is unlikely to provide quantitative flow information.

Concluding remarks

In this thesis we have shown how various imaging biomarkers correlate with retinal (patho-) physiology. We have also modeled cellular effects elicited by fundus autofluorescence. Our findings add important insights into the effects of light exposure on the retinas of patients with STGD1, into pathological features associated with the progression of BCR, and into the pathogenesis of chronic CSC. This thesis focused primarily on imaging techniques that have already shown tremendous clinical value such as spectral-domain OCT and AF-imaging, but also explored new functional imaging techniques with huge potential such as OCTA and OCT-based IOS-imaging. It highlights two fundamental limitations of these techniques: 1) resolution and 2) detection of the intensity of light returning from the retina. These limitations complicate the interpretation of the optical signals investigated herein and introduce considerable sensitivity to background noise. In the future, I expect that these challenges can be addressed by the introduction of new techniques, including adaptive-optics supported techniques, multi-modality analysis, supported by improved image analysis techniques to reduce background noise and to improve the detection of abnormalities in retinal images.

Chapter 4

Chapter 5.

Bibliography

1. Boettner EA, Wolter JR. Transmission of the ocular media. *Invest Ophthalmol.* 1962;1:776-783

2. van de Kraats J, van Norren D. Optical density of the aging human ocular media in the visible and the uv. *J Opt Soc Am A Opt Image Sci Vis.* 2007;24:1842-1857

3. Huxley JB. Phototransduction. *Encyclopedia of neuroscience.* Academic Press; 2009:687-692.

4. Enezi J, Revell V, Brown T, Wynne J, Schlangen L, Lucas R. A "melanopic" spectral efficiency function predicts the sensitivity of melanopsin photoreceptors to polychromatic lights. J *Biol Rhythms.* 2011;26:314-323

5. Sparrow JR, Hicks D, Hamel CP. The retinal pigment epithelium in health and disease. *Curr Mol Med.* 2010;10:802-823

6. Bhutto I, Lutty G. Understanding age-related macular degeneration (amd): Relationships between the photoreceptor/retinal pigment epithelium/bruch's membrane/choriocapillaris complex. *Mol Aspects Med.* 2012;33:295-317

7. Henkind P, Hansen RI, Szalay J. Ocular circulation. In: Records RE, ed. *Physiology of the human eye and visual system.* New York: Harper & Row; 1979:98-155.

8. Hayreh SS. Segmental nature of the choroidal vasculature. *Br J Ophthalmol.* 1975;59:631-648

9. Federman JL. The fenestrations of the choriocapillaris in the presence of choroidal melanoma. *Trans Am Ophthalmol Soc.* 1982;80:498-516

10. Ernest JT, Goldstick TK. Choroidal blood flow measurement in the monkey by clearance of indocyanine green dye. *Exp Eye Res.* 1979;29:7-14

11. Pederson OO. An electron microscopic study of the permeability of intraocular blood vessels using lanthanum as a tracer in-vivo. *Exp Eye Res.* 1979;29:61-69

12. Hayreh SS. The choriocapillaris. *Albrecht Von Graefes Arch Klin Exp Ophthalmol.* 1974;192:165-179

13. Perry HD, Hatfield RV, Tso MO. Fluorescein pattern of the choriocapillaris in the neonatal rhesus monkey. *Am J Ophthalmol.* 1974;84:197-204

14. Aubry JP. Exploration of the choriocapillaris by equidensity technique. *Arch Ophthalmol (Paris).* 1975;35:237-244

15. Zhang HR. Scanning electron-microscopic study of corrosion casts on retinal and choroidal angioarchitecture in man and animals. *Prog Retin Eye Res.* 1994;13:243-270

16. Kuhn H, Hall SW, Wilden U. Light-induced binding of 48-kda protein to photoreceptor membranes is highly enhanced by phosphorylation of rhodopsin. *FEBS Lett.* 1984;176:473-478

17. Pepperberg DR, Cornwall MC, Kahlert M, Hofmann KP, Jin J, Jones GJ, Ripps H. Light-dependent delay in the falling phase of the retinal rod photoresponse. *Vis Neurosci.* 1992;8:9-18

18. Nikonov S, Engheta N, Pugh EN, Jr. Kinetics of recovery of the dark-adapted salamander rod photoresponse. *J Gen Physiol.* 1998;111:7-37

19. Matthews HR, Sampath AP. Photopigment quenching is ca2+ dependent and controls response duration in salamander l-cone photoreceptors. *J Gen Physiol.* 2010;135:355-366

20. Koch KW, Stryer L. Highly cooperative feedback control of retinal rod guanylate cyclase by calcium ions. *Nature.* 1988;334:64-66

21. Anderson RE, Maude MB. Phospholipids of bovine outer segments. *Biochemistry.* 1970;9:3624-3628

22. Liu J, Itagaki Y, Ben-Shabat S, Nakanishi K, Sparrow JR. The biosynthesis of a2e, a fluorophore of aging retina, involves the formation of the precursor, a2-pe, in the photoreceptor outer segment membrane. *J Biol Chem*. 2000;275:29354-29360

23. Poincelot RP, Millar PG, Kimbel RL, Jr., Abrahamson EW. Lipid to protein chromophore transfer in the photolysis of visual pigments. *Nature*. 1969;221:256-257

24. Sun H, Molday RS, Nathans J. Retinal stimulates atp hydrolysis by purified and reconstituted abcr, the photoreceptor-specific atp-binding cassette transporter responsible for stargardt disease. *J Biol Chem*. 1999;274:8269-8281

25. Weng J, Mata NL, Azarian SM, Tzekov RT, Birch DG, Travis GH. Insights into the function of rim protein in photoreceptors and etiology of stargardt's disease from the phenotype in abcr knockout mice. *Cell*. 1999;98:13-23

26. Sparrow JR, Gregory-Roberts E, Yamamoto K, Blonska A, Ghosh SK, Ueda K, Zhou J. The bisretinoids of retinal pigment epithelium. *Prog Retin Eye Res*. 2012;31:121-135

27. Beharry S, Zhong M, Molday RS. N-retinylidene-phosphatidylethanolamine is the preferred retinoid substrate for the photoreceptor-specific abc transporter abca4 (abcr). *J Biol Chem*. 2004;279:53972-53979

28. Molday LL, Rabin AR, Molday RS. Abcr expression in foveal cone photoreceptors and its role in stargardt macular dystrophy. *Nat Genet*. 2000;25:257-258

29. Molday RS, Molday LL. Identification and characterization of multiple forms of rhodopsin and minor proteins in frog and bovine rod outer segment disc membranes. Electrophoresis, lectin labeling, and proteolysis studies. *J Biol Chem*. 1979;254:4653-4660

30. Papermaster DS, Schneider BG, Zorn MA, Kraehenbuhl JP. Immunocytochemical localization of a large intrinsic membrane protein to the incisures and margins of frog rod outer segment disks. *J Cell Biol*. 1978;78:415-425

31. Sun H, Nathans J. Stargardt's abcr is localized to the disc membrane of retinal rod outer segments. *Nat Genet*. 1997;17:15-16

32. Sun H, Nathans J. Abcr, the atp-binding cassette transporter responsible for stargardt macular dystrophy, is an efficient target of all-trans-retinal-mediated photooxidative damage in vitro. Implications for retinal disease. *J Biol Chem*. 2001;276:1176 6-11774

33. Sun H, Nathans J. Mechanistic studies of abcr, the abc transporter in photoreceptor outer segments responsible for autosomal recessive stargardt disease. *J Bioenerg Biomembr*. 2001;33:523-530

34. Gonzalez-Fernandez F. Evolution of the visual cycle: The role of retinoid-binding proteins. J *Endocrinol*. 2002;175:75-88

35. Saari JC, Bredberg DL. Lecithin:Retinol acyltransferase in retinal pigment epithelial microsomes. *J Biol Chem*. 1989;264:8636-8640

36. Trehan A, Canada FJ, Rando RR. Inhibitors of retinyl ester formation also prevent the biosynthesis of 11-cis-retinol. *Biochemistry*. 1990;29:309-312

37. Deigner PS, Law WC, Canada FJ, Rando RR. Membranes as the energy source in the endergonic transformation of vitamin a to 11-cis-retinol. *Science*. 1989;244:968-971

Chapter 5

38.   Moiseyev G, Chen Y, Takahashi Y, Wu BX, Ma JX. Rpe65 is the isomerohydrolase in the retinoid visual cycle. *Proc Natl Acad Sci U S A.* 2005;102:12413-12418

39.   Saari JC, Nawrot M, Kennedy BN, Garwin GG, Hurley JB, Huang J, Possin DE, Crabb JW. Visual cycle impairment in cellular retinaldehyde binding protein (cralbp) knockout mice results in delayed dark adaptation. *Neuron.* 2001;29:739-748

40.   Goldstein EB, Wolf BM. Regeneration of the green-rod pigment in the isolated frog retina. *Vision Res.* 1973;13:527-534

41.   Hood DC, Hock PA. Recovery of cone receptor activity in the frog's isolated retina. *Vision Res.* 1973;13:1943-1951

42.   Mata NL, Radu RA, Clemmons RC, Travis GH. Isomerization and oxidation of vitamin a in cone-dominant retinas: A novel pathway for visual-pigment regeneration in daylight. *Neuron.* 2002;36:69-80

43.   Kefalov VJ. Rod and cone visual pigments and phototransduction through pharmacological, genetic, and physiological approaches. *J Biol Chem.* 2012;287:1635-1641

44.   Dimmer F. Die photografie des augenhintergrundes. Wiesbaden: J.F. Bergmann; 1907. 1907

45.   Webb RH, Hudges GW. Scanning laser ophthalmoscope. *IEEETrans Biomed Eng.* 1981;28:488-492

46.   von Ruckmann A, Fitzke FW, Bird AC. *Distribution* of fundus autofluorescence with a scanning laser ophthalmoscope. *Br J Ophthalmol.* 1995;79:407-412

47.   Huang D, Swanson EA, Lin CP, Schuman JS, Stinson WG, Chang W, Hee MR, Flotte T, Gregory K, Puliafito CA, Fujimoto JG. Optical coherence tomography. *Science.* 1991;254:1178-1181

48.   Sparrow JR, Duncker T. Fundus autofluorescence and rpe lipofuscin in age-related macular degeneration. *J Clin Med.* 2014;3:1302-1321

49.   Schmitz-Valckenberg S, Holz FG, Bird AC, Spaide RF. Fundus autofluorescence imaging: Review and perspectives. *Retina.* 2008;28:385-409

50.   Rudolf M, Vogt SD, Curcio CA, Huisingh C, McGwin G, Jr., Wagner A, Grisanti S, Read RW. Histologic basis of variations in retinal pigment epithelium autofluorescence in eyes with geographic atrophy. *Ophthalmology.* 2013;120:821-828

51.   Sparrow JR, Marsiglia M, Allikmets R, Tsang S, Lee W, Duncker T, Zernant J. Flecks in recessive stargardt disease: Short-wavelength autofluorescence, near-infrared autofluorescence, and optical coherence tomography. *Invest Ophthalmol Vis Sci.* 2015;56:5029-5039

52.   Kim SR, Jang YP, Sparrow JR. Photooxidation of rpe lipofuscin bisretinoids enhances fluorescence intensity. *Vision Res.* 2010;50:729-736

53.   Delori FC, Dorey CK, Staurenghi G, Arend O, Goger DG, Weiter JJ. In vivo fluorescence of the ocular fundus exhibits retinal pigment epithelium lipofuscin characteristics. *Invest Ophthalmol Vis Sci.* 1995;36:718-729

54.   Ruggiero L, Finnemann SC. Rhythmicity of the retinal pigment epithelium. In: Tosini G, Iuvone PM, McMahon DG, eds. *The retina and circadian rhythms.* Springer Press; 2014.

55.   Moussa NB. Multicolor imaging in the evaluation of geographic atrophy due to age-related macular degeneration. *Br J Ophthalmol.* 2015

56. North V, Gelman R, Tsang SH. Juvenile-onset macular degeneration and allied disorders. *Dev Ophthalmol*. 2014;53:44-52

57. Holz FG, Strauss EC, Schmitz-Valckenberg S, van Lookeren Campagne M. Geographic atrophy: Clinical features and potential therapeutic approaches. *Ophthalmology*. 2014;121:1079-1091

58. Zarbin MA, Casaroli-Marano RP, Rosenfeld PJ. Age-related macular degeneration: Clinical findings, histopathology and imaging techniques. *Dev Ophthalmol*. 2014;53:1-32

59. Holz FG, Bindewald-Wittich A, Fleckenstein M, Dreyhaupt J, Scholl HP, Schmitz-Valckenberg S, Group FA-S. Progression of geographic atrophy and impact of fundus autofluorescence patterns in age-related macular degeneration. *Am J Ophthalmol*. 2007;143:463-472

60. Gray DC, Merigan W, Wolfing JI, Gee BP, Porter J, Dubra A, Twietmeyer TH, Ahamd K, Tumbar R, Reinholz F, Williams DR. In vivo fluorescence imaging of primate retinal ganglion cells and retinal pigment epithelial cells. *Opt Express*. 2006;14:7144-7158

61. Allikmets R, Singh N, Sun H, Shroyer NF, Hutchinson A, Chidambaram A, Gerrard B, Baird L, Stauffer D, Peiffer A, Rattner A, Smallwood P, Li Y, Anderson KL, Lewis RA, Nathans J, Leppert M, Dean M, Lupski JR. A photoreceptor cell-specific atp-binding transporter gene (abcr) is mutated in recessive stargardt macular dystrophy. *Nat Genet*. 1997;15:236-246

62. Cukras CA, Wong WT, Caruso R, Cunningham D, Zein W, Sieving PA. Centrifugal expansion of fundus autofluorescence patterns in stargardt disease over time. *Arch Ophthalmol*. 2012;130:171-179

63. Murakami T, Akimoto M, Ooto S, Suzuki T, Ikeda H, Kawagoe N, Takahashi M, Yoshimura N. Association between abnormal autofluorescence and photoreceptor disorganization in retinitis pigmentosa. *Am J Ophthalmol*. 2008;145:687-694

64. Popovic P, Jarc-Vidmar M, Hawlina M. Abnormal fundus autofluorescence in relation to retinal function in patients with retinitis pigmentosa. *Graefes Arch Clin Exp Ophthalmol*. 2005;243:1018-1027

65. Wakabayashi T, Sawa M, Gomi F, Tsujikawa M. Correlation of fundus autofluorescence with photoreceptor morphology and functional changes in eyes with retinitis pigmentosa. *Acta Ophthalmol*. 2010;88:e177-183

66. Sujirakul T, Davis R, Erol D, Zhang L, Schillizzi G, Royo-Dujardin L, Shen S, Tsang S. Bilateral concordance of the fundus hyperautofluorescent ring in typical retinitis pigmentosa patients. *Ophthalmic Genet*. 2015;36:113-122

67. Robson AG, Egan C, Holder GE, Bird AC, Fitzke FW. Comparing rod and cone function with fundus autofluorescence images in retinitis pigmentosa. *Adv Exp Med Biol*. 2003;533:41-47

68. Robson AG, Egan CA, Luong VA, Bird AC, Holder GE, Fitzke FW. Comparison of fundus autofluorescence with photopic and scotopic fine-matrix mapping in patients with retinitis pigmentosa and normal visual acuity. *Invest Ophthalmol Vis Sci*. 2004;45:4119-4125

69. Robson AG, El-Amir A, Bailey C, Egan CA, Fitzke FW, Webster AR, Bird AC, Holder GE. Pattern erg correlates of abnormal fundus autofluorescence in patients with retinitis pigmentosa and normal visual acuity. *Invest Ophthalmol Vis Sci*. 2003;44:3544-3550

Chapter 5

70. Robson AG, Saihan Z, Jenkins SA, Fitzke FW, Bird AC, Webster AR, Holder GE. Functional characterisation and serial imaging of abnormal fundus autofluorescence in patients with retinitis pigmentosa and normal visual acuity. *Br J Ophthalmol.* 2006;90:472-479

71. Robson AG, Tufail A, Fitzke F, Bird AC, Moore AT, Holder GE, Webster AR. Serial imaging and structure-function correlates of high-density rings of fundus autofluorescence in retinitis pigmentosa. *Retina.* 2011;31:1670-1679

72. Wojtkowski M, Srinivasan V, Ko T, Fujimoto J, Kowalczyk A, Duker J. Ultrahigh-resolution, high-speed, fourier domain optical coherence tomography and methods for dispersion compensation. *Opt Express.* 2004;12:2404-2422

73. Nassif N, Cense B, Park B, Pierce M, Yun S, Bouma B, Tearney G, Chen T, de Boer J. In vivo high-resolution video-rate spectral-domain optical coherence tomography of the human retina and optic nerve. *Opt Express.* 2004;12:367-376

74. Izatt J, Choma MA, Dhalla AH. Theory of optical coherence tomography. *Optical coherence tomography: Technology and applications, second edition. S*pringer International; 2015:65-94.

75. Fercher AF, Drexler W, Hitzenberger CK, Lasser T. Optical coherence tomography - principles and applications. *Rep Prog Phys.* 2003;66:239-303

76. Schmitt JM, Kumar G. Optical scattering properties of soft tissue: A discrete particle model. *Appl Opt.* 1998;37:2788-2797

77. Swanson EA, Izatt JA, Hee MR, Huang D, Lin CP, Schuman JS, Puliafito CA, Fujimoto JG. In vivo retinal imaging by optical coherence tomography. *Opt Lett.* 1993;18:1864-1866

78. Nassif N, Cense B, Park BH, Yun SH, Chen TC, Bouma BE, Tearney GJ, de Boer JF. In vivo human retinal imaging by ultrahigh-speed spectral domain optical coherence tomography. *Opt Lett.* 2004;29:480-482

79. Hunter DG, Patel SN, Guyton DL. Automated detection of foveal fixation by use of retinal birefringence scanning. *Appl Opt.* 1999;38:1273-1279

80. Lujan BJ, Roorda A, Knighton RW, Carroll J. Revealing henle's fiber layer using spectral domain optical coherence tomography. *Invest Ophthalmol Vis Sci.* 2011;52:1486-1492

81. Staurenghi G, Sadda S, Chakravarthy U, Spaide RF, International Nomenclature for Optical Coherence Tomography P. Proposed lexicon for anatomic landmarks in normal posterior segment spectral-domain optical coherence tomography: The in*oct consensus. *Ophthalmology.* 2014;121:1572-1578

82. Leung CK. Diagnosing glaucoma progression with optical coherence tomography. *Curr Opin Ophthalmol.* 2014;25:104-111

83. Weinreb RN, Khaw PT. Primary open-angle glaucoma. *Lancet.* 2004;363:1711-1720

84. Kocaoglu OP, Lee S, Jonnal RS, Wang Q, Herde AE, Derby JC, Gao W, Miller DT. Imaging cone photoreceptors in three dimensions and in time using ultrahigh resolution optical coherence tomography with adaptive optics. *Biomed Opt Express.* 2011;2:748-763

85. Scoles D, Flatter JA, Cooper RF, Langlo CS, Robison S, Neitz M, Weinberg DV, Pennesi ME, Han DP, Dubra A, Carroll J. Assessing photoreceptor structure associated with ellipsoid zone disruptions visualized with optical coherence tomography. *Retina.* 2015

86. Huang D, Swanson EA, Lin CP, Schuman JS, Stinson WG, Chang W, Hee MR, Flotte T, Gregory K, Puliafito CA, et al. Optical coherence tomography. *Science*. 1991;254:1178-1181

87. Adler DC, Huang SW, Huber R, Fujimoto JG. Photothermal detection of gold nanoparticles using phase-sensitive optical coherence tomography. *Opt Express*. 2008;16:4376-4393

88. Lee TM, Oldenburg AL, Sitafalwalla S, Marks DL, Luo W, Toublan FJ, Suslick KS, Boppart SA. Engineered microsphere contrast agents for optical coherence tomography. *Opt Lett*. 2003;28:1546-1548

89. Wang S, Larin KV. Shear wave imaging optical coherence tomography (swi-oct) for ocular tissue biomechanics. *Opt Lett*. 2014;39:41-44

90. Zhao Y, Chen Z, Saxer C, Xiang S, de Boer JF, Nelson JS. Phase-resolved optical coherence tomography and optical doppler tomography for imaging blood flow in human skin with fast scanning speed and high velocity sensitivity. *Opt Lett. 2*000;25:114-116

91. Wang RK, Jacques SL, Ma Z, Hurst S, Hanson SR, Gruber A. Three dimensional optical angiography. *Opt Express*. 2007;15:4083-4097

92. Wang XJ, Milner TE, Nelson JS. Characterization of fluid flow velocity by optical doppler tomography. *Opt Lett*. 1995;20:1337-1339

93. Chen Z, Milner TE, Dave D, Nelson JS. Optical doppler tomographic imaging of fluid flow velocity in highly scattering media. *Opt Lett*. 1997;22:64-66

94. Barton J, Stromski S. Flow measurement without phase information in optical coherence tomography images. *Opt Express*. 2005;13:5234-5239

95. Mariampillai A, Standish BA, Moriyama EH, Khurana M, Munce NR, Leung MK, Jiang J, Cable A, Wilson BC, Vitkin IA, Yang VX. Speckle variance detection of microvasculature using swept-source optical coherence tomography. *Opt Lett*. 2008;33:1530-1532

96. Jia Y, Tan O, Tokayer J, Potsaid B, Wang Y, Liu JJ, Kraus MF, Subhash H, Fujimoto JG, Hornegger J, Huang D. Split-spectrum amplitude-decorrelation angiography with optical coherence tomography. *Opt Express*. 2012;20:4710-4725

97. Li W, Lancee CT, Cespedes EI, van der Scteen AFW, Bom N. Decorrelation of intravascular ultrasound signals: A computer simulation study. *Ultrasonic symposium, 1997. Proceedings, 1997*. IEEE; 1997:1165-1168.

98. de Kinkelder R, Kalkman J, Faber DJ, Schraa O, Kok PH, Verbraak FD, van Leeuwen TG. Heartbeat-induced axial motion artifacts in optical coherence tomography measurements of the retina. *Invest Ophthalmol Vis Sci*. 2011;52:3908-3913

99. Quaranta-El Maftouhi M, El Maftouhi A, Eandi CM. Chronic central serous chorioretinopathy imaged by optical coherence tomographic angiography. *Am J Ophthalmol*. 2015;160:581-587 e581

100. Tso DY, Frostig RD, Lieke EE, Grinvald A. Functional-organization of primate visual-cortex revealed by high-resolution optical imaging. *Science*. 1990;249:417-420

101. Grinvald A, Shoham D, Glaser D. In-vivo optical imaging of cortical architecture and dynamics. In: Weindhorts U, Johansson H, eds. *Modern techniques in neuroscience research*. Berlin: Springer Verlag; 2001.

Chapter 5

102. Klevering BJ, Deutman AF, Maugeri A, Cremers FPM, Hoyng CB. The spectrum of retinal phenotypes caused by mutations in the abca4 gene. *Graef Arch Clin Exp.* 2005;243:90-100

103. Azarian SM, Travis GH. The photoreceptor rim protein is an abc transporter encoded by the gene for recessive stargardt's disease (abcr). *FEBS Lett.* 1997;409:247-252

104. Illing M, Molday LL, Molday RS. The 220-kda rim protein of retinal rod outer segments is a member of the abc transporter superfamily. *J Biol Chem.* 1997;272:10303-10310

105. Organisciak DT, Vaughan DK. Retinal light damage: Mechanisms and protection. *Prog Retin Eye Res.* 2010;29:113-134

106. Eldred GE, Lasky MR. Retinal age pigments generated by self-assembling lysosomotropic detergents. *Nature.* 1993;361:724-726

107. Ablonczy Z, Higbee D, Anderson DM, Dahrouj M, Grey AC, Gutierrez D, Koutalos Y, Schey KL, Hanneken A, Crouch RK. Lack of correlation between the spatial distribution of a2e and lipofuscin fluorescence in the human retinal pigment epithelium. *Invest Ophthalmol Vis Sci.* 2013;54:5535-5542

108. Mata NL, Weng J, Travis GH. Biosynthesis of a major lipofuscin fluorophore in mice and humans with abcr-mediated retinal and macular degeneration. *P Natl Acad Sci USA. 2000;97:7154-7159*

109. Mata NL, Tzekov RT, Liu X, Weng J, Birch DG, Travis GH. Delayed dark-adaptation and lipofuscin accumulation in abcr+/- mice: Implications for involvement of abcr in age-related macular degeneration. *Invest Ophthalmol Vis Sci.* 2001;42:1685-1690

110. Davies S, Elliott MH, Floor E, Truscott TG, Zareba M, Sarna T, Shamsi FA, Boulton ME. Photocytotoxicity of lipofuscin in human retinal pigment epithelial cells. *Free Radic Biol Med.* 2001;31:256-265

111. Godley BF, Shamsi FA, Liang FQ, Jarrett SG, Davies S, Boulton M. Blue light induces mitochondrial DNA damage and free radical production in epithelial cells. *J Biol Chem.* 2005;280:21061-21066

112. Shamsi FA, Boulton M. Inhibition of rpe lysosomal and antioxidant activity by the age pigment lipofuscin. *Invest Ophthalmol Vis Sci.* 2001;42:3041-3046

113. Radu RA, Mata NL, Bagla A, Travis GH. Light exposure stimulates formation of a2e oxiranes in a mouse model of stargardt's macular degeneration. *P Natl Acad Sci USA.* 2004;101:5928-5933

114. Paskowitz DM, LaVail MM, Duncan JL. Light and inherited retinal degeneration. Brit J *Ophthalmol.* 2006;90:1060-1066

115. Berson EL. Light deprivation and retinitis pigmentosa. *Vision Res.* 1980;20:1179-1184

116. Smith RT, Gomes NL, Barile G, Busuioc M, Lee N, Laine A. Lipofuscin and autofluorescence metrics in progressive stgd. *Invest Ophth Vis Sci.* 2009;50:3907-3914

117. Smith RT. Fundus autofluorescence patterns in stargardt disease over time. *Arch Ophthalmol.* 2012;130:1354; author reply 1354-1355

118. McBain VA, Lois N. Progression of retinal pigment epithelial atrophy in stargardt disease. *Am J Ophthalmol 2012;*154:146-154

119. Allikmets R. Stargardt disease. In: Tombran-Tink J, Barnstable CJ, eds. *Retinal degenerations.* Totowa: Humana Press; 2007:105-118.

120. Fishman GA, Stone EM, Grover S, Derlacki DJ, Haines HL, Hockey RR. Variation of clinical expression in patients with stargardt dystrophy and sequence variations in the abcr gene. *Arch Ophthalmol.* 1999;117:504-510

121. Cideciyan AV, Aleman TS, Swider M, Schwartz SB, Steinberg JD, Brucker AJ, Maguire AM, Bennett J, Stone EM, Jacobson SG. Mutations in abca4 result in accumulation of lipofuscin before slowing of the retinoid cycle: A reappraisal of the human disease sequence. *Hum Mol Genet.* 2004;13:525-534

122. Smith RT, Nagasaki T, Sparrow JR, Barbazetto I, Klaver CC, Chan JK. A method of drusen measurement based on the geometry of fundus reflectance. *Biomed Eng Online.* 2003;2:10

123. Smith RT, Koniarek JP, Chan J, Nagasaki T, Sparrow JR, Langton K. Autofluorescence characteristics of normal foveas and reconstruction of foveal autofluorescence from limited data subsets. *Invest Ophth Vis Sci.* 2005;46:2940-2946

124. Smith RT, Chan JK, Busuoic M, Sivagnanavel V, Bird AC, Chong NV. Autofluorescence characteristics of early, atrophic, and high-risk fellow eyes in age-related macular degeneration. *Invest Ophth Vis Sci.* 2006;47:5495-5504

125. Wu L, Ueda K, Nagasaki T, Sparrow JR. Light damage in abca4 and rpe65rd12 mice. *Invest Ophthalmol Vis Sci.* 2014;55:1910-1918

126. Hunter JJ, Morgan JI, Merigan WH, Sliney DH, Sparrow JR, Williams DR. The susceptibility of the retina to photochemical damage from visible light. *Prog Retin Eye Res.* 2012;31:28-42

127. Ham WT, Jr., Mueller HA, Sliney DH. Retinal sensitivity to damage from short wavelength light. *Nature.* 1976;260:153-155

128. Ham WT, Jr., Mueller HA, Ruffolo JJ, Jr., Millen JE, Cleary SF, Guerry RK, Guerry D, 3rd. Basic mechanisms underlying the production of photochemical lesions in the mammalian retina. *Curr Eye Res.* 1984;3:165-174

129. Ham WT, Jr., Allen RG, Feeney-Burns L. The involvement of the retinal pigment epithelium. In: Waxler M, Hitchins VM, eds. *Crc optical radiation and visual health.* Boca Raton, FL: CRC Press, Inc; 1986:43-67.

130. Friedman E, Kuwabara T. The retinal pigment epithelium. Iv. The damaging effects of radiant energy. *Arch Ophthalmol.* 1968;80:265-279

131. Busch EM, Gorgels TG, Roberts JE, van Norren D. The effects of two stereoisomers of n-acetylcysteine on photochemical damage by uva and blue light in rat retina. *Photochem Photobiol.* 1999;70:353-358

132. Ham WT, Jr., Ruffolo JJ, Jr., Mueller HA, Clarke AM, Moon ME. Histologic analysis of photochemical lesions produced in rhesus retina by short-wave-length light. *Invest Ophthalmol Vis Sci.* 1978;17:1029-1035

133. Charbel Issa P, Barnard AR, Singh MS, Carter E, Jiang Z, Radu RA, Schraermeyer U, MacLaren RE. Fundus autofluorescence in the abca4(-/-) mouse model of stargardt disease--correlation with accumulation of a2e, retinal function, and histology. *Invest Ophthalmol Vis Sci.* 2013;54:5602-5612

Chapter 5

134. Delori F, Greenberg JP, Woods RL, Fischer J, Duncker T, Sparrow J, Smith RT. Quantitative measurements of autofluorescence with the scanning laser ophthalmoscope. *Invest Ophthalmol Vis Sci.* 2011;52:9379-9390

135. Burke TR, Duncker T, Woods RL, Greenberg JP, Zernant J, Tsang SH, Smith RT, Allikmets R, Sparrow JR, Delori FC. Quantitative fundus autofluorescence in recessive stargardt disease. *Invest Ophthalmol Vis Sci.* 2014;55:2841-2852

136. Lambertus S, van Huet RAC, Bax NM, Hoefsloot LH, Cremers FPM, Boon CJF, Klevering BJ, Hoyng CB. Early-onset stargardt disease: phenotypic and genotypic characteristics. *Ophthalmology.* 2015;122:335-344

137. Morgan JIW, Hunter JJ, Masella B, Wolfe R, Gray DC, Merigan WH, Delori FC, Williams DR. Light-induced retinal changes observed with high-resolution autofluorescence imaging of the retinal pigment epithelium. *Invest Ophth Vis Sci.* 2008;49:3715-3729

138. Zhou J, Sparrow JR. Light filtering in a retinal pigment epithelial cell culture model. *Optom Vis Sci.* 2011;88:759-765

139. Sparrow JR, Nakanishi K, Parish CA. The lipofuscin fluorophore a2e mediates blue light-induced damage to retinal pigmented epithelial cells. *Invest Ophthalmol Vis Sci.* 2000;41:1981-1989

140. Sparrow JR, Cai BL. Blue light-induced apoptosis of a2e-containing rpe: Involvement of caspase-3 and protection by bcl-2. *Invest Ophth Vis Sci.* 2001;42:1356-1362

141. Schutt F, Davies S, Kopitz J, Holz FG, Boulton ME. Photodamage to human rpe cells by a2-e, a retinoid component of lipofuscin. *Invest Ophthalmol Vis Sci.* 2000;41:2303-2308

142. Ryan SJ, Maumenee AE. Birdshot retinochoroidopathy. *Am J Ophthalmol.* 1980;89:31-45

143. Smit RL, Baarsma GS, de Vries J. Classification of 750 consecutive uveitis patients in the rotterdam eye hospital. *Int Ophthalmol.* 1993;17:71-76

144. Rodriguez A, Calonge M, Pedroza-Seres M, Akova YA, Messmer EM, D'Amico DJ, Foster CS. Referral patterns of uveitis in a tertiary eye care center. *Arch Ophthalmol.* 1996;114:593-599

145. Rothova A, Suttorp-van Schulten MS, Frits Treffers W, Kijlstra A. Causes and frequency of blindness in patients with intraocular inflammatory disease. *Br J Ophthalmol.* 1996;80:332-336

146. Baarsma GS, Priem HA, Kijlstra A. Association of birdshot retinochoroidopathy and hla-a29 antigen. *Curr Eye Res.* 1990;9 Suppl:63-68

147. Levinson RD, Brezin A, Rothova A, Accorinti M, Holland GN. Research criteria for the diagnosis of birdshot chorioretinopathy: Results of an international consensus conference. *Am J Ophthalmol.* 2006;141:185-187

148. Kuiper JJ, Van Setten J, Ripke S, Van 't Slot R, Mulder F, Missotten T, Baarsma GS, Francioli LC, Pulit SL, De Kovel CG, Ten Dam-Van Loon N, Den Hollander AI, Huis In Het Veld P, Hoyng CB, Cordero-Coma M, Martin J, Llorenc V, Arya B, Thomas D, Bakker SC, Ophoff RA, Rothova A, De Bakker PI, Mutis T, Koeleman BP. A genome-wide association study identifies a functional erap2 haplotype associated with birdshot chorioretinopathy. *Hum Mol Genet.* 2014;23:6081-6087

149. Kuiper JJ, Rothova A, Schellekens PA, Ossewaarde-van Norel A, Bloem AC, Mutis T. Detection of choroid- and retina-antigen reactive cd8(+) and cd4(+) t lymphocytes in the vitreous fluid of patients with birdshot chorioretinopathy. *Hum Immunol.* 2014;75:570-577

150. Levinson RD, Monnet D. Imaging in birdshot chorioretinopathy. *Int Ophthalmol Clin.* 2012;52:191-198

151. Birnbaum AD, Fawzi AA, Rademaker A, Goldstein DA. Correlation between clinical signs and optical coherence tomography with enhanced depth imaging findings in patients with birdshot chorioretinopathy. *JAMA Ophthalmol.* 2014;132:929-935

152. Young M, Fallah N, Forooghian F. Choroidal degeneration in birdshot chorioretinopathy. *Retina.* 2015;35:798-802

153. Keane PA, Allie M, Turner SJ, Southworth HS, Sadda SR, Murray PI, Denniston AK. Characterization of birdshot chorioretinopathy using extramacular enhanced depth optical coherence tomography. *JAMA Ophthalmol.* 2013;131:341-350

154. Theelen T, Berendschot TT, Boon CJ, Hoyng CB, Klevering BJ. Analysis of visual pigment by fundus autofluorescence. *Exp Eye Res.* 2008;86:296-304

155. Piffer AL, Boissonnot M, Gobert F, Zenger A, Wolf S, Wolf U, Korobelnik JF, Rougier MB. Relevance of wide-field autofluorescence imaging in birdshot retinochoroidopathy: Descriptive analysis of 76 eyes. *Acta Ophthalmol.* 2014;92:e463-469

156. Kramer M, Priel E. Fundus autofluorescence imaging in multifocal choroiditis: Beyond the spots. *Ocul Immunol Inflamm.* 2014;22:349-355

157. van Grinsven MJ, Buitendijk GH, Brussee C, van Ginneken B, Hoyng C, Theelen T, Klaver CC, Sanchez CI. Automatic identification of reticular pseudodrusen using multimodal retinal image analysis. *Invest Ophthalmol Vis Sci.* 2015

158. Kuiper JJ, Missotten T, Baarsma SG, Rothova A. Vision-related quality of life in patients with birdshot chorioretinopathy. *Acta Ophthalmol.* 2013;91:e329-331

159. Koizumi H, Pozzoni MC, Spaide RF. Fundus autofluorescence in birdshot chorioretinopathy. *Ophthalmology.* 2008;115:e15-20

160. Forooghian F, Gulati N, Jabs DA. Restoration of retinal architecture following systemic immunosuppression in birdshot chorioretinopathy. *Ocul Immunol Inflamm.* 2010;18:470-471

161. Hood DC, Ramachandran R, Holopigian K, Lazow M, Birch DG, Greenstein VC. Method for deriving visual field boundaries from oct scans of patients with retinitis pigmentosa. *Biomed Opt Express.* 2011;2:1106-1114

162. Rozanowska M, Rozanowski B. Visual transduction and age-related changes in lipofuscin. In: Tombran-Tink J, Barnstable CJ, eds. *Ophthalmology research: The visual transduction cascade.* Totowa, NJ: The Humana Press Inc.; 2008:405-446.

163. Dowling JE, Sidman RL. Inherited retinal dystrophy in the rat. *J Cell Biol.* 1962;14:73-109

164. Matthes MT, LaVail MM. Inherited retinal dystrophy in the rcs rat: Composition of the outer segment debris zone. *Prog Clin Biol Res.* 1989;314:315-330

165. D'Cruz PM, Yasumura D, Weir J, Matthes MT, Abderrahim H, LaVail MM, Vollrath D. Mutation of the receptor tyrosine kinase gene mertk in the retinal dystrophic rcs rat. *Hum Mol Genet.* 2000;9:645-651

166. Wing GL, Blanchard GC, Weiter JJ. The topography and age relationship of lipofuscin concentration in the retinal pigment epithelium. *Invest Ophthalmol Vis Sci.* 1978;17:601-607

Chapter 5

167. ANSI. American national standard for safe use of lasers (ansi 136.1). *Ansi 136.1-2007.* The Laser Institute of America; 2007.

168. Sliney D, Aron-Rosa D, DeLori F, Fankhauser F, Landry R, Mainster M, Marshall J, Rassow B, Stuck B, Trokel S, West TM, Wolffe M. Adjustment of guidelines for exposure of the eye to optical radiation from ocular instruments: Statement from a task group of the international commission on non-ionizing radiation protection (icnirp). *Appl Optics.* 2005;44:2162-2176

169. Delori FC, Webb RH, Sliney DH. Maximum permissible exposures for ocular safety (ansi 2000), with emphasis on ophthalmic devices. *J Opt Soc Am A.* 2007;24:1250-1265

170. Cideciyan AV, Jacobson SG, Aleman TS, Gu DN, Pearce-Kelling SE, Sumaroka A, Acland GM, Aguirre GD. In vivo dynamics of retinal injury and repair in the rhodopsin mutant dog model of human retinitis pigmentosa. *P Natl Acad Sci USA.* 2005;102:5233-5238

171. Cideciyan AV, Swider M, Aleman TS, Roman MI, Sumaroka A, Schwartz SB, Stone EM, Jacobson SG. Reduced-illuminance autofluorescence imaging in abca4-associated retinal degenerations. *J Opt Soc Am A.* 2007;24:1457-1467

172. Teussink MM, Lee MD, Smith RT, van Huet RA, Klaver CC, Klevering BJ, Theelen T, Hoyng CB. The effect of light deprivation in patients with stargardt disease. *Am J Ophthalmol.* 2015;159:964-972 e962

173. Yannuzzi LA, Fisher YL, Krueger A, Slakter J. Solar retinopathy: A photobiological and geophysical analysis. *Trans Am Ophthalmol Soc.* 1987;85:120-158

174. American Society for Testing and Materials A. Standard tables for reference solar spectral irradiance at air mass 1.5: Direct normal spectrum for a 37 degree tilted surface (astm g173-03 global tilt), iso 9845-1, 1992. . 1999

175. Burns SA, Webb RH. Optical generation of the visual stimulus. In: Bass M, van Stryland EW, Williams DR, Wolfe WL, eds. *Handbook of optics.* McGrawhill; 1994:1-28.

176. Winn B, Whitaker D, Elliott DB, Phillips NJ. Factors affecting light-adapted pupil size in normal human subjects. *Invest Ophthalmol Vis Sci.* 1994;35:1132-1137

177. Pokorny J, Smith VC, Lutze M. Aging of the human lens. *Appl Opt.* 1987;26:1437-1440

178. Dryja TP, O'Neil-Dryja M, Albert DM. Elemental analysis of melanins from bovine hair, iris, choroid, and retinal pigment epithelium. *Invest Ophthalmol Vis Sci.* 1979;18:231-236

179. Nofsinger JB, Forest SE, Simon JD. Explanations for the disparity among absorption and action spectra of eumelanin *J. Phys. Chem.* 1999;103:11428-11432

180. Prahl SA, Keijzer SL, Jacques SL, Welch AJ. A monte carlo model of light propagation in tissue. *SPIE Inst Ser IS 5.* 1989:102-111

181. Wang L, Jacques SL, Zheng L. Mcml--monte carlo modeling of light transport in multi-layered tissues. *Comput Methods Programs Biomed.* 1995;47:131-146

182. Bergougnoux L, Misguich-Ripault J, Firpo JL, Andre J. Monte carlo calculation of backscattered light intensity by suspension: Comparison with experimental data. *Appl Opt.* 1996;35:1735-1741

183. Tran NT, Campbell CG, Shi FG. Study of particle size effects on an optical fiber sensor response examined with monte carlo simulation. *Appl Opt.* 2006;45:7557-7566

184. Cracknell KP, Farnell DJ, Grierson I. Monte carlo simulation of latanoprost induced iris darkening. *Comput Methods Programs Biomed.* 2007;87:93-103

185. Weiter JJ, Delori FC, Wing GL, Fitch KA. Retinal pigment epithelial lipofuscin and melanin and choroidal melanin in human eyes. *Invest Ophthalmol Vis Sci.* 1986;27:145-152

186. van Gemert JC, Berenbaum MC, Gijsbers GH. Wavelength and light-dose dependence in tumour phototherapy with haematoporphyrin derivative. *Br J Cancer.* 1985;52:43-49

187. Kawauchi S, Sato S, Morimoto Y, Kikuchi M. Correlation between oxygen consumption and photobleaching during in vitro photodynamic treatment with atx-s10.Na(ii) using pulsed light excitation: Dependence of pulse repetition rate and irradiation time. *Photochem Photobiol.* 2004;80:216-223

188. Boulton M, Docchio F, Dayhaw-Barker P, Ramponi R, Cubeddu R. Age-related changes in the morphology, absorption and fluorescence of melanosomes and lipofuscin granules of the retinal pigment epithelium. *Vision Res.* 1990;30:1291-1303

189. Sparrow JR, Blonska A, Flynn E, Duncker T, Greenberg JP, Secondi R, Ueda K, Delori FC. Quantitative fundus autofluorescence in mice: Correlation with hplc quantitation of rpe lipofuscin and measurement of retina outer nuclear layer thickness. *Invest Ophthalmol Vis Sci.* 2013;54:2812-2820

190. Delori FC, Staurenghi G, Arend O, Dorey CK, Goger DG, Weiter JJ. In vivo measurement of lipofuscin in stargardt's disease--fundus flavimaculatus. *Invest Ophthalmol Vis Sci.* 1995;36:2327-2331

191. Greenberg JP, Duncker T, Woods RL, Smith RT, Sparrow JR, Delori FC. Quantitative fundus autofluorescence in healthy eyes. *Invest Ophthalmol Vis Sci.* 2013;54:5684-5693

192. Fish G, Grey R, Sehmi KS, Bird AC. The dark choroid in posterior retinal dystrophies. *Br J Ophthalmol.* 1981;65:359-363

193. Uliss AE, Moore AT, Bird AC. The dark choroid in posterior retinal dystrophies. *Ophthalmology.* 1987;94:1423-1427

194. Bonnin MP. [the choroidal silence sign in central tapetoretinal degenerations examined by fluorescein]. *Bull Soc Ophtalmol Fr.* 1971;71:348-351

195. Bonnin MP, Passot M, Triolaire-Cotten T. Le signe du silence choroidien dans les degenerescences tapeto-retiennes posterieures. *Internation Symposium on Fluorescein Angiography* 1976:461–463 Proc Ser

196. Ueda K, Zhao J, Kim HJ, Sparrow JR. Photodegradation of retinal bisretinoids in mouse models and implications for macular degeneration. *Proc Natl Acad Sci U S A.* 2016;113:6904-6909

197. Eagle RC, Jr., Lucier AC, Bernardino VB, Jr., Yanoff M. Retinal pigment epithelial abnormalities in fundus flavimaculatus: A light and electron microscopic study. *Ophthalmology.* 1980;87:1189-1200

198. Rozanowska M, Pawlak A, Rozanowski B, Skumatz C, Zareba M, Boulton ME, Burke JM, Sarna T, Simon JD. Age-related changes in the photoreactivity of retinal lipofuscin granules: Role of chloroform-insoluble components. *Invest Ophthalmol Vis Sci.* 2004;45:1052-1060

199. Feeney-Burns L, Hilderbrand ES, Eldridge S. Aging human rpe: Morphometric analysis of macular, equatorial, and peripheral cells. *Invest Ophthalmol Vis Sci.* 1984;25:195-200

Chapter 5

200. Curcio CA, Sloan KR, Kalina RE, Hendrickson AE. Human photoreceptor topography. *J Comp Neurol.* 1990;292:497-523

201. Dartnall HJ, Bowmaker JK, Mollon JD. Human visual pigments: Microspectrophotometric results from the eyes of seven persons. *Proc R Soc Lond B Biol Sci.* 1983;220:115-130

202. Mahroo OA, Lamb TD. Recovery of the human photopic electroretinogram after bleaching exposures: Estimation of pigment regeneration kinetics. *J Physiol.* 2004;554:417-437

203. Jacques SL. Optical properties of biological tissues: A review. *Phys Med Biol.* 2013;58:R37-61

204. Feldman TB, Yakovleva MA, Arbukhanova PM, Borzenok SA, Kononikhin AS, Popov IA, Nikolaev EN, Ostrovsky MA. Changes in spectral properties and composition of lipofuscin fluorophores from human-retinal-pigment epithelium with age and pathology. *Anal Bioanal Chem.* 2015;407:1075-1088

205. Kurz T, Karlsson M, Brunk UT, Nilsson SE, Frennesson C. Arpe-19 retinal pigment epithelial cells are highly resistant to oxidative stress and exercise strict control over their lysosomal redox-active iron. *Autophagy.* 2009;5:494-501

206. Zareba M, Skumatz CM, Sarna TJ, Burke JM. Photic injury to cultured rpe varies among individual cells in proportion to their endogenous lipofuscin content as modulated by their melanosome content. *Invest Ophthalmol Vis Sci.* 2014;55:4982-4990

207. Qin S, De Vries GW. Alpha2 but not alpha1 amp-activated protein kinase mediates oxidative stress-induced inhibition of retinal pigment epithelium cell phagocytosis of photoreceptor outer segments. *J Biol Chem.* 2008;283:6744-6751

208. Olchawa MM, Herrnreiter AM, Skumatz CM, Zareba M, Sarna TJ, Burke JM. Photosensitized oxidative stress to arpe-19 cells decreases protein receptors that mediate photoreceptor outer segment phagocytosis. *Invest Ophthalmol Vis Sci.* 2013;54:2276-2287

209. Mullen RJ, LaVail MM. Inherited retinal dystrophy: Primary defect in pigment epithelium determined with experimental rat chimeras. *Science.* 1976;192:799-801

210. Zadlo A, Burke JM, Sarna T. Effect of untreated and photobleached bovine rpe melanosomes on the photoinduced peroxidation of lipids. *Photochem Photobiol Sci.* 2009;8:830-837

211. Rozanowski B, Burke JM, Boulton ME, Sarna T, Rozanowska M. Human rpe melanosomes protect from photosensitized and iron-mediated oxidation but become pro-oxidant in the presence of iron upon photodegradation. *Invest Ophthalmol Vis Sci.* 2008;49:2838-2847

212. Rozanowska M, Korytowski W, Rozanowski B, Skumatz C, Boulton ME, Burke JM, Sarna T. Photoreactivity of aged human rpe melanosomes: A comparison with lipofuscin. *Invest Ophthalmol Vis Sci.* 2002;43:2088-2096

213. Winkler BS, Boulton ME, Gottsch JD, Sternberg P. Oxidative damage and age-related macular degeneration. *Mol Vis.* 1999;5:32

214. Feeney L. Lipofuscin and melanin of human retinal pigment epithelium. Fluorescence, enzyme cytochemical, and ultrastructural studies. *Invest Ophthalmol Vis Sci.* 1978;17:583-600

215. Engineering Toolbox T. Common light levels outdoor.2015

216. De Mul FF. Monte-carlo simulations of light scattering and absorption in turbid media, like tissue, including fluorescence, raman, laser-doppler and photo-acoustics. 2016 (www.demul. net/frits; click 'Montcarl')

217. De Mul FF, Koelink MH, Kok ML, Harmsma PJ, Greve J, Graaff R, Aarnoudse JG. Laser doppler velocimetry and monte carlo simulations on models for blood perfusion in tissue. *Appl Opt.* 1995;34:6595-6611

218. De Mul FF. Monte-carlo simulation of light transport in turbid media. In: Tuchin VV, ed. *Handbook of coherent domain optical methods, biomedical diagnostics, environment and material science.* Kluwer Publishers; 2004:465-533.

219. Sarna T, Schwartz HM. The physical properties of melanins. In: Nordlund JJea, ed. *The pigmentary system.* Oxford: Oxford University Press; 1988:posted on (http://omlc.ogi.edu/spectra/melanin/extcoeff.html by S L Jacques).

220. Simon JD, Hong L, Peles DN. Insights into melanosomes and melanin from some interesting spatial and temporal properties. *J Phys Chem B.* 2008;112:13201-13217

221. Zhang QX, Lu RW, Messinger JD, Curcio CA, Guarcello V, Yao XC. In vivo optical coherence tomography of light-driven melanosome translocation in retinal pigment epithelium. *Sci Rep.* 2013;3:2644

222. Weibel ER, Kistler GS, Scherle WF. Practical stereological methods for morphometric cytology. *J Cell Biol.* 1966;30:23-38

223. Sardar DK, Mayo ML, Glickman RD. Optical characterization of melanin. *J Biomed Opt.* 2001;6:404-411

224. Feeney-Burns L, Burns RP, Gao CL. Age-related macular changes in humans over 90 years old. *Am J Ophthalmol.* 1990;109:265-278

225. van de Hulst HC. *Light scattering by small particles.* Dover Publications Inc; 1982.

226. Bohren CF, Huffman DR. *Absorption and scattering of light by small particles.* John Wiley & Sinds Inc.; 1983.

227. Vitkin IA, Woolsey J, Wilson BC, Anderson RR. Optical and thermal characterization of natural (sepia officinalis) melanin. *Photochem Photobiol.* 1994;59:455-462

228. Jacques SL. Http://omlc.Org/spectra/melanin/mua.Html. 1998;2016

229. Zijp JR, ten Bosch JJ. Pascal program to perform mie calculations. *Opt Engin.* 1993;32:1691-1695

230. Ach T, Huisingh C, McGwin G, Jr., Messinger JD, Zhang T, Bentley MJ, Gutierrez DB, Ablonczy Z, Smith RT, Sloan KR, Curcio CA. Quantitative autofluorescence and cell density maps of the human retinal pigment epithelium. *Invest Ophthalmol Vis Sci.* 2014;55:4832-4841

231. Haralampus-Grynaviski NM, Lamb LE, Clancy CM, Skumatz C, Burke JM, Sarna T, Simon JD. Spectroscopic and morphological studies of human retinal lipofuscin granules. *Proc Natl Acad Sci U S A.* 2003;100:3179-3184

232. Linsenmeier RA, Yancey CM. Effects of hyperoxia on the oxygen distribution in the intact cat retina. *Invest Ophthalmol Vis Sci.* 1989;30:612-618

233. Linsenmeier RA, Braun RD. Oxygen distribution and consumption in the cat retina during normoxia and hypoxemia. *J Gen Physiol.* 1992;99:177-197

Chapter 5

234. Rozanowska M, Wessels J, Boulton M, Burke JM, Rodgers MA, Truscott TG, Sarna T. Blue light-induced singlet oxygen generation by retinal lipofuscin in non-polar media. *Free Radic Biol Medi.* 1998;24:1107-1112

235. Curcio CA, Medeiros NE, Millican CL. Photoreceptor loss in age-related macular degeneration. *Invest Ophthalmol Vis Sci.* 1996;37:1236-1249

236. Nagy D, Schonfisch B, Zrenner E, Jagle H. Long-term follow-up of retinitis pigmentosa patients with multifocal electroretinography. *Invest Ophthalmol Vis Sci.* 2008;49:4664-4671

237. Sunness JS, Massof RW, Johnson MA, Bressler NM, Bressler SB, Fine SL. Diminished foveal sensitivity may predict the development of advanced age-related macular degeneration. *Ophthalmology.* 1989;96:375-381

238. Radhakrishnan H, Srinivasan VJ. Compartment-resolved imaging of cortical functional hyperemia with oct angiography. *Biomed Opt Express.* 2013;4:1255–1268

239. Jonnal RS, Rha J, Zhang Y, Cense B, Gao W, Miller DT. In vivo functional imaging of human cone photoreceptors. *Opt Express.* 2007;15:16141-16160

240. Bedggood P, Metha A. Optical imaging of human cone photoreceptors directly following the capture of light. *PLoS One.* 2013;8

241. Rha J, Schroeder B, Godara P, Carroll J. Variable optical activation of human cone photoreceptors visualized using a short coherence light source. *Opt Lett.* 2009;34:3782-3784

242. Elsner AE, Burns SA, Webb RH. Mapping cone photopigment optical density. *J Opt Soc Am A.* 1993;10:52-58

243. Hood DC, Birch DG. Phototransduction in human cones measured using the alpha-wave of the erg. *Vision Res.* 1995;35:2801-2810

244. Friedburg C, Allen CP, Mason PJ, Lamb TD. Contribution of cone photoreceptors and post-receptoral mechanisms to the human photopic electroretinogram. *J Physiol.* 2004;556:819-834

245. Harary HH, Brown JE, Pinto LH. Rapid light-induced changes in near infrared transmission of rods in bufo marinus. *Science.* 1978;202:1083-1085

246. Kuhn H, Bennett N, Michel-Villaz M, Chabre M. Interactions between photoexcited rhodopsin and gtp-binding protein: Kinetic and stoichiometric analyses from light-scattering changes. *Proc Natl Acad Sci U S A.* 1981;78:6873-6877

247. Zawadzki RJ, Jones SM, Olivier SS, Zhao M, Bower BA, Izatt JA, Choi S, Laut S, Werner JS. Adaptive-optics optical coherence tomography for high-resolution and high-speed 3d retinal in vivo imaging. *Opt Express.* 2005;13:8532-8546

248. Srinivasan VJ, Chen Y, Duker JS, Fujimoto JG. In vivo functional imaging of intrinsic scattering changes in the human retina with high-speed ultrahigh resolution oct. *Opt Express.* 2009;17:3861-3877

249. Schmoll T, Kolbitsch C, Leitgeb RA. In vivo functional retinal optical coherence tomography. *J Biomed Opt.* 2010;15:041513

250. Grieve K, Roorda A. Intrinsic signals from human cone photoreceptors. *Invest Ophthalmol Vis Sci.* 2008;49:713-719

251. Tumlinson AR, Hermann B, Hofer B, Povazay B, Margrain TH, Binns AM, Drexler W. Techniques for extraction of depth-resolved in vivo human retinal intrinsic optical signals with optical coherence tomography. *Jpn J Ophthalmol.* 2009;53:315-326

252. Theelen T, Hoyng CB, Klevering BJ, Cense B. Functional imaging of inherited retinal disease with a commercial optical coherence tomography device. *Progress in Biomedical Optics and Imaging.* 2011;12:80911O-80911 -80918

253. Bedggood P, Metha A. Variability in bleach kinetics and amount of photopigment between individual foveal cones. *Invest Ophthalmol Vis Sci.* 2012;53:3673-3681

254. Hodgkin AL, Obryan PM. Internal recording of the early receptor potential in turtle cones. J *Physiol.* 1977;267:737-766

255. Imai H, Imamoto Y, Yoshizawa T, Shichida Y. Difference in molecular properties between chicken green and rhodopsin as related to the functional difference between cone and rod photoreceptor cells. *Biochemistry.* 1995;34:10525-10531

256. Imai H, Terakita A, Tachibanaki S, Imamoto Y, Yoshizawa T, Shichida Y. Photochemical and biochemical properties of chicken blue-sensitive cone visual pigment. *Biochemistry.* 1997;36:12773-12779

257. Yoshizawa T. Molecular basis for color vision. *Biophysical chemistry.* 1994;50:17-24

258. Vought BW, Dukkipatti A, Max M, Knox BE, Birge RR. Photochemistry of the primary event in short-wavelength visual opsins at low temperature. *Biochemistry.* 1999;38:11287-11297

259. Kusnetzow A, Dukkipati A, Babu KR, Singh D, Vought BW, Knox BE, Birge RR. The photobleaching sequence of a short-wavelength visual pigment. *Biochemistry.* 2001;40:7832-7844

260. Yao XC, Yamauchi A, Perry B, George JS. Rapid optical coherence tomography and recording functional scattering changes from activated frog retina. *Appl Opt.* 2005;44:2019-2023

261. Bizheva K, Pflug R, Hermann B, Povazay B, Sattmann H, Qiu P, Anger E, Reitsamer H, Popov S, Taylor JR, Unterhuber A, Ahnelt P, Drexler W. Optophysiology: Depth-resolved probing of retinal physiology with functional ultrahigh-resolution optical coherence tomography. *P Natl Acad Sci USA.* 2006;103:5066-5071

262. Jonnal RS, Kocaoglu OP, Wang Q, Lee S, Miller DT. Phase-sensitive imaging of the outer retina using optical coherence tomography and adaptive optics. *Biomed Opt Express.* 2012;3:104-124

263. Schneeweis DM, Schnapf JL. Photovoltage of rods and cones in the macaque retina. *Science.* 1995;268:1053-1056

264. Hill BC, Schubert ED, Nokes MA, Michelson RP. Laser interferometer measurement of changes in crayfish axon diameter concurrent with action potential. *Science.* 1977;196:426-428

265. Tasaki I, Byrne PM. Rapid mechanical changes in the amphibian retina evoked by brief light pulses. *Biochem Biophys Res Commun.* 1987;143:93-97

266. Tasaki I, Nakaye T. Rapid mechanical responses of the dark-adapted squid retina to light pulses. *Science.* 1984;223:411-413

267. Heck M, Pulvermuller A, Hofmann KP. Light scattering methods to monitor interactions between rhodopsin-containing membranes and soluble proteins. *Methods Enzymol.* 2000;315:329-347

Chapter 5

268. Korenbrot JI. Speed, sensitivity, and stability of the light response in rod and cone photoreceptors: Facts and models. *Prog Retin Eye Res.* 2012;31:442-466

269. Leskov IB, Klenchin VA, Handy JW, Whitlock GG, Govardovskii VI, Bownds MD, Lamb TD, Pugh EN, Jr., Arshavsky VY. The gain of rod phototransduction: Reconciliation of biochemical and electrophysiological measurements. *Neuron.* 2000;27:525-537

270. Bizheva K, Pflug R, Gasparoni S, Hermann B, Sattmann H, Anger E, Popov S, Reitsamer H, Ahnelt P, Drexler W. Optophysiology - spatially resolved optical probing of retinal physiology with functional ultrahigh resolution optical coherence tomography. *Invest Ophth Vis Sci.* 2005;46:5066-5071

271. Moayed AA, Hariri S, Choh V, Bizheva K. In vivo imaging of intrinsic optical signals in chicken retina with functional optical coherence tomography. *Opt Lett.* 2011;36:4575-4577

272. Yao XC, George JS. Near-infrared imaging of fast intrinsic optical responses in visible light-activated amphibian retina. *J Biomed Opt.* 2006;11:064030

273. Wang B, Lu R, Zhang Q, Jiang Y, Yao X. En face optical coherence tomography of transient light response at photoreceptor outer segments in living frog eyecup. *Opt Lett.* 2013;38:4526-4529

274. Yao XC. Intrinsic optical signal imaging of retinal activation. *Jpn J Ophthalmol.* 2009;53:327-333

275. Brown RL, Lynch LL, Haley TL, Arsanjani R. Pseudechetoxin binds to the pore turret of cyclic nucleotide-gated ion channels. *J Gen Physiol.* 2003;122:749-760

276. Ricco S, Chen M, Ishikawa H, Wollstein G, Schuman J. Correcting motion artifacts in retinal spectral domain optical coherence tomography via image registration. *Med Image Comput Comput Assist Interv.* 2009;12:100-107

277. Yun S, Tearney G, Bouma B, Park B, de Boer J. High-speed spectral-domain optical coherence tomography at 1.3 mum wavelength. *Opt Express.* 2003;11:3598-3604

278. Yun SH, Tearney G, de Boer J, Bouma B. Motion artifacts in optical coherence tomography with frequency-domain ranging. *Opt Express.* 2004;12:2977-2998

279. Klein T, Wieser W, Reznicek L, Neubauer A, Kampik A, Huber R. Multi-mhz retinal oct. *Biomed Opt Express.* 2013;4:1890-1908

280. Martinez-Conde S, Macknik SL, Hubel DH. The role of fixational eye movements in visual perception. *Nature reviews. Neuroscience.* 2004;5:229-240

281. Podoleanu A, Charalambous I, Plesea L, Dogariu A, Rosen R. Correction of distortions in optical coherence tomography imaging of the eye. *Phys Med Biol.* 2004;49:1277-1294

282. Kocaoglu OP, Ferguson RD, Jonnal RS, Liu Z, Wang Q, Hammer DX, Miller DT. Adaptive optics optical coherence tomography with dynamic retinal tracking. *Biomed Opt Express.* 2014;5:2262-2284

283. Braaf B, Vienola KV, Sheehy CK, Yang Q, Vermeer KA, Tiruveedhula P, Arathorn DW, Roorda A, de Boer JF. Real-time eye motion correction in phase-resolved oct angiography with tracking slo. *Biomed Opt Express.* 2013;4:51-65

284. Jonnal RS, Migacz JV, Zawadzki RJ, Lee HS, Werner JS. Afocal ao-oct image quality improvements through 3d registration and averaging. Presented at ARVO 2014; Orlando, FL. May 2014

285. Bedggood P, Daaboul M, Ashman R, Smith G, Metha A. Characteristics of the human isoplanatic patch and implications for adaptive optics retinal imaging. *J Biomed Opt.* 2008;13:024008

286. Moller F, Laursen ML, Tygesen J, Sjolie AK. Binocular quantification and characterization of microsaccades. *Graefes Arch Clin Exp Ophthalmol.* 2002;240:765-770

287. Thaler L, Schutz AC, Goodale MA, Gegenfurtner KR. What is the best fixation target? The effect of target shape on stability of fixational eye movements. *Vision Res.* 2013;76:31-42

288. Moller F, Sjolie AK, Bek T. Quantitative assessment of fixational eye movements by scanning laser ophthalmoscopy. *Acta Ophthalmol Scand.* 1996;74:578-583

289. Collewijn H, van der Mark F, Jansen TC. Precise recording of human eye movements. *Vision Res.* 1975;15:447-450

290. Miller DT, Williams DR, Morris GM, Liang J. Images of cone photoreceptors in the living human eye. *Vision Res.* 1996;36:1067-1079

291. Potsaid B, Gorczynska I, Srinivasan VJ, Chen Y, Jiang J, Cable A, Fujimoto JG. Ultrahigh speed spectral / fourier domain oct ophthalmic imaging at 70,000 to 312,500 axial scans per second. *Opt Express.* 2008;16:15149-15169

292. Stiles WS, Crawford BH. The luminous efficiency of rays entering the eye pupil at different points. *P Roy Soc Lond B Bio.* 1933;112:428-450

293. Laties AM, Enoch JM. An analysis of retinal receptor orientation. I. Angular relationship of neighboring photoreceptors. *Invest Ophthalmol.* 1971;10:69-77

294. Burns SA, Wu S, Delori F, Elsner AE. Direct measurement of human-cone-photoreceptor alignment. *J Opt Soc Am A Opt Image Sci Vis.* 1995;12:2329-2338

295. Gorrand JM, Delori F. A method for assessing the photoreceptor directionality. *Invest Ophthalmol Vis Sci.* 1990;4:425

296. Delint PJ, Berendschot TT, van Norren D. Local photoreceptor alignment measured with a scanning laser ophthalmoscope. *Vision Res.* 1997;37:243-248

297. Gao W, Cense B, Zhang Y, Jonnal RS, Miller DT. Measuring retinal contributions to the optical stiles-crawford effect with optical coherence tomography. *Opt Express.* 2008;16:6486-6501

298. DeLint PJ, Berendschot TT, van de Kraats J, van Norren D. Slow optical changes in human photoreceptors induced by light. *Invest Ophthalmol Vis Sci.* 2000;41:282-289

299. Zagers NP, Berendschot TT, van Norren D. Wavelength dependence of reflectometric cone photoreceptor directionality. *J Opt Soc Am A Opt Image Sci Vis.* 2003;20:18-23

300. Westheimer G. Dependence of the magnitude of the stiles-crawford effect on retinal location. *J Physiol.* 1967;192:309-315

301. Vermeer KA, Mo J, Weda JJ, Lemij HG, de Boer JF. Depth-resolved model-based reconstruction of attenuation coefficients in optical coherence tomography. *Biomed Opt Express.* 2013;5:322-337

302. Lim Y, Cense B. Motion correction in doppler optical coherence tomography using a line scanning laser ophthalmoscope based active retinal tracker. *Optics & Photonics Japan, Nara, Japan.* 2013

303. Mayer M, Sheets K. Optical coherence tomography segmentation and evaluation gui (version 0.1). *Available at http://www5.cs.fau.de/research/software/octseg/.*

Chapter 5

304. Grulkowski I, Liu JJ, Potsaid B, Jayaraman V, Lu CD, Jiang J, Cable AE, Duker JS, Fujimoto JG. Retinal, anterior segment and full eye imaging using ultrahigh speed swept source oct with vertical-cavity surface emitting lasers. *Biomed Opt Express.* 2012;3:2733-2751

305. Zhang QQ, Wu XJ, Tang T, Zhu SW, Yao Q, Gao BZ, Yuan XC. Quantitative analysis of rectal cancer by spectral domain optical coherence tomography. *Phys Med Biol.* 2012;57:5235-5244

306. Faber D, van der Meer F, Aalders M, van Leeuwen T. Quantitative measurement of attenuation coefficients of weakly scattering media using optical coherence tomography. *Opt Express.* 2004;12:4353-4365

307. Sardar DK, Salinas FS, Perez JJ, Tsin AT. Optical characterization of bovine retinal tissues. *J Biomed Opt.* 2004;9:624-631

308. Shih YY, De la Garza BH, Muir ER, Rogers WE, Harrison JM, Kiel JW, Duong TQ. Lamina-specific functional mri of retinal and choroidal responses to visual stimuli. *Invest Ophthalmol Vis Sci.* 2011;52:5303-5310

309. Ts'o D, Schallek J, Kwon Y, Kardon R, Abramoff M, Soliz P. Noninvasive functional imaging of the retina reveals outer retinal and hemodynamic intrinsic optical signal origins. *Jpn J Ophthalmol.* 2009;53:334-344

310. Liew G, Quin G, Gillies M, Fraser-Bell S. Central serous chorioretinopathy: A review of epidemiology and pathophysiology. *Clin Experiment Ophthalmol.* 2013;41:201-214

311. Wang M, Munch IC, Hasler PW, Prunte C, Larsen M. Central serous chorioretinopathy. *Acta Ophthalmol.* 2008;86:126-145

312. Nicholson B, Noble J, Forooghian F, Meyerle C. Central serous chorioretinopathy: Update on pathophysiology and treatment. *Surv Ophthalmol.* 2013;58:103-126

313. Gemenetzi M, De Salvo G, Lotery AJ. Central serous chorioretinopathy: An update on pathogenesis and treatment. *Eye (Lond).* 2010;24:1743-1756

314. Yannuzzi LA. Central serous chorioretinopathy: A personal perspective. *Am J Ophthalmol.* 2010;149:361-363

315. Maaranen TH, Tuppurainen KT, Mantyjarvi MI. Color vision defects after central serous chorioretinopathy. *Retina.* 2000;20:633-637

316. de Jong EK, Breukink MB, Schellevis RL, Bakker B, Mohr JK, Fauser S, Keunen JE, Hoyng CB, den Hollander AI, Boon CJ. Chronic central serous chorioretinopathy is associated with genetic variants implicated in age-related macular degeneration. *Ophthalmology.* 2015;122:562-570

317. Miki A, Kondo N, Yanagisawa S, Bessho H, Honda S, Negi A. Common variants in the complement factor h gene confer genetic susceptibility to central serous chorioretinopathy. *Ophthalmology.* 2014;121:1067-1072

318. Gass JD. Pathogenesis of disciform detachment of the neuroepithelium. *Am J Ophthalmol.* 1967;63:Suppl:1-139

319. Prunte C, Flammer J. Choroidal capillary and venous congestion in central serous chorioretinopathy. *Am J Ophthalmol.* 1996;121:26-34

320. Spaide RF, Hall L, Haas A, Campeas L, Yannuzzi LA, Fisher YL, Guyer DR, Slakter JS, Sorenson JA, Orlock DA. Indocyanine green videoangiography of older patients with central serous chorioretinopathy. *Retina.* 1996;16:203-213

321. Guyer DR, Yannuzzi LA, Slakter JS, Sorenson JA, Ho A, Orlock D. Digital indocyanine green videoangiography of central serous chorioretinopathy. *Arch Ophthalmol.* 1994;112:1057-1062

322. Eandi CM, Ober M, Iranmanesh R, Peiretti E, Yannuzzi LA. Acute central serous chorioretinopathy and fundus autofluorescence. *Retina.* 2005;25:989-993

323. Loo RH, Scott IU, Flynn HW, Jr., Gass JD, Murray TG, Lewis ML, Rosenfeld PJ, Smiddy WE. Factors associated with reduced visual acuity during long-term follow-up of patients with idiopathic central serous chorioretinopathy. *Retina.* 2002;22:19-24

324. Wang MS, Sander B, Larsen M. Retinal atrophy in idiopathic central serous chorioretinopathy. *Am J Ophthalmol.* 2002;133:787-793

325. Yoshioka H, Katsume Y, Akune H. Experimental central serous chorioretinopathy in monkey eyes: Fluorescein angiographic findings. *Ophthalmologica.* 1982;185:168-178

326. Yoshioka H, Katsume Y. Experimental central serous chorioretinopathy. Iii: Ultrastructural findings. *Jpn J Ophthalmol.* 1982;26:397-409

327. Kitaya N, Nagaoka T, Hikichi T, Sugawara R, Fukui K, Ishiko S, Yoshida A. Features of abnormal choroidal circulation in central serous chorioretinopathy. *Br J Ophthalmol.* 2003;87:709-712

328. Liegl R, Ulbig MW. Central serous chorioretinopathy. *Ophthalmologica.* 2014;232:65-76

329. Spaide RF, Klancnik JM, Jr., Cooney MJ. Retinal vascular layers in macular telangiectasia type 2 imaged by optical coherence tomographic angiography. *JAMA Ophthalmol.* 2015;133:66-73

330. Jia Y, Bailey ST, Wilson DJ, Tan O, Klein ML, Flaxel CJ, Potsaid B, Liu JJ, Lu CD, Kraus MF, Fujimoto JG, Huang D. Quantitative optical coherence tomography angiography of choroidal neovascularization in age-related macular degeneration. *Ophthalmology.* 2014;121:1435-1444

331. de Carlo TE, Bonini Filho MA, Chin AT, Adhi M, Ferrara D, Baumal CR, Witkin AJ, Reichel E, Duker JS, Waheed NK. Spectral-domain optical coherence tomography angiography of choroidal neovascularization. *Ophthalmology.* 2015;122:1228-1238

332. Bonini Filho MA, de Carlo TE, Ferrara D, Adhi M, Baumal CR, Witkin AJ, Reichel E, Duker JS, Waheed NK. Association of choroidal neovascularization and central serous chorioretinopathy with optical coherence tomography angiography. *JAMA Ophthalmol.* 2015

333. Scheider A, Nasemann JE, Lund OE. Fluorescein and indocyanine green angiographies of central serous choroidopathy by scanning laser ophthalmoscopy. *Am J Ophthalmol.* 1993;115:50-56

334. Holz FG, Jorzik J, Schutt F, Flach U, Unnebrink K. Agreement among ophthalmologists in evaluating fluorescein angiograms in patients with neovascular age-related macular degeneration for photodynamic therapy eligibility (flap-study). *Ophthalmology.* 2003;110:400-405

335. Nishiyama Y, Mori K, Murayama K, Yoneya S. Quantitative analysis of indocyanine green angiographic image in central serous chorioretinopathy. *Jpn J Ophthalmol.* 2001;45:116

336. Iida T, Kishi S, Hagimura N, Shimizu K. Persistent and bilateral choroidal vascular abnormalities in central serous chorioretinopathy. *Retina.* 1999;19:508-512

Chapter 5

337. Ferrara D, Mohler KJ, Waheed N, Adhi M, Liu JJ, Grulkowski I, Kraus MF, Baumal C, Hornegger J, Fujimoto JG, Duker JS. En face enhanced-depth swept-source optical coherence tomography features of chronic central serous chorioretinopathy. *Ophthalmology.* 2014;121:719-726

338. Uyama M, Matsunaga H, Matsubara T, Fukushima I, Takahashi K, Nishimura T. Indocyanine green angiography and pathophysiology of multifocal posterior pigment epitheliopathy. *Retina.* 1999;19:12-21

339. Hussain D, Gass JD. Idiopathic central serous chorioretinopathy. *Indian J Ophthalmol.* 1998;46:131-137

340. Slakter JS, Yannuzzi LA, Guyer DR, Sorenson JA, Orlock DA. Indocyanine-green angiography. *Curr Opin Ophthalmol.* 1995;6:25-32

341. Karakus SH, Basarir B, Pinarci EY, Kirandi EU, Demirok A. Long-term results of half-dose photodynamic therapy for chronic central serous chorioretinopathy with contrast sensitivity changes. *Eye (Lond).* 2013;27:612-620

342. Koytak A, Erol K, Coskun E, Asik N, Ozturk H, Ozerturk Y. Fluorescein angiography-guided photodynamic therapy with half-dose verteporfin for chronic central serous chorioretinopathy. *Retina.* 2010;30:1698-1703

343. Brinkmann R, Schule G, Neumann J, Framme C, Porksen E, Elsner H, Theisen-Kunde D, Roider J, Birngruber R. [selective retina therapy: Methods, technique, and online dosimetry]. *Ophthalmologe.* 2006;103:839-849

344. Klatt C, Saeger M, Oppermann T, Porksen E, Treumer F, Hillenkamp J, Fritzer E, Brinkmann R, Birngruber R, Roider J. Selective retina therapy for acute central serous chorioretinopathy. *Br J Ophthalmol.* 2011;95:83-88

345. Smith RT, Koniarek JP, Chan J, Nagasaki T, Sparrow JR, Langton K. Autofluorescence characteristics of normal foveas and reconstruction of foveal autofluorescence from limited data subsets. *Invest Ophthalmol Vis Sci.* 2005;46:2940-2946

346. Hwang JC, Chan JW, Chang S, Smith RT. Predictive value of fundus autofluorescence for development of geographic atrophy in age-related macular degeneration. *Invest Ophthalmol Vis Sci.* 2006;47:2655-2661

347. Taylor HR, West S, Munoz B, Rosenthal FS, Bressler SB, Bressler NM. The long-term effects of visible light on the eye. *Arch Ophthalmol.* 1992;110:99-104

348. Tomany SC, Cruickshanks KJ, Klein R, Klein BE, Knudtson MD. Sunlight and the 10-year incidence of age-related maculopathy: The beaver dam eye study. *Arch Ophthalmol.* 2004;122:750-757

349. Delcourt C, Carriere I, Ponton-Sanchez A, Fourrey S, Lacroux A, Papoz L, Group PS. Light exposure and the risk of age-related macular degeneration: The pathologies oculaires liees a l'age (pola) study. *Arch Ophthalmol.* 2001;119:1463-1468

350. Rozanowska M, Rozanowski B, Boulton M. Photobiology of the retina: Light-induced damage to the retina. *Photobiological Sciences* 2009;2015

351. Rozanowska MB. Light-induced damage to the retina: Current understanding of the mechanisms and unresolved questions: A symposium-in-print. *Photochem Photobiol.* 2012;88:1303-1308

352. Kono M, Enoch JM, Strada E, Shih P, Srinivasan R, Lakshminarayanan V, Susilasate W, Graham A. Stiles-crawford effect of the first kind: Assessment of photoreceptor alignments following dark patching. *Vision Res.* 2001;41:103-118

353. Westheimer G. Directional sensitivity of the retina: 75 years of stiles-crawford effect. *Proc Biol Sci.* 2008;275:2777-2786

354. Symes R, Young M, Forooghian F. Quantitative assessment of retinal degeneration in birdshot chorioretinopathy using optical coherence tomography. *Ophthalmic Surg Lasers Imaging Retina.* 2015;46:1009-1012

355. Terman A, Brunk UT. Lipofuscin. *Int J Biochem Cell Biol.* 2004;36:1400-1404

356. Knorr HL, Linde-Behringer M, Gossler B, Mayer UM. Human retinal pigment epithelium in vitro: Influence of low oxygen tension, glucose and insulin. *Ophthalmic Res.* 1993;25:226-234

357. Nash RW, McKay BS, Burke JM. The response of cultured human retinal pigment epithelium to hypoxia: A comparison to other cell types. *Invest Ophthalmol Vis Sci.* 1994;35:2850-2856

358. Yao X, Wang B. Intrinsic optical signal imaging of retinal physiology: A review. *J Biomed Opt.* 2015;20:090901

359. Zhang Q, Lu R, Wang B, Messinger JD, Curcio CA, Yao X. Functional optical coherence tomography enables in vivo physiological assessment of retinal rod and cone photoreceptors. *Sci Rep.* 2015;5:9595

360. Hillmann D, Spahr H, Pfaeffle C, Sudkamp H, Frank G, Huettmann G. In vivo optical imaging of physiological responses to photostimulation in human photoreceptors. *Proc Natl Acad Sci USA.* 2016

361. Costanzo E, Cohen SY, Miere A, Querques G, Capuano V, Semoun O, El Ameen A, Oubraham H, Souied EH. Optical coherence tomography angiography in central serous chorioretinopathy. *J Ophthalmol.* 2015;2015:134783

362. Hage R, Mrejen S, Krivosic V, Quentel G, Tadayoni R, Gaudric A. Flat irregular retinal pigment epithelium detachments in chronic central serous chorioretinopathy and choroidal neovascularization. *Am J Ophthalmol.* 2015;159:890-903 e893

363. Tokayer J, Jia Y, Dhalla AH, Huang D. Blood flow velocity quantification using split-spectrum amplitude-decorrelation angiography with optical coherence tomography. *Biomed Opt Express.* 2013;4:1909-1924

364. Spaide RF, Fujimoto JG, Waheed NK. Image artifacts in optical coherence tomography angiography. *Retina.* 2015;35:2163-2180

365. Zhang A, Zhang Q, Wang RK. Minimizing projection artifacts for accurate presentation of choroidal neovascularization in oct micro-angiography. *Biomed Opt Express.* 2015;6:4130-4143

366. Wang Y, Chen ZQ, Wang W, Fang XY. Multimodal imaging evaluations of focal choroidal excavations in eyes with central serous chorioretinopathy. *J Ophthalmol.* 2016;2016:7073083

367. Chan WM, Lam DS, Lai TY, Tam BS, Liu DT, Chan CK. Choroidal vascular remodelling in central serous chorioretinopathy after indocyanine green guided photodynamic therapy with verteporfin: A novel treatment at the primary disease level. *Br J Ophthalmol.* 2003;87:1453-1458

Chapter 5

Chapter 6.

Summary

The progression of retinal diseases is often gradual with subtle changes. These local alterations become more prominent during the development of the disease. Accurate measurements of the early changes, based on imaging techniques sensitive enough to the detect them, can help to provide better insight into the pathophysiology, to evaluate effects of treatment and to provide a better prognosis. This thesis describes disease-associated changes in retinal scans (imaging biomarkers), the expansion speed of changes, and their correlation with the disease process.

In **Chapter 2**, three studies are described that were mainly conducted with fundus autofluorescence (FAF). It includes an analysis of any safety risks of the bright light that is used in this technique. **Chapter 2.1** presents the results of an FAF-based study on the long-term effects of light exposure in patients with Stargardt disease (STGD1). Five patients with the diagnosis STGD1 wore a black contact lens to nearly completely shield their subjectively most functional eye from visible light, during a minimum of one year except while sleeping. The retrospective image analysis of FAF was performed with a semiautomatic system that had been validated previously in patients with AMD or STGD1. Abnormal FAF was measured as focally increased (FIAF), -decreased (FDAF), or as being essentially absent (geographic atrophy, GA) on a per-pixel basis. An analysis of the rate of expansion of these pixel populations shows that FIAF differed neither consistently nor significantly between the light-protected and –exposed eyes. FDAF, on the contrary, expanded more rapidly in the light exposed eye of 4 out of 5 patients; in these 4 patients the rate of expansion was, on average, 53% lower in the treated eye. The remaining patient had early-onset STGD1, which is typically associated with a significantly worse prognosis. The decreased rate of expansion of FDAF suggests that the normal daily light exposure can accelerate the occurrence of damage to the retinal pigment epithelium (RPE). This study therefore supports the clinical advice given to patients with STGD1 to limit intraocular exposure to light.

Chapter 2.2 describes a quantitative, retrospective study on the development and progression of diverse (chorio-)retinal lesions in patients with birdshot chorioretinopathy (BCR), in relation to the activity of retinal inflammation. The added value of FAF imaging in the monitoring of the disease progression of BCR was also investigated. We used optical coherence tomography (OCT) to obtain a fuller picture of the lesions' identity and their progression. The inflammatory activity was evaluated based on fluorescein angiography (FAG) and indocyanine green angiography (ICGA). Active retinal inflammation was defined as an observation of inflammatory activity on FAG together with a decision to maintain or intensity treatment by the treating physician. In 9 out of 21 patients (43%), we found at least of the following lesions in the photoreceptors or RPE: circular chorioretinal lesions on FAF and OCT; disruption of the ellipsoid zone on OCT; and RPE-atrophy on FAF and OCT. A disruption of the ellipsoid zone was the most frequent observation of these lesion types (7 out of 21 patients, 33%). Comparative image analysis of FAF and OCT showed an excellent spatial

correspondence between hyperfluorescent areas on FAF and disruption of the ellipsoid zone on OCT. A partial or complete restoration of this zone was also found in 4 out of 7 patients, which was contemporary with a visually evident reduction in retinal inflammatory activity subsequent to the intensification of treatment. This study illustrates the clinical presentation of patients with BCR, it specifies the spectrum of retinal lesions, and it offer insight into the progression of these lesions. Monitoring disruptions in the ellipsoid zone of photoreceptors can help to determine anatomical improvements, even in the case of chronic disease.

Chapter 2.3 continues the work presented in Chapter 2.1, and describes a numerical simulation of oxidative stress in the RPE as a consequence of exposure to sunlight or to the excitation laser of FAF. We compared this stress between healthy individuals and patients with STGD1, which provided us with an indication of the degree with which accumulated RPE lipofuscin potentially sensitizes these patients to light exposure. The simulation consists of 3 main factors that determine the quantity of light absorbed by lipofuscin, as well as a factor that relates this light absorption to oxygen consumption—this oxygen consumption is an indicator of the production of oxygen radicals and therefore of oxidative stress. The light intensity on the retinal was calculated first: the yearly average radiance of diffuse sunlight (λ = 380-700 nm) and the constant intensity of the FAF excitation laser (λ = 488 nm) were corrected for the age-dependent optical attenuation by the ocular lens and media. Second, light attenuation by melanin in the pigment epithelial monolayer was simulated with a Monte-Carlo simulation: this factor was dependent on age and wavelength, although the total attenuation was only 11% on average. In patients with STGD1, this optical attenuation was found to be reduced by about 50% relative to age-matched controls. Third, light absorption by lipofuscin granules in the RPE was calculated based on the strong correlation between histologic data and the calibrated FAF-intensity. Based on the linear relationship between these factors and by extrapolation, we calculated that light absorption by lipofuscin is increased by 3-fold and 2-fold in patients with STGD1 relative to that in 20- and 60-year old controls, respectively. Interestingly, we found no age-dependent increase in oxygen uptake during daylight in healthy controls whereas this increase was found during FAF-imaging. The oxygen uptake during both daylight and FAF imaging was increased 3-fold. Future research ought to determine how well this simulation approaches the actual situation, as well as the implications of the calculated increases in oxygen uptake in STGD1. The 1.3-fold increase in oxidative stress during FAF may exceed the anti-oxidative capacity of the RPE during the short duration of an FAF imaging session, although it is at present unclear whether this can lead to damage to the RPE or the photoreceptors.

Chapter 3 describes two investigations that were performed with OCT. In **Chapter 3.1**, we performed a theoretical and practical analysis of motion-associated noise factors, which affect measurements of phototransduction-associated intrinsic optical signals (IOS) that are based on the amplitude reflectivity of tissue measured by spectral-domain OCT (SD-

Chapter 6

OCT). We also investigated the literature for the biophysical underpinnings of IOS. Based first on partial inconsistencies between the IOS signal duration and a causal mechanism postulated previously—osmotic swelling of photoreceptor outer segments, and second based on light-scattering boundaries in these outer segments, we proposed that local activity of phosphodiesterase (PDE) could be a underlying mechanism for IOS. Both could evoke changes in the optical path length between the inner/outer-segment (IS/OS-) junction of photoreceptors and the tips of outer segments (OS tips). Four factors need to be taken into account in order to enable in-vivo measurements of IOS based on the reflectivity-amplitude. IOS of adjacent photoreceptors can have opposite signal polarity; the prevention of crosstalk necessitates cellular resolution, a high image-acquisition speed, and image stabilization by means of image registration or active retinal tracking. In order to prevent large-scale fluctuations in the reflectivity-amplitude of cone photoreceptors due to the optical Stiles-Crawford effect, it is crucial to align the optical axis of the imaging system with the peak of the Stiles-Crawford function by performing pupil-centred measurements. Fluctuations in signal amplitude can also be caused by movements of the sample along the optical systems' optical axis, which is caused by an exponential dependence of the sensitivity of SD-OCT and the optical path length between sample and detector ('sensitivity fall-off'). In case of our SD-OCT, this factor can explain 29% of the variability in signal amplitude during IOS-measurements. A correction of this effect is possible by a separate measurement and subsequent Gaussian fitting. Finally, we described an algorithm that specifically addresses highly variable illumination in M-B scans, which enables a reduction of signal variability to within a variation coefficient of 6.9%. Recent developments by other authors have led to a specific OCT that is capable of measuring IOS-associated changes in the optical path length of photoreceptor outer segments. We expect that this technique will soon prove to be clinically feasible to detect the presence of functional photoreceptors in-vivo, primarily because this phase-sensitive technique is insensitive to the noise factors that we assessed, and because better insights have been gained regarding the biophysical underpinnings of this type of IOS.

Chapter 3.2 presents a study on patients with chronic serous chorioretinopathy (CSC) in which signs of abnormal blood perfusion were compared among different angiographic techniques, including OCT-angiography (OCTA), FAG, and ICGA. This multi-modal imaging was performed on the same day to maximize the comparability of morphology. Two clinical researchers demarcated areas of perceived abnormalities in these images. The spatial overlap of annotated areas was measured in terms of Jaccard indices (JIs). Most abnormalities were annotated in late-phase ICGA-scans (>15 min post-injection of ICGA) and on OCTA of the choriocapillaris, with high (median JI, 0.74) and average (median JI, 0.52) inter-observer agreement. The annotated areas on OCTA of the choriocapillaris frequently exhibited focal areas of decreased flow surrounded by an increased density of flow. Hotspots on ICGA were in close proximity of areas of decreased flow on OCTA of the choriocapillaris (mean distance, 168 μm). Areas with current or former subretinal fluid were co-located

with flow abnormalities. This study showed that CSC exhibits frequent, yet relatively subtle, aberrant perfusion patterns that were not characterized in other studies. The hyperdense blood perfusion surrounding focal areas of decreased flow can be explained by reactive hyperperfusion—a suggestion that is supported by findings in a recent study with comparable perfusion patterns. This hyperperfusion may be cause of leakage, causing ischemic damage to the RPE which may disrupt the barrier function of the RPE.

The studies described in this thesis show how various relatively subtle imaging biomarkers correlated with retinal and choroidal (patho-)physiology, and with the development and progression of retinal diseases. This has led to new insights into the disease process of STGD1, BCR, and chronic CSC. Measurements of these biomarkers can be performed in order to quantify the progression of important retinal diseases, which can be correlated with genetics, environmental factors, and treatments.

Chapter 6

Chapter 7.

Samenvatting

De ziekteprogressie van netvliesaandoeningen is vaak vrij geleidelijk met subtiele veranderingen. Deze lokale veranderingen worden steeds duidelijker tijdens de ontwikkeling van de ziekte. Nauwkeurige metingen van de vroege veranderingen, gebaseerd op beeldvormingstechnieken die gevoelig genoeg zijn hiervoor, kunnen helpen om beter inzicht te verschaffen in het ziekteproces, om behandeleffecten te evalueren en om de prognose beter in te schatten. Dit proefschrift beschrijft ziekte-geassocieerde veranderingen in scans van het netvlies (imaging biomarkers), de snelheid waarmee veranderingen zich uitbreiden, en hun relatie met het ziekteproces.

In **Hoofdstuk 2** worden drie onderzoeken beschreven die met name verricht zijn met fundus autofluorescentie (FAF). Ook worden eventuele veiligheidsrisico's van het felle licht dat bij deze techniek gebruikt wordt geanalyseerd. **Hoofdstuk 2.1** presenteert de resultaten van een onderzoek op basis van FAF, naar de lange termijn effecten van lichtblootstelling bij patiënten met de ziekte van Stargardt (STGD1). Vijf patiënten met de diagnose STGD1 droegen een zwarte contactlens om hun subjectief meest functionele oog vrijwel volledig af te schermen voor zichtbaar licht, gedurende minimaal één jaar behalve tijdens het slapen. De retrospectieve beeldanalyse van FAF werd uitgevoerd met een semiautomatisch systeem dat eerder gevalideerd was bij patiënten met AMD of STGD1. Per pixel werd abnormale FAF gemeten als focaal toegenomen (FIAF), afgenomen (FDAF), en nagenoeg afwezige FAF (geografische atrofie, GA) gedetecteerd. Analyse van de expansiesnelheid van deze pixel populaties laat zien dat FIAF noch consistent noch significant verschilde tussen het licht-afgeschermde en blootgestelde oog. FDAF echter breidde zich sneller uit in het blootgestelde oog bij 4 van de 5 patiënten; bij hen was deze snelheid gemiddeld 53% lager in het behandelde oog. Bij de overige patiënt was sprake van early-onset STGD1, waarbij de prognose doorgaans veel slechter is. De afgenomen expansiesnelheid van FDAF suggereert dat de normale dagelijkse lichtbelasting het optreden van schade in het pigmentepitheel RPE) kan versnellen. Deze studie onderschrijft daarom het advies aan patiënten met STGD1 om intra-oculaire blootstelling aan licht te beperken.

Hoofdstuk 2.2 beschrijft een kwalitatief, retrospectief onderzoek naar de ontwikkeling en progressie van diverse (chorio-) retinale lesies bij patiënten met birdshot chorioretinopathie (BCR), in relatie tot de ontstekingsactiviteit in het netvlies. Tevens werd onderzocht welke toegevoegde waarde FAF heeft bij het monitoren van BCR ziekteprogressie. Om een completer beeld te krijgen van de identiteit van de lesies alsmede hun progressie is gebruik gemaakt van optische coherentie tomografie (OCT). Voor de evaluatie van ontstekingsactiviteit is fluoresceïne angiografie (FAG) en indocyanine groen angiografie (ICGA) geanalyseerd. Actieve netvliesontsteking gold wanneer de behandelaar een FAG als actief beoordeelde en besloot de behandeling te handhaven of intensiveren. Bij 9 van de 21 patiënten (43%) vonden wij ten minste één van de volgende lesies in de fotoreceptoren of RPE: circulaire chorioretinale lesies op FAF en OCT, verstoring van de ellipsoidale zone op OCT, en RPE-atrofie op FAF en

OCT. Van deze typen lesies was verstoring van de ellipsoidale zone het meest frequent (7 van de 21 patiënten, 33%). Vergelijkende beeldanalyse van FAF en OCT toonde een uitstekende overlap aan tussen gebieden van verhoogde FAF en verstoring van de ellipsoidale zone op OCT. Tevens werd een geheel of gedeeltelijk herstel van deze zone gevonden bij 4 van de 7 patiënten, gelijktijdig met een duidelijke afname in ontstekingsactiviteit in het netvlies na intensivering van behandeling. Dit onderzoek geeft de klinische presentatie van patiënten van BCR weer, specificeert het spectrum van lesies, en biedt inzicht in lesie progressie. Het monitoren van deze verstoringen kan helpen om anatomische verbetering na behandeling te bepalen, zelfs in geval van chronische ziekte.

Hoofdstuk 2.3 bouwt voort op Hoofdstuk 2.1 en presenteert een numerieke simulatie van oxidatieve stress in het RPE ten gevolge van blootstelling aan zonlicht of aan de excitatielaser van FAF. Deze stress werd vergeleken tussen gezonden en patiënten met STGD1, waardoor wij een indicatie kregen van de mate waarin opgestapeld lipofuscine in het RPE deze patiënten mogelijk gevoeliger maakt voor lichtblootstelling. De simulatie bestaat uit 3 hoofdfactoren die de hoeveelheid lichtabsorptie door lipofuscine bepalen, en uit een laatste factor die lichtabsorptie door lipofuscin aan zuurstofconsumptie relateert—deze zuurstofconsumptie is een indicator voor de productie van zuurstofradicalen en daarmee oxidatieve stress. Ten eerste werd de lichtintensiteit op het netvlies berekend: de jaargemiddelde stralingsintensiteit van diffuus zonlicht (λ = 380-700 nm) en de constante intensiteit van de FAF excitatielaser (λ = 488 nm) werden gecorrigeerd voor leeftijdsafhankelijke lichtattenuatie door de ooglens en oculaire media. Ten tweede werd lichtattenuatie door melanine in het eencellige pigmentepitheel gesimuleerd met een Monte-Carlo simulatie: deze bleek leeftijds- en golflengteafhankelijk te zijn, maar de totale attenuatie was gemiddeld genomen slechts 11%. Bij patiënten met STGD1 was attenuatie ongeveer 50% lager ten opzicht van gezonde leeftijdsgenoten. Ten derde werd lichtabsorptie door lipofuscine granulae in het RPE berekend aan de hand van de sterke correlatie tussen histologische metingen en gekalibreerde FAF-intensiteit. Vanuit het lineaire verband tussen deze factoren en extrapolatie berekenden wij respectievelijk een 3-voud en 2-voud hogere lichtabsorptie door lipofuscine bij patiënten met STGD1 versus 20- en 60- jarige gezonde personen. Interessant genoeg vonden wij bij gezonden geen leeftijdsgerelateerde toename in zuurstofconsumptie tijdens daglicht, maar wel tijdens FAF beeldvorming. Bij STGD1 was zuurstofconsumptie 3-voud hoger tijdens daglicht en FAF. Toekomstig onderzoek moet uitwijzen hoe goed deze simulatie de werkelijkheid benadert, alsmede de implicaties van deze toename bij STGD1. De 1.3-voud toename in oxidatieve stress tijdens FAF kan de anti-oxidatieve capaciteit kortstondig overschrijden, maar het is niet duidelijk of hierdoor schade aan het RPE of de fotoreceptoren kan ontstaan.

Hoofdstuk 3 beschrijft twee onderzoeken verricht met OCT. In **Hoofdstuk 3.1** hebben wij een theoretische en praktische analyse verricht aan bewegingsgerelateerde stoorfactoren, die een rol spelen bij metingen van fototransductie-geassocieerde intrinsic optical signals (IOS) met

OCT op basis van amplitude van reflecties. Tevens hebben wij literatuuronderzoek verricht naar de biofysische oorzaken van IOS. Op basis van gedeeltelijke inconsistenties tussen de signaalduur van IOS en een eerder voorgesteld causaal mechanisme—osmotische zwelling van de buitensegmenten van fotoreceptoren, en op basis van licht-verstrooiende elementen in deze buitensegmenten, stelden wij voor dat lokale fosfodiesterase (PDE) activiteit een oorzaak zou kunnen zijn voor het ontstaan van IOS. Beiden kunnen verandering in de optische weglengte tussen de binnen/buitensegment overgang van fotoreceptoren (IS/OS-junction) en de uiteinden van de buitensegmenten (OS tips) teweegbrengen. Om aan de hand van reflectie-amplitude veranderingen IOS te kunnen meten, moet met 4 factoren rekening worden gehouden. IOS van aanliggende fotoreceptoren kunnen tegenovergestelde polariteit hebben; om overspraak te voorkomen is cellulaire resolutie, hoge beeldacquisitiesnelheid, en beeldstabilisatie door beeldregistratie of active retinal tracking nodig. Om te voorkomen dat het optische Stiles-Crawford effect grote fluctuaties in de reflectieamplitude van kegel-fotoreceptoren veroorzaakt is het cruciaal om de optische as van het optische systeem op één lijn te brengen met de piek van de Stiles-Crawford functie, door pupil-gecentreerd te meten. Fluctuaties in signaalamplitude kunnen ook worden veroorzaakt door het sample van de OCT af te bewegen, veroorzaakt door een exponentiële afhankelijkheid van de gevoeligheid van OCT met deze afstand ('sensitivity fall-off'). Bij onze OCT verklaart deze factor 29% van de variatie in signaalamplitude tijdens IOS-metingen. Correctie is mogelijk na meting en Gaussian-fitting van dit effect. Tenslotte beschreven we een algoritme om zeer variabele belichtingsintensiteit bij M-B scans te reduceren tot een variatiecoëfficiënt van 6.9%. Recente ontwikkelingen door andere auteurs hebben geleid tot een specifieke OCT die in-vivo IOS-geassocieerde veranderingen in optische weglengtes in de buitensegmenten kan meten. Wij verwachten dat deze techniek spoedig klinisch bruikbaar kan zijn om functionele fotoreceptoren te detecteren, met name omdat deze fase-gebaseerde techniek relatief ongevoelig is voor de besproken stoorfactoren en omdat betere inzichten zijn verkregen over de biofysische oorzaak van dit signaal.

Hoofdstuk 3.2 presenteert een studie bij patiënten met chronische centraal sereuze chorioretinopathie (CSC) waarin kenmerken van abnormale bloedperfusie worden vergeleken tussen verschillende angiografische technieken, waaronder OCT angiografie (OCTA), FAG, en ICGA. Deze beelden werden op dezelfde dag verkregen voor een optimaal vergelijk van morfologische overeenkomst. Twee klinische onderzoekers tekenden in elk van deze beelden gebieden af waarin zij abnormaliteiten waarnamen. De overlap tussen geannoteerde gebieden werd gemeten met Jaccard indici (JIs). De meeste abnormaliteiten werden geannoteerd in lage-fase ICGA scans (>15 min na injectie van ICGA) en op OCTA van de choriocapillaris, met hoge (mediaan JI, 0.74) en gemiddelde (mediaan JI, 0.52) overeenstemming tussen de onderzoekers. De geannoteerde gebieden op OCTA van de choriocapillaris omvatten vaak focale afgenomen doorbloeding met omliggende verhoogde perfusiedichtheid. Lekpunten op ICGA lagen nabij punten van afgenomen doorbloeding op

OCTA van de choriocapillaris (gemiddelde afstand, 168 μm). Abnormale perfusiepatronen kwamen overeen met de locatie en omtrek van subretinaal vocht. Deze studie toonde frequente, doch relatief subtiele, abnormale perfusiepatronen bij CSC die bij andere studies niet nader gespecificeerd waren. De hyperdichte bloedperfusie rondom focale afnames in perfusie is te verklaren door reactieve – een suggestie die door bevindingen in een recente studie met vergelijkbare perfusiepatronen ondersteund wordt. Mogelijk ligt deze hyperperfusie ten grondslag aan lekkage, waardoor het RPE ischemische schade ondervindt en waardoor de barrièrefunctie van het RPE verstoord kan raken.

De studies in dit proefschrift laten zien hoe verschillende relatief subtiele imaging biomarkers correleren met de (patho-)fysiologie van het netvlies en choroidea, en met de ontwikkeling en progressie van netvliesaandoeningen. Hierdoor zijn nieuwe inzichten verkregen in het ziekteproces van STGD1, BCR, en chronische CSC. Aan de hand van deze biomarkers kunnen metingen worden verricht om de progressiesnelheid van belangrijke oogziekten te bepalen, zodat deze kunnen worden gecorreleerd aan genetica, omgevingsfactoren, en behandelingen.

Chapter 7

Dankwoord

Acknowledgements

De weg naar een academische promotie laat zich goed vergelijken met een ontdekkingsreis in de 16e eeuw met als doel het in kaart brengen van de *terra incognita*. Je navigeert vanuit bekend terrein en probeert je reis zodanig te plannen dat je nieuwe ontdekkingen kan anticiperen. Echter, anders dan de bekende ontdekkingsreizen uit het verleden kan je vaak niet vertrouwen op slechts één informatiebron (zoals ons gezichtsvermogen): je moet goed weten naar welke informatie je zoekt en welke bron daar het beste bij past. Een ander fundamenteel verschil is het feit dat je je verkenningstocht niet geïsoleerd van andere mensen hoeft te doen. Ik vond ontzettend veel steun en wijsheid bij mijn vrienden, familie en mijn collega's tijdens mijn reis, die was doorvlochten van blijschap en frustratie, gezelligheid en stress, schoonheid en chaos, hoop en twijfel.

Ik ben heel dankbaar dat ik de kans heb gekregen om te promoveren en wil graag mijn dank betuigen aan iedereen die op één of andere manier aan de totstandkoming van mijn proefschrift heeft bijgedragen. Hierbij wil ik een aantal van jullie in het bijzonder bedanken. Mocht ik iemand vergeten zijn: mijn excuses en alsnog hartelijk bedankt!

Prof. dr. C.B. Hoyng, beste Carel, door jou is mijn vermogen om sneller tot de essentie door te dringen sterk ontwikkeld. Je hebt me ook geïnspireerd om wat vaker buiten de grenzen van mijn eigen onderzoek te kijken naar belangrijke ontwikkelingen op mijn gebied. Bovenal heb je me doen inzien dat het belang van de patiënt altijd centraal staat. Bedankt voor je geduld, je laagdrempeligheid, je aanstekelijke en tomeloze enthousiasme over nieuwe technieken, en voor de mogelijkheden die je hebt weten te scheppen voor mijn onderzoek.

Dr. T. Theelen, beste Thomas, we hebben onze meningsverschillen gehad, soms heb ik een te detail-georiënteerde en perfectionistische inslag en neig soms naar het schrijven van te lange zinnen (zoals deze). Toch denk ik dat we een heel goede balans hebben weten te vinden met jouw ervaring, totaal-overzicht, pragmatisme en blik als clinicus. Ik denk dat we veel van elkaar hebben geleerd. Ik ervoer onze aangename gesprekken vaak als een steeds opgaande spiraal van wederzijds enthousiasme en nieuwe ideeën. Ook heb ik heel veel plezier beleefd aan onze trips naar o.a. Luxemburg, München en Oirschot en aan het proeven van je zelfgebrouwen (niet altijd lichte) bier. Ik ben je zeer dankbaar voor je vertrouwen, persoonlijke interesse en voor je voortdurende steun.

Prof. dr. B. J. Klevering, beste Jeroen, hoewel je me iets meer op afstand begeleidde tijdens mijn traject, is de toegevoegde waarde van jouw input zeer groot geweest. Je hielp mee het fundament van mijn projecten te leggen met verfrissende ideeën en pragmatische oplossingen. Bij de afronding (zoals het schrijven) wist je vaak constructieve kritiek te leveren en schroomde daarbij niet de methodiek en resultaten nog eens extra onder de loep te nemen. Zoals je weet heb ik hier altijd veel waardering voor gehad want: *"what doesn't kill us makes us stronger"*. Bedankt voor je rust, nuchtere blik en optimisme.

Dear colleagues of the Diagnostic Image Analysis Group, dear Clarisa, Mark, Bart and Freerk, I always looked forward to see you guys again and I really enjoyed our talks. I feel privileged that I got an inside-look into your innovative methods and to see how you tackle technical problems. Furthermore, I really appreciate all the help and the amount of time you invested in my various technical problems, in particular with functional OCT and quantitative AF. I hope that you found my input useful and if questions of any kind arise in the future, please feel free to contact me!

Drs. J.M. Groenewoud, beste Hans, bedankt voor je hulp bij het ontleden van de diverse problemen waar ik mee kwam en voor je nauwkeurige analyses. Dit wist je zodanig te doen dat ik eigenlijk altijd weer vertrok met meer inzicht in mijn probleem dan waar ik mee gekomen was.

Dr. E.K. de Jong, beste Eiko, ik wil je graag nog bedanken voor je persoonlijke interesse en je interesse in mijn projecten. Als je aanwezig was dan stond je deur eigenlijk altijd wel open, wat een heel prettig gevoel van deskundige ondersteuning gaf. Daarbij dank voor je input in de vorm van nieuwe en vaak zeer interessante mogelijkheden voor onderzoek.

Dr. B. Cense, beste Barry, ik heb een geweldige tijd in Utsunomiya gehad. Ik heb er enorm veel geleerd en met je collega's wisten we het ook altijd gezellig te maken. Ik denk nog graag terug aan het badmintonnen, *'No rice for you! You get wooden horse!'*, de zon-overgoten barbequeue, de Karaoke, het imposante vuurwerk tijdens het snikhete zomerfestifal en nog veel meer. Dank voor je optimisme (ook als ik weer eens beren op de weg zag liggen), je kennis en creative inbreng en je ruimhartige gastvrijheid. Ook wil ik graag Lim, Hans, Rolf, Fanny, David, Geliztle, Jackin, Din, ms. Hori en Jiyoung bedanken voor de vele gezellige momenten. Hopelijk zie ik jullie nog eens!

Francis, Berna, Laura, en ten tijde van mijn promotie Karlijn, Bart en Charlotte, jullie wisten me keer op keer uit de brand te helpen door een gaatje in de drukke agenda's van mijn begeleiders te vinden. Dank voor alle hulp, jullie interesse en flexibiliteit.

Jack, Hans, Asha, Angelique en Chantal, heel veel dank voor het mij aanleren van de diverse imaging technieken en voor onze vele aangename gesprekken. Dankzij jullie was het mogelijk om —tussen de reguliere patiënten door— op de Spectralis diverse dingen te checken of om te imagen, wat het zoveel makkelijker maakte om mijn onderzoek te doen.

Lieve dames van het trialscentrum, beste Anne en Maria, ik vond het altijd leuk om jullie weer te spreken over van alles en nog wat. Bedankt voor jullie interesse en jullie tijd voor mijn vragen en verzoeken.

Beste Bert, bedankt dat ik een tijd in de gradingroom mocht werken aan mijn qAF project. Ik vond het altijd leuk om even een praatje met je te maken over mijn onderzoek en alles daaromheen.

Beste Paulien, nogmaals van harte bedankt voor onze aangename gesprekken. Als ik weer iets nieuws bedacht had werd je vaak wel enthousiast over de nieuwe ontwikkelingen, en door jouw reactie werd ik dan ook weer enthousiast. Deze opwaartse spiraal en natuurlijk jouw kennis over birdshot hebben ongetwijfeld bijgedragen aan het mooie resultaat.

Beste Lieuwe, ik wil je graag nog hartelijk bedanken voor onze gesprekken over uveïtis en birdshot chorioretinopathie: ze waren voor mij echt een eye-opener.

Dr. de Mul, beste Frits, heel veel dank voor uw vele deskundige bijdragen en uw snelle reacties en MontCarl updates. Als medisch bioloog vind ik Monte-Carlo simulaties even zo fascinerend als complex. Echter, uw uitleg en adviezen en ons aangename gesprek bij u thuis gaven mij een stevig houvast bij dit onderwerp, wat in de toekomst ongetwijfeld van pas kan komen.

Dr. Rozanowska, dear Malgorzata, I feel honored that you collaborated with us on the fruitful lipofuscin phototoxicity project. Indeed, as you mentioned during our first Skype-meeting, the project proved to be a challenge. Undoubtedly many more challenges await in applying this method to study phototoxicity in the elderly and AMD – I would be delighted to explore this subject further and hopefully I get to enjoy your expertise herein as well.

Dear Prof. Dr. R. Theodore Smith, thank you so much for helping us make the study on the black contact lens for patients with STGD1 a success. Your groundbreaking AF-analysis software and the fantastic work of Michele D. Lee were indispensible, and I am greatly indepted to you both. I keep following your work with great interest, and I hope to get the opportunity to meet you in person at a congress in the future.

Mijn dank gaat ook uit naar mijn mede-promovendi met wie ik zin en onzin kon delen, wederkerig begrip en onbegrip heb gehad, bij wie ik mijn ei kwijt kon. Maar bovenal met wie ik het heel gezellig heb gehad. Ramon, bedankt voor je hulp bij mijn fOCT experimenten en bij al het andere waar ik vragen over had. John, bedankt dat je mijn vaste aanspreekpunt voor allerhande mannenzaken was (samen met Freekje). Yara, bedankt voor het organiseren van de Singstar avonden en voor je luisterend oor. Constantin, dank voor je hulp bij mijn imaging en voor onze vele aangename gesprekken. Myrte, ik ben je dankbaar voor het monnikenwerk dat je bij onze OCTA studie hebt gedaan en voor jouw kijk op de zaak: ik ben er zeker wijzer van geworden. Stanley, dank voor onze aangename samenwerking en je nuttige adviezen. Ook wil ik graag mijn dank betuigen aan alle andere promovendi voor de vele gezellige momenten: Nicole, Freekje, Laura, Nathalie, Roos, Maartje, Eveline, Dyon,

Vivian, Sanne, Dženita, Mahesh en Shazia. Laat maar weten als jullie willen dat ik nog eens Carel speel bij promotiefilmpjes!

Daarbij wil ik ook Bjorn en Frederieke bedanken voor jullie interesse en gezelligheid.

Ook wil ik graag alle niet-genoemde patiënten en proefpersonen hartelijk bedanken voor hun deelname aan ons onderzoek. Hun deelname is simpelweg onmisbaar voor het doen van medisch biologisch en geneeskundig onderzoek.

Mijn vrienden van 'de biobeuk', Arjan, Willemijn, Liene, Jeroen, Erik, Nathalie, Harriëtte, Jos, Bernard, Theo en Jacqueline wil ik bedanken voor het bieden van de broodnodige afleiding. Niets is zo fijn als 's avond na een lange dag werken op de bank te kunnen ploffen en met jullie al mijn gedachten en avonturen te kunnen delen. Dit, jullie kookkunst en natuurlijk de afwas (ja zoals bekend een echte hobby van mij…. Of toch niet? :P) hebben mij de energie gegeven om dit proefschrift bij elkaar te beuken! Bedankt voor de weekendjes weg (vol met inkiaanse avonturen), de gummiberen met wodka, de hilarische Sinterklaasavonden, de biologisch verantwoorde uitstapjes zoals de dierentuin en de Hortus Botanicus, het The-Big-Lebowski pakket inclusief bowlingbal, en jullie goede smaak qua muziek zoals the 90's/00's en een gezonde dosis metaal op zijn tijd.

Ik wil mijn paranimfen Jacqueline en Arjan graag nog apart bedanken dat jullie binnenkort aan mijn zijde willen staan. Sjek, je bent altijd bereid een begripvol en luisterend oor te bieden! Altijd leuk om weer 'ns een bakkie koffie met je te drinken en van je kookkunst te genieten. Ik ben heel blij dat wij vrienden zijn!
Arjan, wij zijn vrienden door dik en dun. In het begin in Vossenveld moest ik even een olifantenhuid ontwikkelen door al het (uiteraard goed bedoelde) op-de-kast gejaag en gestang met Bennie, maar hierdoor ben ik wel veel meer zelfverzekerd en relativerend geworden. Uiteindelijk moesten we er toch altijd weer flink om lachen (in het begin, moet ik toegeven, een beetje als een boer met kiespijn :P). Maar je kent me, soms ben ik 'een beetje' recalcitrant en ga mijn eigen weg, maar dat betekent niet dat ik je advies niet waardeer.

Ralf, al sinds ik je ken sinds de basisschool voelt het als vanzelfsprekend dat wij vrienden zijn. Niet omdat wij het altijd met elkaar eens zijn, maar juist omdat wij zo verschillend zijn. Bedankt voor je inspirerende verhalen die kunnen leiden tot soms briljante one-liners en gitaarspelen, het aanhoren van mijn oeverloze klets, onze discussies over films en series, je energie en humor.

Beste Gerrit-Jan en José, bedankt voor jullie interesse in mijn promotie. Nu kan ik eindelijk antwoorden op jullie veelgestelde vraag: het is nu eindelijk klaar! Fijn dat je mijn promotie bij wilt wonen.

Lieve oma, bedankt voor je eindeloze interesse in mij en mijn promotie. Na zo'n 5 jaar kan ik nu zeggen dat dit werk klaar is. Terugkijkend kan ik zeggen dat ik het erg leuk vond om te doen (is dat niet het belangrijkst?), dat ik het erg leerzaam vond en dat ik ook best wel trots ben op het resultaat. Nu op naar de volgende uitdaging!

De personen die het belangrijkst voor je zijn komen vaak als laatst aan bod bij het dankwoord en zo ook hier. Lieve Ronald en Kun, jullie hebben mijn werk op een afstandje gevolgd, maar altijd met veel interesse. Veel dank dankvoor. Jullie hebben nu in ieder geval een beter idee wat ik al die tijd heb uitgespookt in het ziekenhuis.

Lieve Guido en Els, lieve pap en mam, jullie staan altijd voor me klaar, in voor en tegenspoed. Jullie hebben me geadviseerd bij mijn belangrijkste beslissingen en doordat jullie me zo goed kennen heb ik jullie advies bijna altijd opgevolgd. Daar heb ik nog geen seconde spijt van gehad. Voor nu en voor altijd: bedankt.

List of publications

Publications related to this thesis

Teussink MM, Lambertus S, de Mul FF, Rozanowska MB, Hoyng CB, Klevering BJ, Theelen T. Lipofuscin-associated photo-oxidative stress during fundus autofluorescence imaging. *PLoS One.* 2017 Feb 24;12(2):e0172635.

Teussink MM, Huis in het Veld PI, de Vries LA, Hoyng CB, Klevering BJ, Theelen T. Multimodal imaging of the disease progression of birdshot chorioretinopathy. *Acta Ophthalmol.* 2016 Dec;94(8):815-823.

Teussink MM, Breukink MB, van Grinsven MJJP, Hoyng CB, Klevering BJ, Boon CJ, de Jong EK, Theelen T. OCT angiography compared to fluorescein and indocyanine green angiography in chronic central serous chorioretinopathy. *Invest Ophthalmol Vis Sci.* 2015 Aug;56(9):5229-5237.

Teussink MM, Lee MD, Smith RT, van Huet RAC, Klaver CCK, Klevering BJ, Theelen T, Hoyng CB. The effect of light deprivation in patients with Stargardt disease. *Am J Ophthalmol.* 2015 May;159(5):964-972.

Teussink MM, Cense B, van Grinsven MJJP, Klevering BJ, Hoyng CB, Theelen T. Impact of motion-associated noise on intrinsic optical signal imaging in humans with optical coherence tomography. *Biomed Opt Express.* 2015 Apr 9;6(5):1632-1647.

Other publications

Wolberink EA, van Erp PE, **Teussink MM**, van de Kerkhof PC, Gerritsen MJ. Cellular features of psoriatic skin: imaging and quantification using in vivo reflectance confocal microscopy. *Cytometry B Clin Cytom.* 2011 May;80(3):141-149.

Curriculum vitae

Michel Marco Teussink werd geboren op 21 november 1984 te Enschede. Na het behalen van zijn VWO diploma aan het Carmel College in Oldenzaal in 2003 begon hij aan de studie Biologie aan de Radboud Universiteit Nijmegen (destijds Katholieke Universiteit Nijmegen). Tijdens zijn studie liep hij gedurende 10 maanden zijn eerste stage onder leiding van Prof. Dr. Gert Flik op de afdeling Organismale Dierfysiologie aan het project 'The localization of Neuropeptide Y and α-Melanocyte Stimulating Hormone in the *Cyprinus carpio* hypothalamus'. Hij liep gedurende 6 maanden zijn tweede stage onder leiding van Dr. Piet van Erp, Dr. Rianne Gerritsen en Prof dr. Joost Schalkwijk op de afdeling Experimentele Dermatologie aan het project 'The correlation of reflectance confocal microscopy with histopathological features'.

De affiniteit die hij met beeldvorming ontwikkelde gedurende deze projecten vormde de basis voor zijn aanstelling als Operator confocal/advanced microscopy op het Microscopic Imaging Center –onderdeel van de afdeling Celbiologie– aan het Nijmegen Center for Molecular Life Sciences (tegenwoordig Radboud Institute for Molecular Life Sciences) onder leiding van Prof. dr. Peter Friedl en Dr. Jack Fransen. In deze periode, van februari tot september 2011, vergaarde hij kennis over de techniek en onderliggende optische principes van onder meer (spinning disk-) confocaal microscopie en multifoton microscopie.

Hij begon in december 2011 als onderzoeker in opleiding aan de ontwikkeling van een nieuwe *in vivo* beeldvormingstechniek aan de afdeling Oogheelkunde van het Universiteit Medisch Centrum St Radboud (tegenwoordig Radboudumc) te Nijmegen. Dit project had als doel functionele autofluorescentie en intrinsic optical signal-imaging gebaseerde functionele OCT te combineren en geschikt te maken voor klinische toepassingen in de oogheelkunde. Vanwege technische beperkingen die tijdens dit onderzoek aan het licht kwamen is de focus verlegd naar andere beeldvorming-gerelateerde aandachtsgebieden in de Oogheelkunde. De resultaten van dit promotieonderzoek staan beschreven in dit proefschrift.